ВІСНИК
КИЇВСЬКОГО НАЦІОНАЛЬНОГО УНІВЕРСИТЕТУ ІМЕНІ ТАРАСА ШЕВЧЕНКА

ISSN 1728-2306

РАДІОФІЗИКА ТА ЕЛЕКТРОНІКА

16/2011

Засновано 1999 року

Публікуються результати експериментальних та теоретичних досліджень у галузях фізичної електроніки, фізики плазми, фізики поверхні твердого тіла, емісійної електроніки, кріогенної та мікроелектроніки, нанофізики та наноелектроніки, високотемпературної надпровідності, квантової радіофізики, функціональної електроніки, твердотільної електроніки, мобільного зв'язку, медичної радіофізики, методів отримання діагностичної інформації та її комп'ютерної обробки.

Для науковців, викладачів вищої школи, студентів.

Experimental and theoretical contributions are published in the following fields: physical electronics, plasma physics, solid-state surface physics, emission electronics, cryogenic electronics, microelectronics, nanophysics and nanoelectronics, high-temperature supercondactive electronics, solid-state electronics, functional electronics, microwave electronics, quantum electronics, mobile communication, medical radio-physics, methods of receipt and computer processing of diagnosis information.

For researches, university teachers, students.

Адреса редколегії	03127, м. Київ-127, проспект акад. Глушкова, 2, корп. 5, радіофізичний факультет; ☎ (38044) 526 05 60;
Затверджено	Вченою радою радіофізичного факультету 08.11.10 (протокол № 4)
Атестовано	Вищою атестаційною комісією України. Постанова Президії ВАК України № 1-05/1 від 10.02.2010
Зареєстровано	Міністерством юстиції України. Свідоцтво про державну реєстрацію КВ № 15797-4269Р від 02.10.09
Засновник Та видавець	Київський національний університет імені Тараса Шевченка, Видавничо-поліграфічний центр "Київський університет" Свідоцтво внесено до Державного реєстру ДК № 1103 від 31.10.02
Адреса видавця	01601, Київ-601, б-р Т. Шевченка, 14, кімн. 43; ☎ (38044) 239 32 22; факс 239 31 28

CONTENTS

ЗМІСТ

UDC 621.385.833

T. Afanasieva, eng., O. Greenchuck, post grad. stud., I. Koval, Ph. D.,
M. Nakhodkin, Dr. Sci., Academician of NAS of Ukraine

DISSOCIATION OF O_2 MOLECULE ON PERFECT GE-GE ADDIMERS OF GE_XSI_{1-X}/SI(001) INTERFACE

Dissociation of chemisorbed O_2 molecule on perfect Ge-Ge addimers of Ge_xSi_{1-x}/Si(001) interface was investigated using ab initio calculations. Dissociation barrier of adsorbed O_2 on perfect Ge-Ge addimers of Ge_xSi_{1-x}/ Si(001) interface is 1,99 eV. O_2 dissociation is accompanied by spin conversions.

Key words: dissociation, interface, oxidation.

Використовуючи розрахунки з перших принципів ab initio досліджено дисоціацію хемаосорбовної молекули O_2 на чистих Ge-Ge аддимерах поверхні Ge_xSi_{1-x}/Si(001). Бар'єр для дисоціації становить 1.99 еВ. Дисоціація молекули O_2 супроводжується зміною спінового стану системи.

Ключові слова: дисоціація, інтерфейс, окислення.

Introduction. The oxidation of SiGe alloys has been investigated for both fundamental and theoretical reasons, as has Si oxidation. It has been expected as fabrication process for the gate oxide of SiGe channel metal-oxide field effect transistors (MOSFETs), which have higher carrier mobility than Si channel MOSFETs [11]. In recent years, it has also been employed in the fabrication of SiGe-on-insulator and Ge-on-insulator substrates [12,14]. These substrates have enabled high-speed MOSFETs with channel materials of strained Si, SiGe and Ge [10].

It was found that intermixing of Ge and Si atoms has a greater influence on oxygen uptake by Ge_xSi_{1-x}/Si(001) surface [5]. Such oxygen uptake was much less then in case of clean Si(001) surface [5]. Anyway, SiO_2 complex was found to appear faster on Ge_xSi_{1-x}/Si(001) than on Si(001) at the same conditions [9]. The reasons of such increasing in oxidation rate in case of Ge_xSi_{1-x}/Si(001) is unclear. Hence investigation of Ge_xSi_{1-x}/Si(001) interface oxidation is needed. Such investigation include: detailed study of clean Ge_xSi_{1-x}/Si(001) interface[1], stable O atoms adsorption configurations on Ge_xSi_{1-x}/Si(001) [2] and investigation of simple acts such as O_2 adsorption[4], dissociation, and diffusion of subsequent O atoms in to the bulk of Ge_xSi_{1-x}/Si(001)[3].

The aim of this work is investigation of chemisorbed O_2 dissociation process on perfect Ge-Ge addimers of Ge_xSi_{1-x}/ Si(001) interface. O_2 dissociation on perfect Si-Si and mixed Si-Ge addimers will be the aim of future research.

Methodology. Density functional theory calculations (DFT) with B3LYP [8] (Becke, three-parameter, Lee-Yang-Parr) pseudopotential were used to investigate O_2 dissociation on perfect Ge-Ge addimers of Ge_xSi_{1-x}/Si(001) interface. The basis set N21-3** was used for all atoms (Si, H, Ge, and O). Calculations were carried out with the aid of GAMESS package [13].

The Ge_xSi_{1-x}/Si(001) surface was simulated – analogously to what has been done in [3] – in the form of a $Si_{15}H_{14}Ge_2$ cluster (Fig. 1). The dangling bonds at the cluster boundaries were saturated with hydrogen atoms. In the initial approximation, the lengths of all Si–Si bonds were assumed to equal 2.35 Å (as they are in the bulk of crystalline silicon), and the lengths of Si–H bonds to equal 1.48 Å.

Positions of Ge addimer atoms and Si atoms of second subsurface layer were optimized (atoms in dashed box fig.1(a)). For simulating O_2 dissociation we use three reaction coordinate: h, $d_{o\text{-}o}$ and $d_{Ge\text{-}Ge}$ (fig1(b)). First we calculate the energy (E) of the system as a function of h and $d_{o\text{-}o}$ – $E(h, d_{o\text{-}o})$. It is well known, that surface reaction is often accompanied by spin conversion [4,7]. Hence, we plot singlet and triplet cases of $E(h, d_{o\text{-}o})$ dependence. At the spin conversion point we plot $E(h, d_{o\text{-}o})$ as a function of $d_{Ge\text{-}Ge.}$ – $E^{I}(d_{Ge\text{-}Ge.})$ in singlet and triplet system state. While doing this, we optimize position of second subsurface layer atoms (Si atoms in dashed box fig.1(a)). In such a way we find spin conversion point and corresponding energy value (E_{exect}). O_2 dissociation barrier (Δ) was found as $\Delta = E_{exact} - E_a$ (E_a-energy of $Si_{15}H_{14}Ge_2$ with adsorbed O_2).

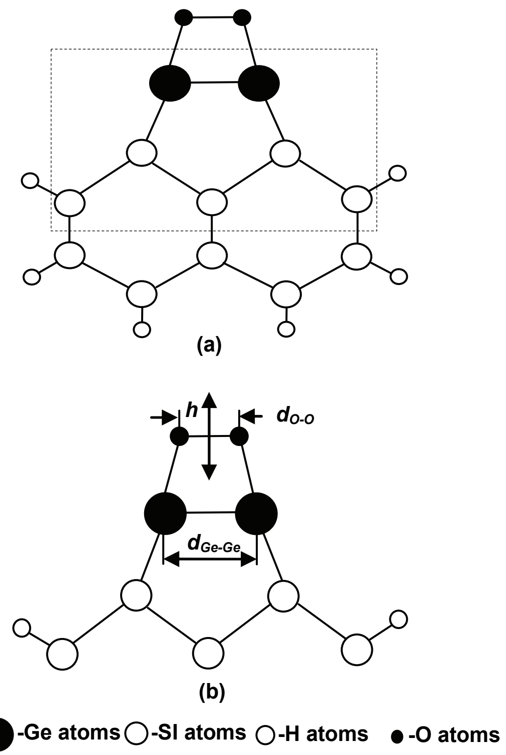

Fig.1 (a). Cluster $Si_{15}H_{14}Ge_2$ used to simulate Ge_xSi_{1-x}/Si(001) surface with chemisorbed O_2 molecule. Position of atoms in dashed box was optimized; (b)- coordinates used for simulating O_2 dissociation: *h*-height of O_2 under the addimer, $d_{o\text{-}o}$- distance between O atoms, $d_{Ge\text{-}Ge}$-distance between Ge atoms

Calculation of stable O_2 adsorption configurations and establishing of stable structure with two separate oxygen atoms was followed by hessian matrix [6] (second derivation of energy) calculation.

Calculation result. Before direct consideration of O_2 dissociation process, stable adsorption configuration of O_2 molecule and location of two separate O atoms after O_2 dissociation must be defined. Previously [4] we found that O_2 molecule is non dissociative chemisorbed on perfect Ge-Ge addimers of Ge_xSi_{1-x}/Si(001) interface. We consider such stable configuration of chemisorbed O_2 on perfect Ge-Ge addimers as a starting point of O_2 dissociation process (reactant) fig.2(a). The structure (c) (fig.2) was found as a final dissociation state of O_2 molecule (product). Fig. 2 also represents changing of Ge-Ge and O-O bond length upon O_2 dissociation process.

A Hessian matrix of the product and reactant structures doesn't contain any negative eigenvalues. It means that product and reactant (fig.2(a;c)) represent the true minimums of potential energy surface (PES). Electronic structure of such products will be discussed in next work.

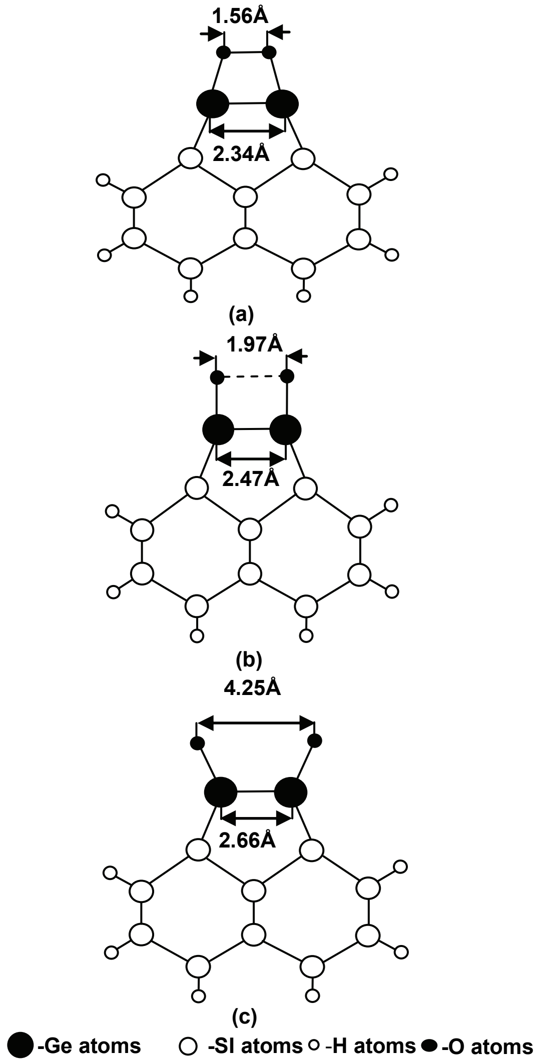

Fig. 2. Stationary structures and transition state structure of O_2 dissociation process on perfect Ge-Ge addimers of Ge_xSi_{1-x}/Si(001) interface. (a) – reactant, (b) – transition point, (c) – product

After finding product and reactant structure we plot $E(h, d_{o\text{-}o})$ dependence in singlet and triplet cases. While plotting $E(h, d_{o\text{-}o})$ we find that energy monotonically increase with h increasing at each $d_{o\text{-}o}$ value. Therefore, we conclude that reaction pass at almost constant h. Hence, we may analyze only $E(d_{o\text{-}o})$ dependence at constant h for singlet and triplet state – fig.3 (a). As we can see singlet and triplet $E(d_{o\text{-}o})$ cases have two intersection in (A) and (C) points. Hence, we can conclude that dissociation of chemisorbed O_2 on Ge-Ge addimer of Ge_xSi_{1-x}/Si(001) interface is accompanied by spin conversion.

First spin conversion during reaction pass happened at A point (fig.3(a)). Structure that is corresponding to A point in triplet and singlet state have different Ge-Ge bond length 2.56 and 2.34, respectively. To find the real spin conversion point we plot $E^{I}(d_{Ge\text{-}Ge.})$ dependence in singlet and triplet case – fig.3(b). In such a way we find a real spin conversion point – B. B point is corresponding to O-O bond breaking in chemisorbed O_2 on perfect Ge-Ge addimers of Ge_xSi_{1-x}/Si(001) interface. Structures that correspond to B point was found identical in singlet and triplet cases and are shown on fig.2(b) (transition state). Dissociation barrier was calculated as energy difference between reactant and transition state structure (fig. 2(a,b)). This difference is 1,99 eV. It is larger than in case of O_2 dissociation on clean Si(001) surface (0.69 eV [7]). The energy difference between reactant and product structure was less than 0,01 eV. This fact suggests a low probability of O_2 dissociation in contrast to Si(001) surface [7]. Therefore, oxidation rate of Ge_xSi_{1-x}/Si(001) have to be lower than in case of Si(001). For elucidating such disagreement with [9] investigation of O_2 dissociation on Si-Ge and Si-Si addimers of Ge_xSi_{1-x}/Si(001) interface is essential.

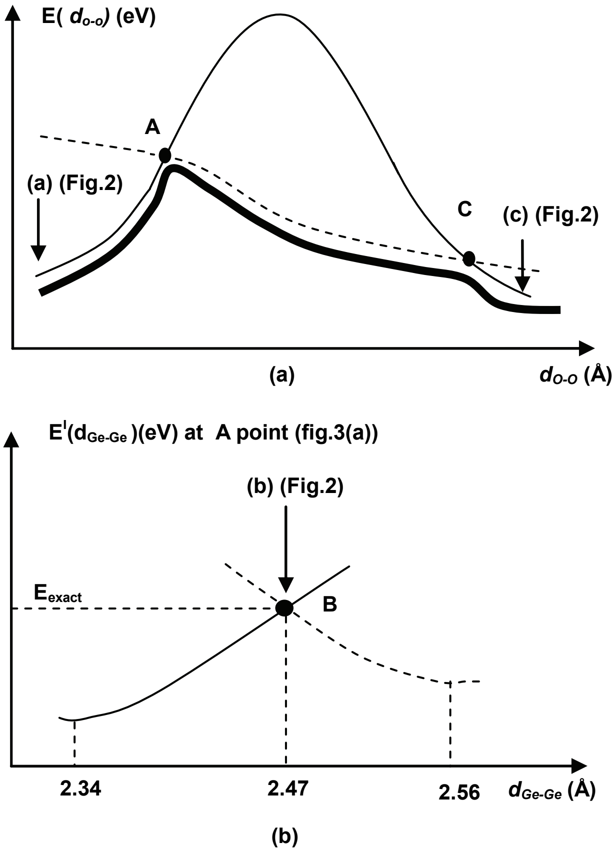

Fig.3. $E(d_{o\text{-}o})$ (a) and $E^{I}(d_{Ge\text{-}Ge.})$ (b) plot. ——— – singlet, – – – – – triplet

A few words have to be noted about charge exchange between surface and O_2 molecule. Such exchange is difficult for direct investigation [6]. Therefore we focused on O_2 and Ge-Ge bond length measurement. The bond length of chemisorbed O_2 on perfect Ge_xSi_{1-x}/Si(001) interface is 1.56 Å while simple O_2 bond length is 1.34 Å. Ge-Ge addimer bond length of Ge_xSi_{1-x}/Si(001) interface is 2.45 Å [1] after O_2 chemisorption, Ge-Ge addimer bond length decrease to 2.34 Å. Hence, we can assume that such changing of O-O and Ge-Ge bond length is accompanied by charge transfer from π^* Ge-Ge addimer antibonding orbital to π^* antibonding O_2 orbital. Hence we assume that π^* population of Ge-Ge addimer has a great influence on O_2 dissociation process.

As it was mentioned above O_2 dissociation was accompanied by double spin conversion (A and C points (fig.3(a)). First spin conversion is direct connected with O_2

dissociation barrier (A and B points fig.3) on perfect Ge-Ge addimers of Ge_xSi_{1-x}/Si(001) interface. Therefore we can assume that external magnetic field or photoexcitation can reduce dissociation barrier.

Conclusion. Dissociation of chemisorbed O_2 on perfect Ge-Ge addimers on Ge_xSi_{1-x}/Si(001) surface was investigated. The height of dissociation barrier was found to be equal to 1,99 eV. Also it was shown that this value can be reduced by photoexcitation or application of external magnetic field.

1. *Afanasieva T.V., Greenchuck A.A., Koval I.P., et. al.* Structure of Pure Si−Si, Ge−Ge, and Mixed Si−Ge Addimers on Si(001. Surface // Ukr. J. of Phys. – 2011. – № 3. – P. 240–247. 2. *Afanasieva T.V., Greenchuck A.A., Koval I.P., et. al.* Oxygen adsorption on the Ge/Si(001. surface // Visn. Kiev. Univ. Ser: Fiz.-Mat. – 2007. – № 2. – P. 207–210. 3. *Afanasieva T.V., Greenchuck A.A., Koval I.P., et. al.* Diffusion of Oxygen Atom Into Subsurface Layers of Ge_xSi_{1-x}/Si(001. Interface // Ukr. J. of Phys. – 2011. – № 4. – P. 352–358. 4. *Afanasieva T.V., Greenchuck A.A., Koval I.P., et. al.* Molecular oxygen adsorption on Ge_xSi_{1-x}/Si(001. surface // International Conference on the Physics and Technology of Thin Films and Nanosystems ICPTTFN-XIII2011, May, 16, 2011. 5. *Fukuda T., Ogino T.* Oxidation kinetics of epitaxial Ge-covered Si(100. surfaces // Surf. Sci. – 1997. – Vol. 380. – P. L469–L473. 6. *Jensen F.* Introduction to Computational Chemistry. – B., 1999. 7. *Kato K., Uda T.* Chemisorption of a single oxygen molecule on the Si(100. surface: Initial oxidation mechanisms // Phys. Rev. B. – 2000. – Vol. 62. – P. 15978. 8. *Kim K., Jordan K. D.,* Comparison of density functional and MP2 Calculation on the Water Monomer and Dimer // J. Phys. Chem. – 1994. – P. 10089–10094. 9. *Koval I. P., Len Y. A., Nakhodkin M. G.* Investigation of interaction of the oxygen with surface of alloy germanium-silicon by methods of electron spectroscopy // Visn. Kiev. Univ. Ser: Fiz.-Mat. – 2006. – № 1. – P. 275–273. 10. *Lee M. L., Fitzgerald E. A., Bulsara M. T. et. al.* Strained Si, SiGe, and Ge channels for high-mobility metal-oxide-semiconductor field-effect transistors // J. of Apll. Phys. – 2000. – Vol. 62. – P. 15978. 11. *LeGoues F. K., Rosenberg R., Nguyen T., et. al.* Oxidation studies of SiGe // J. of Apll. Phys. – 1989. – Vol. 65. – P. 1724. 12. *Nakaharai S., Tezuka T., Sugiyama N., et. al.* Characterization of 7-nm-thick strained Ge-on-insulator layer fabricated by Ge-condensation technique // Apll. Phys. Lett. – 2003. – Vol. 83. – P. 3516. 13. *Schmidt M.W., Baldridge K.K., Boatz J.A.,et.al* GAMESS, The General Atomic and Molecular Electronic Structure System // J.Comput. Chem. – 1993. – Vol. 14. – P. 1347. 14. *Tezuka T. Sigiyama N., Mizuno T., et.al.* A Novel Fabrication Technique of Ultrathin and Relaxed SiGe Buffer Layers with High Ge Fraction for Sub-100 nm Strained Silicon-on-Insulator MOSFETs // Jap. J. of Apll. Phys. – 2001.– Vol. 49. – P. 2866–2874.

Submited on 20.05.2011

UDC 681.3

I. Bilokon, stud., Y. Boyko, Ph. D., D. Gryaznov, assist., V. Melnik, stud.

FORMALIZING WORKFLOWS FOR AUTOMATION OF UNIVERSITY DOCUMENT MANAGEMENT SYSTEM DEVELOPMENT

A formalized workflow model was built. Mathematical graph theory was used. The common stages and tasks of incoming correspondence workflow were highlighted. The basic elements of workflow were allocated. The method of automation workflow development was proposed.

Key words: document docflow, workflow, theory of graphs, workflow model

Побудовано формалізовану модель документообігу. Використано математичний апарат теорії графів. Виділено основні етапи та задачі документообігу вхідної кореспонденції. Виділено базисні елементи документообігу вхідної кореспонденції. Запропоновано метод автоматизації розробки робочих процесів.

Ключові слова: документообіг, робочі процеси, теорія графів, модель робочих процесів

Introduction. An analysis of time spent of organizations, which work only with paper documents, shows that operations with documents (transportation, filling, processing, searching) take about 50-60% of time. These costs can be decreased by using document management system (DMS). Document management systems provide access, storage, processing, security and searching for any electronic information. Electronic one replaces paper document. Electronic document is document, information of which is fixed as electronic data, including required requisites [11]. Rationale for transition to such systems is shown in works [8], [4], and [5]. DMS accelerates workflows and enhances the quality of final product. It is explained by acceleration of information transition, improving working conditions for employees and labor discipline in organization. Introduction of DMS can help to decrease corruption ([3]) due to openness and transparency. Also introduction of such systems is one of the main tasks according to program "Electronic Ukraine" [7].

Modern DMS provides such facilities:

- Storing document attributes (document card).
- Integration with other program products.
- Converting paper documents to electronic ones using scanners and etc.
- Indexing.
- Document storage.
- Rights management.
- Collaboration over documents.
- Versioning.
- Workflow processing.

Electronic document management system requires formalizing and often reconstruction of internal processes [2]. This makes it impossible to develop all workflows at once. That's why it is appropriate to involve to system gradually each part of organization. Disadvantage of this method is permanent needing developers to extend and to create new workflows. This problem can be solved by giving to users tools for creating necessary workflows within organization. This approach will allow substitute traditional document processing gradually. This requires tools, which maximally simplifies workflow development and abstracts from their implementation. Usually this is achieved by using visual programming, which includes manipulating graphics instead writing code. In turn, graphics reflect certain stages of document processing and links between them determine the sequence of execution. The considered method of introducing workflows is relevant for organizations, which consist of many interacted departments and which require strict routing of documents, for example universities and regional administrations. The existing universal platforms for document management "EMC: DOCUMENTUM", "Microsoft: SharePoint 2010", "DocsVision", "IBM Lotus Notes") implement only the basic components of the DMS (including workflow management), but they are able to expand functionality.

Problem statement. In this work processes over incoming correspondence are selected as object of researching. The movement of each document is independent that allows analyzing workflow based only on the state of one document. He graphs are selected to create model of document management. The graphs are one of the most powerful tools to implement an intuitive presentation of applied problems. Application of graphs allows using established mathematical tools to represent data flows and change of the document states. The representation of production processes using graphs was carried out by V.M. Glushkov [2]. Description workflows as diagrams

BPD (Business Process Diagram), diagrams EPC (Event-driven process chain) or UML (Unified Modeling Language) diagrams is inappropriate in this work, because their models are complex for analyzing and selection specific processing stages of document management. Application of graphs allows using mathematical apparatus for obtaining similar kinds of movement stages. This enables to provide a simpler graphical notation for representing document management. The aim of this work is the analysis of workflow processes to allocate specific processing of documents, their mathematical representation and description of workflow construction using defined elements. This will allow developing visual components, which abstract developing of workflow from its implementation.

Document's movement in organization. Incoming documents can be received as packages, letters, and postcards or as faksograms, telegrams, e-mails, if transfer takes place by electronic communication lines. In the case of paper document, at first it is worked by secretary of record-keeping department and then is transformed to digital form. Such operations are performed over incoming documents ([10]): pre-processing, registration, overview by leadership and giving resolutions, review and execution of resolutions, statement to control, progress tracking, reporting to leadership. Each of these operations is workflow, in which document cab be transferred between subjects. A certain task is put to participant of the process. Then finish of execution is expected and process is continued depends on result. Following the established rules of document processing we can construct a model of document managing.

Introduction of model. Using work [6] we introduce three sets, which describe document managing: M – set of participants, A – set of actions, which can be executed over document, F – set of states (forms of document). Thus formal model of document managing is $DM = \{M, A, F\}$. The properties of these sets are below.

Set of participants

- Is a set of roles.
- Is complete, i.e. it should to include all roles that are included in document managing.
- Isn't degenerate – each participant has appropriate element of the set.
- Several participants can be related to one element of the set.

Set of states:

- Is completed and reflects adequately the states of documents.
- Each element of the set corresponds to a set of attribute values of the document.

Set of actions.

- Contains discrete actions, that are get after decomposition of process.
- Element of the set reflects the action that changes the document state definitely.
- Provides coherence of the set of states.

Relation that reflects interaction between objects of document management connects these three sets.

Because the movement of one document is being considered, the states of workflow are determined by its metadata – additional information about a document for easier management. So-called pair grammar is [6] used to determine an appropriate graph representation of introduced model. The pair grammar is composition of two grammars between rules and symbols of which an unambiguous mapping is established. We consider it as a translation system of one language to another. In our case, we need to match introduced notation (three sets $\{M, A, F\}$) and elements of graph – vertices and directed ribs. Elements of members set are associated with actions. It means that the member is determined who can change the state of document to another by executing the action over it. Following properties are inherent for the representation:

- one vertex corresponds to only one document state and vice versa;
- one rib corresponds to one action over a document and vice versa.

Rib connects one vertex with another only if corresponding to it action translates the document between states corresponding to connected vertices. The direction of rib is chosen so way that direction will indicate to a valid direction of workflow.

So workflow model is $G = \{E, V, I\}$, where E – the set of vertices, V – set of ribs of the graph, I – incidence relation. There are initial and final states in set of states. Initial states are states of document in which the document is on the beginning of workflow. Vertices with no incoming ribs correspond to initial states. Final states are states of document in which the document is on the completing of workflow. Vertices with no outgoing ribs correspond to them in the graph representation.

After representation of model of documentation using graph, we are able to apply the mathematical apparatus of graph theory to the workflow. Consider operations of union over document workflow, basing on graph theory (neglect other operations because they are not used in this work).

Operation of union is designated as

$$DM(V, E, I) = DM1(E1, V1, I1) \cup DM2(E2, V2, I2),$$

where DM – the resulting model, DM1 and DM2 – outgoing model of documentation. Rules of union:

- $V = V1 \cup V2$ – set of states (vertices) of the resulting documentation consists of the union of states of the initial workflows
- $E = E1 \cup E2$ – a set of actions (edges) of the resulting documentation consists of the union sets the initial action workflow
- $I = I1 \cup I2$ – incidence ratio of the resulting documentation consists of the sum of the initial workflow relationships.

Represent workflow as a set of task statements to participants, expectations of their performance and their execution. Basing on this, set of actions, states and members is specified.

Set of actions consists of:

- Subset of actions like "create task t for the participant y". Elements are denoted as c(t, y).
- Subset of actions such as "execution of task t by participant y". Elements are denoted as e(t,y).

Set of states consists of:

- subset of states such as "waiting execution of task t by participant y". Elements denoted as W(t,y).
- subset of connecting states – introduced to provide a connection subgraphs in appropriate manner. They reflect relations between different stages of workflow. Elements are denoted as C_i, where $i \in 1...N_c$ (N_c – number of connections).

Elements of the set of participants are denoted as y_i, where $i \in 1...N$ (N – number of roles). Their amount depends on the number of typical tasks in document workflow and their relations with participants.

Decomposition of model. After analysis of document processing stages and constructing their models according to the method in chapter 4. Typical tasks were established, which are set before the participants of document managing: document processing (t1), registration (t2), ratification (t3), execution (t4), verification (t5), overview (t6), publishing (t7), saving to archive (t8), choice one of the options (t9), transmission of personal letters (t10), reworking (t11), sending to other department (t12), reporting (t13), notification (t14),. The processes of document management were classified. There are types of processes, which were determined after analysis of models for each stage of document processing, in table 1.

Selected types can be represented as parameterized graphs, arguments of which are tasks and participants. In general choice type can have any number of options. For example formula of following workflow was written: "document is registered → reviewing by manager → depending on resolution document is published, or saved to archive or executed by participant and then document is published".

$$D = EP(y1,t2,C1,C2) \cup CP1(y2,y3,t14,t6,C2,C3) \cup VP(y2,t9,a1,a2,a3,C3,C4,C5,C6) \cup EP(y4,t7\,C4,C7) \cup EP(y4,t8\,C5,C8) \cup CP1(y5,y6,t4,t5,C6,C7)$$

This formula reflects graph of workflow with initial state C1 and final states C6, C7. Parameters a_1, a_2 and a_3 are responsible for decision to publish, to save to archive or to execute resolutions before publishing. States C1… C8 are passed in such way to provide appropriate sequence of workflow stages.

Table 1. **Process types**

Process type	**Incidence matrix**	**Graph represantation**
Cyclical process of 1 type CP1(y',y'',t',t'',C',C'')	$\begin{array}{l\|c\|c\|c\|c} & C' & W(t',y') & W(t',y'') & C'' \\ \hline c(t',y') & 1 & -1 & & \\ e(t',y') & & 1 & & -1 \\ c(t'',y'') & & 1 & -1 & \\ e(t'',y'є) & & -1 & 1 & \end{array}$	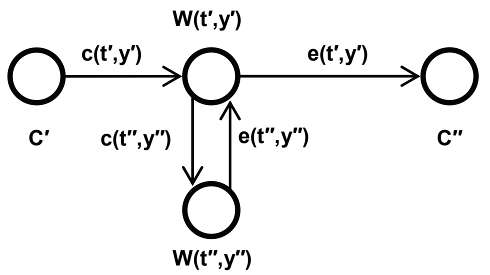
Cyclical process of 2 type CP2(y',y'',t',t'',C',C'')	$\begin{array}{l\|c\|c\|c\|c} & C' & W(t',y') & W(t'',y'') & C'' \\ \hline c(t',y') & 1 & -1 & & \\ c(t',y') & & 1 & -1 & \\ c(t'',y') & & 1 & -1 & \\ e(t'',y'') & & & 1 & -1 \end{array}$	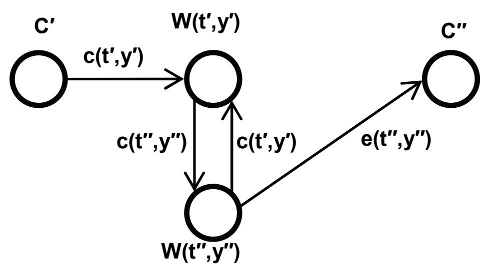
Choice process VP(y',t',a',a'',C',C'',C''	$\begin{array}{l\|c\|c\|c\|c} & C' & W(t',y') & C'' & C''' \\ \hline c(t',y') & 1 & -1 & & \\ e_1(t',y') & & 1 & -1 & \\ e_2(t',y') & & 1 & & -1 \end{array}$	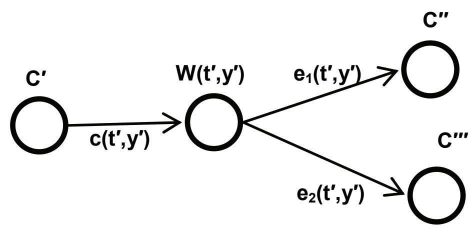
Execution process EP(y',t',C',C'')	$\begin{array}{l\|c\|c\|c} & C' & W(t',y') & C'' \\ \hline c(t',y') & 1 & -1 & \\ e(t',y') & & 1 & -1 \end{array}$	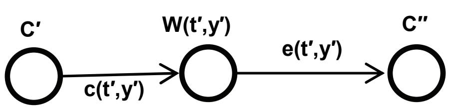

The sets of actions, states and participants were got according to rules of union from chapter 4. Incidence matrix of final graph is result of appending new columns and rows to initial one. In such way any workflow can be written as formula.

Earlier it was illustrated, that the workflow of incoming correspondence can be built by combining only formulated basic components. Thus the basic processes, which were determined, can be implemented as parameterized basic actions of a processes construction system.

Conclusions.

- According to document management rules common stages and problems of incoming correspondence workflow were established, that allowed to analyze and systematize them by kind of flowing.

- The formal model of document management was built, which allowed using mathematical analysis and algebraic operations of graph theory over workflows.
- The basic elements of document management were established, which allowed to build appropriate workflow by combining finite number of completely determined elements.
- The model built and the basic elements are ground for workflow visual programming system development.

1. *Березина Н.М., Воронцова Е.П., Лысенко Л.М.* Современное делопроизводство. – СПб.: Питер, 2004. 2 *Глушков В.М.* Введение в АСУ. – Киев: Техника, 1972. – 312 с. 3. *Дрожжинов В.И.* Электронный документооборот и управление записями на платформе EMC Documentum как инструмент для борьбы с коррупцией – 2008. 4. *Дубровин С.* Обычный и технический документооборот на промышленных предприятиях // Журнал Секретарское дело. – 2007. – № 3. 5. *Коляденко В.А.* Программа "Электронная Украина" – путь к информационному обществу // Информационное общество – 2004. – №. 2. – С. 15–16. 6. *Круковский М.Ю.* Графовая модель композитного документооборота // Математичні машини і системи. – 2005. – № 3. – С. 149–163. 7. *Круковский М.Ю.* Методология построения композитных систем документооборота // Математичні машини і системи. – 2004. – № 1. – С. 101–114. 8. *Малахов Е.В., Пелехов В.С.* Организация систем автоматизированого документооборота // Труды Одесского политехнического университета. – 2006. – № 1. 9. *Матвієнко О., Цивін М.* Основи організації електронного документообігу : Навчальний посібник. – К.: Центр учбової літератури, 2008. – 112 с. 10. *Охріменко Г.В.* Основні принципи та проблеми впровадження електронного документообігу в організації // Науковий блог НаУ "Острозька академія". – http://naub.org.ua/ 11. "Про електронні документи та електронний документообіг:". Закон України від 22 травня 2003 р. № 851-IV.

Submitted 20.05.2011

UDC 537.86/.87

D. Bozhko, stud., G. Melkov, Dr. Sci., V. Moiseienko, post. grad. stud.

BACKWARD VOLUME MAGNETOSTATIC WAVES SIGNALS SEPARATION BY ELECTROMAGNETIC PUMPING

In this paper theoretically and experimentally investigated separation of backward volume magnetostatic wave's signals by electromagnetic pumping. Basis of the method is phenomena of non-resonant wave front reversal in thin magnetic films, such as yttrium-iron garnet. Due to the fact that during wave front reversal maximum signals amplification occurs at half of the pumping frequency, and gain band depends on the power and duration of the pumping, changing the pumping frequency will lead to selective amplification of signals in the magnetic film, which can be interpreted as a separation. Thus, we studied the separation of pulse and monochrome signals of close frequencies, achieved separation of impulse signals with the difference in carrier frequencies above 20 MHz and for monochrome – 2 MHz. Developed spin – wave theory, which explains the physics of the addition of signal spectra, followed by amplification by pumping. Has been carried out a numerical simulation, which results are well consistent with experimental data.

Key words: Spin waves, signal separation, non-resonant wave front reversal, microwave filter.

В роботі теоретично та експериментально досліджено методику розділення сигналів зворотних об'ємних магнітостатичних хвиль за допомогою електромагнітної накачки. В основу методики покладено явище нерезонансного обернення хвильового фронту спінових хвиль в тонких магнітних плівках, таких як залізо-ітрієвий гранат. Через те, що при оберненні хвольового фронту максимальне підсилення сигналів відбувається на половині частоти накачки, а смуга підсилення залежить від потужності та тривалості накачки, зміна частоти накачки буде призводити до селективного підсиленню сигналів в магнітній плівці, що можна трактувати як розділення. Таким чином, було досліджено розділення імпульсних та монохроматичних сигналів близьких частот, вдалося виконати розділення імпульсних сигналів з різницею в несучій частоті більше 20 МГц і монохромних – 2 МГц. Розроблена спін – хвильова теорія, котра пояснює фізику додавання сигнальних спектрів з подальшим підсиленням їх накачкою. Було проведено числове моделювання, результати котрого добре узгоджуються з експериментальними даними.

Ключові слова: Спінові хвилі, розділення сигналів, нерезонансне обернення хвильового фронту, НВЧ фільтр.

Often a situation arises when the detector comes multiple signals and simple methods application to divide the resulting complex signal is not possible, especially in the case of equal carrier frequencies. For the case of signals of different frequencies can be used dispersive delay lines, as well as proposed earlier by non-resonant wave front reversal (WFR) of backward volume magnetostatic waves (BVMSW) in thin films of yttrium-iron garnet (YIG) [1].

WFR is widely used for information processing in all frequency bands – from optics to acoustics. Efficiency of WFR is maximal at resonance, when (in the case of three-wave parametric process) the carrier signal frequency ω_s is equal to half of the pump frequency: ω_p : $\omega_s = \omega_p / 2$. In this case we have amplification, controlled delay, time profile reversal, cloning of the signal, etc. [4, 5, 6, 9]. Because of the high frequency selectivity of WFR, there is the filtering process of input signals with high gain (several tens of decibels) and frequency band, which minimum width is determined by the relaxation frequency Γ_k of reversed waves. The center frequency of the WFR-filter for three-wave parametric process is equal to half of the pumping frequency and can be controlled by changing of this frequency. This makes it possible to implement with non-resonant WFR a series of operations of information processing, such as: narrow-band filtering, selection of input signals in frequency, followed by separating them in time, spectral analysis. This paper presents the results of a study of the non-resonant ($\omega_s \neq \omega_p / 2$) WFR with respect to the separation of the signals of two close frequencies simultaneously came to the receiver input.

Analysis of the non-resonant WFR of spin waves in YIG was carried out using the Landau – Lifshitz equation of the magnetization motion [3]. Considered the case of parallel pumping of spin-wave instability (frequency $\omega_p \cong 2\omega_s$) [6] taking into account the geometry BVMSWs, i.e. the case when the constant magnetic field H_0 is applied along the film and the direction of wave propagation [3].

Consider the case when the antenna input signal is single frequency. At the initial time $t = 0$ there are set of BVMSWs with all possible wave numbers k and amplitudes C_{k0} . These amplitudes are determined by the input signal $h_s(t) = h_{s0}(t)e^{i\omega_s t}$ and the efficiency of wave excitation F_k by antenna [2].

$$C_{k0} = I_k(h_s)F_k \exp\{i\omega_k t - \Gamma_k t\} \quad (1)$$

$$I_k = \frac{1}{t}\int_0^t h_{s0}(t)e^{i\omega_s t}e^{-i\omega_k t}dt \quad (2)$$

$$F_k = \exp\left(-\left(k/k_0\right)^4\right).$$

Here ω_k – intrinsic frequency of BVMSWs with wavenumber k, k_0 – maximum wavenumber, which can be excited by antenna.

Amplitude of reversed waves C_{-k}, which are result of the pumping switched on the time $t = T_p$ for time of τ_p, after switching off pumping ($t > T_p + \tau_p$) has the form [10]:

$$C_{-k}(t) = I_k F_k C^*_{-k}(t)\exp\left\{ i\omega_k(t - \tau_p - 2T_p)\right\}, \quad (3)$$

$$C^*_{-k}(t) = \exp\left\{ -\Gamma_k t + i\frac{\omega_p}{2}\tau_p + V_k h_p\tau_p - \frac{\Delta\omega_k^2}{2V_k h_p}\tau_p \right\};$$

$$\Delta\omega_k = \omega_k - \omega_p/2,$$

where h_p – pumping electromagnetic field amplitude, V_k – parametric coupling parameter between pumping and BVMSWs [3].

Power of output reversed signal P_r is calculated by summing the squares of modules of the wave amplitudes for all possible wave numbers at a time $t = 2T_p + \tau_p$, as in all other times phase is distributed randomly on the [0..2π] interval and the output signal is equal to zero [10].

$$P_r = \sum\left|C_{-k}\right|^2 \quad (4)$$

Relationship between the frequency of the wave ω_k and its wavenumber k was taken into account by the approximate dispersion relation for BVMSWs

$$\omega_k = \sqrt{\omega_H^2 + \omega_H\omega_M(1 - e^{-kd})/kd}, \quad (5)$$

Where $\omega_H = \gamma H_0$, $\omega_M = 4\pi\gamma M_0$, d - film thickness, H_0 – external static magnetic field, M_0 – saturation magnetization of the ferrite, γ – gyromagnetic ratio for electron's spin.

Analyzing the expression (3), can be concluded that for the duration of the pumping pulse implemented amplification of signal waves C_{k0} and the generation of reversed waves, whose amplitudes C_{-k} depends on their frequency ω_k. At high gains we get [7]:

$$C_{-k}^2 = C_{k0}^2 G_0 \exp\left[-\left(2\Delta\omega_k/\Omega\right)^2\right], \; \Omega = \sqrt{2V_k h_p/\tau_p}$$
$$G_0 = \exp\left[\left(V_k h_p - \Gamma_k\right)\tau_p\right]/2 \quad (6)$$

Substituting (6) (4), taking into account (1) and (2) we get that there is a resonant dependence of the reversed signal power P_r from the signal frequency ω_s with a maximum at $\omega_s = \omega_p/2$ and bandwidth $\sim\Omega$. Bandwidth Ω increases with the pumping amplitude h_p increases and with its duration τ_p decreases.

According to (3), provided $\Omega \to 0, C_{-k} \sim \delta(\omega_k - \omega_p/2)$ hence the reversed output power is:

$$P_r \sim \left[\int_0^t h_{s0}(t)e^{i\omega_s t}e^{-i\frac{\omega_p}{2}t}dt\right]^2 \quad (7)$$

It means that narrowband WFR-filter can be used for spectrum analysis of input signals, in particular for separation of BVMSW signals.

Now let us consider the case of m close by frequencies, signals, which are simultaneously excited input antenna. In this case equation (3) for amplitudes of waves after pumping action will become:

$$C_k(t) = C_{-k}(t) = I_k^\Sigma F_k \exp\left\{ i\omega_k(t - \tau_p - 2T_p)\right\}\times$$
$$\times\exp\left\{ -\Gamma_k t + i\frac{\omega_p}{2}\tau_p + V_k h_p\tau_p - \frac{\Delta\omega_k^2}{2V_k h_p}\tau_p \right\}, \quad (8)$$

where I_k^Σ – input signals spectrums. In case of rectangular impulses its spectrums will be:

$$I_k^\Sigma(\omega_k) = \sum_{i=1}^m 2\frac{\sin\left(\left(\omega_k - \omega_s^i\right)\frac{\tau_s}{2}\right)}{\left(\omega_k - \omega_s^i\right)}\exp(i\varphi_i) \quad (9)$$

Where m – maximum number of signals, simultaneously coming to the system.

For the case of monochromatic signals the total spectrum should have a Fourier expansion of only two components, but in reality there is always some broadening of the spectrum, which in our case can be written approximately as follows:

$$I_k^\Sigma(\omega_k) = \sum_{i=1}^m \exp\left[\frac{\left(\omega_k - \omega_s^i\right)^n}{\left(2\pi\Delta\omega\right)^n}\right]\exp(i\varphi_i) \quad (10)$$

Where n – integer number, which varies depending on the desired shape of the spectrum from 1 to 100, in the theoretical calculations we used $n = 1$. In this expressions also has been taken into account that these signals may be, in general case, phase shifted by random angles φ_i.

Measurements were carried out on an experimental section considered in [1]. It consists of a YIG film mounted in an open dielectric resonator (ODR) and placed on two, photolithographic method formed, input and output microstrip antennas, a width of 25 μm with lead lines. The distance between the antennas was 6 mm. The test sample of the ferromagnetic film width of 1.5 mm was cut from a single-crystal YIG film thickness of 5.1 μm with low magnetic losses ($\Delta H = 0.3\,Oe$). The film was grown on a substrate of gallium-gadolinium garnet by liquid phase epitaxy. Saturation magnetization of the film is 1750 gauss. The film was magnetized to saturation by a bias magnetic field $H_0 = 969\,Oe$, which was set on to the plane in the direction of wave propagation. Measuring section is located at the outlet flange of 3cm waveguide of pumping channel by which the pumping signal was brought into the system. As the pumping source was used pulsed magnetron M857. Maximum impulse power of the pumping signal at the output flange of the pumping channel was 7 watts.

In an experiment were used signals from two microwave generators, which are regulated by attenuation precision attenuators, and then they are fed to the adder, the output of which was loaded onto the input antenna of the measuring section. Input antenna excited in the YIG film complex signal BVMSWs consisting of a set of frequencies of two signals with carrier frequencies ω_{s1} and ω_{s2} and duration τ_{s1} and τ_{s2}. At the time of passage of the wave packet through the film, on the ODR applied pumping pulse with duration τ_p, resulting in the input and output antenna appears WFR and amplified signal, respectively. After two stages of amplification, these signals are fed to the semiconductor detector, where their envelope was registered with an oscilloscope Tektronix TDS 3032B. WFR signal and the amplified signal are suitable for research, but because it is more convenient to use only one input antenna, all subsequent measurements we performed for the WFR signal.

Fig. 1 shows the experimentally obtained dependence of the signal WFR on half of the pumping frequency. Frequency of the first incoming signal was 4715 MHz, the difference between the carrier frequencies of first and second signals 10 and 40 MHz respectively. Power of input signals was $P_{s1} = P_{s2} = -75$ dBm, pumping $P_p = -7.6$ dBm. The duration of the incoming signals was $\tau_p =$ 50 ns, duration of the pumping $\tau_p =$ 50 ns. By scanning the entire frequency range of signals by pumping frequency, were measured frequency responses of the total input signal.

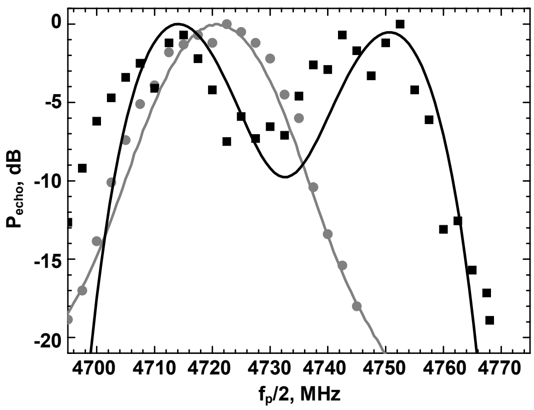

Fig. 1. Frequency response of the two incoming signals $\Delta f_s =$ 10 MHz (●) and 40 MHz (■). The theoretical curves (solid lines) calculated at $V_p =$ 0.95 MHz. The carrier frequency of the first input signal was 4715 MHz

As a result of parametric amplification the frequency components of a complex input signal by pumping, there are resonances at the pumping frequency f_p equal to twice the carrier frequencies of each of the components of the incoming signal $2f_{s1}$ and $2f_{s2}$. The optimal choice of power and duration of pumping is important, because it affects the bandwidth of the gain Ω (6). So you can see that with the difference between frequencies 10 MHz achievement good separation of the spectra is not possible. A completely different situation is for the difference in carrier frequencies of 40 MHz, one can see here is a good division. It is important to note that the AFC of output signal frequency can be seen a small frequency cut. This is due to overlapping sidelobe components of the signals, and at a frequency where the same central and lateral lobe of the spectrum of the rectangular signal they summed up, resulting in a response received such a complicated form. Separation is considered effective if there is no overlap of spectral components at -3 dB. The theoretical results obtained by numerical simulations shared the above formulas and assumptions of the mathematical model.

In the case of monochromatic signals ($\tau_s = \infty$), the dependence of the WFR signal power on half of the pumping frequency $f_p/2$ is given in Fig. 2. In this case, all processes are in principle similar with separation of signals of rectangular envelope. The difference is that the calculations used an approximation of the spectrum monochromatic signal, due to the fact that monochromatic signals does not exist, there is always a certain width of the spectrum and it was suggested to use as a spectrum of incoming signals (10) Gaussian spectral line with variance of 1 MHz. Power of input signals was $P_{s1} = P_{s2} = 6$ dBm, pumping $P_p = -78$ dBm, and the duration of the pumping pulse $\tau_p =$ 2.5 μs. By scanning the entire frequency range of signals by pumping frequency f_p, the overall AFC of input signals were measured. As can be seen from the already mentioned above on Fig. 2, for monochrome signals can be achieved a sufficiently effective separation of signals with a difference of carrier frequencies of 2 MHz and 5 MHz at -3 dB. The theoretical limit on the separation is – 1 MHz.

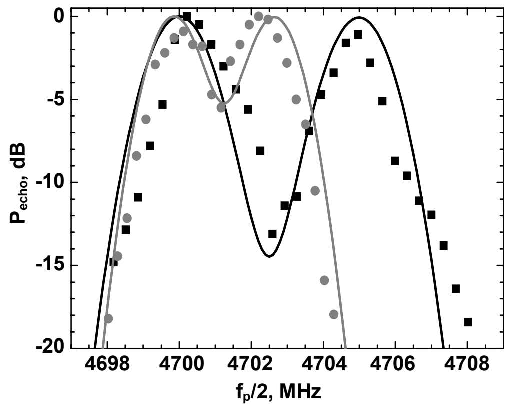

Fig. 2. Frequency response of the two incoming signals with $\Delta f_s =$ 2 MHz (●) and 5 MHz (■). The theoretical curves (solid lines) calculated at $V_p =$ 22 MHz. The carrier frequency of the first input signal is $f_s = 4700$ MHz

As a result of this work was implemented the possibility of using non-resonant WFR for microwave filtering and signal amplification, as was predicted in [1]. The method of backward volume magnetostatic waves signal separation in YIG thin films by using an electromagnetic pumping was investigated theoretically and experimentally. It was confirmed that the wave front reversal maximum amplification of signals occurs at half of the pumping frequency, and gain band depends on the power and duration of pumping. It was managed to obtain the separation of pulsed and monochromatic signals of close frequencies with a difference of carrier frequency greater than 20 MHz and for monochromatic signals – 2 MHz. Spin – wave theory, which explains the physics of the addition of signal spectra, followed by amplification by the pumping was developed. On the basis of it was written software to calculate the spectra of the signal at the output of device. The theoretical results are well consistent with experimental data.

1. *Vasyuchka V. I., Melkov G. A., Slavin A. N., Chumak A. V., Moiseienko V. A., Hillebrands B.* Non-resonant wave front reversal of spin waves used for microwave signal processing // J. Phys. D: Appl. Phys. – 2010. – Vol. 43 – P. 325001 (4pp). 2. *Васючка В. І., Лазовський В. В., Мойсеєнко В. А,* *Чумак А. В.* Вплив ефективних параметрів плівок залізо-ітрієвого гранату на характеристики пасивної лінії затримки // Вісн. Київ. нац. ун-ту ім. Т. Шевченка. Серія: радіофізика та електроніка. – 2006. – Вип. 9. – С. 15–18. 3. *Gurevich A. G., Melkov G. A.* Magnetization Oscillations and Waves. – N.Y.: CRC Press, 1996. 4. *Zel'dovich B. Ya., Pilipetckii R. F., Shkunov V. V.* Principles of Phase Conjugation. – Berlin: Springer, 1985. 5. *Luukkala M., Surakka J.* // J. Appl. Phys. – 1972. – Vol. 43. – № 6. – P. 2510. 6. *Melkov G.A. et al.* // Sov. Phys. JETP. – 1999. – Vol. 89. – P. 1189. 7. *Melkov G.A., Kobljanskyj Yu.V., Serga A.A., Tiberkevich V.S., Slavin A.N.* // Phys. Rev. Lett. – 2001. – Vol. 86. – № 21. – P. 4918. 8. *Melkov G.A., Vasyuchka V.I., Chumak A.V., Tiberkevich V.S., Slavin A.N.* // J. Appl. Phys. – 2006. – Vol. 99. – P. 08P513. 9. *Smith Kevin R., Vasyuchka Vitaliy I., Wu Mingzhong, Melkov Gennadiy A., Patton Carl E.* The Cloning and Trapping of Magnetostatic Spin Wave Pulses by Parametric Pumping // Phys. Rev. B. – 2007. – Vol. 76. – P. 054412 (6 pp.). 10. *Чумак А. В., Коблянський Ю.В., Васючка В. І.* Дослідження профілів вихідних імпульсів пасивної і активної ліній затримки сигналів на зворотніх об'ємних магнітостатичних хвилях // Вісн. Київ. нац. ун-ту ім. Т. Шевченка. Серія: фізико-математичні науки – 2004. – Вип. 1. – С. 353–360.

Submitted on 15.05.2011

UDC 004.7

Yu. Boyko, Assoc. Prof., O. Podolskyi, stud., R. Synyuk, assist.

IMPLEMENTATION OF REDUNDANCY AND LOAD BALANCING SERVERS ACCESS IN METRO ETHERNET NETWORKS

This article was reviewed existing protocols provide access to the Internet, discussed advantages and disadvantages of each of them. Was done the analysis of existing methods of Redundancy and the balancing of access servers. Based on existing methods it was proposed and implemented its own Redundancy and system and balancing.

Keywords: redundancy, load balancing, protocols, Virtual Local Area Network, customer, router.

В даній статті було розглянуто існуючі протоколи надання доступу до глобальної мережі Інтернет, перераховано їх недоліки та переваги. Проведено аналіз існуючих методів резервування та балансування серверів доступу. На основі існуючих методів було запропоновано та реалізовано власну систему резервування та балансування.

Ключові слова: резервування, балансування навантаження, протокол, віртуальна локальна мережа, користувач, маршрутизатор.

Introduction. Every year the number of services and amount of information available to users of Internet tremendously increase. As a result, network technologies occupy more space in everyday life. All this was made available thanks to modern broadband networks. At the same time Internet Service Providers (ISP) have some problems associated with termination of large number of users and network security.

Nowadays such methods are actively used for providing Internet access: Tunneling Protocols [1], Point-to-point protocol over Ethernet (PPPoE) [2] and Internet Protocol [3] (IP) over Ethernet (IPoE).Consider in more detail each of them.

Tunneling Protocols.

These include Point-to-Point Tunneling Protocol (PPTP) and Layer Two Tunneling Protocol (L2TP).

The PPTP is a network protocol that allows the computer to establish connection to the server through a special tunnel in the conventional network. PPTP encapsulates Point-to-Point Protocol (PPP) frames in IP-packets for transmission over a global IP-network.

Protocol L2TP is a tunneling protocol that provides encapsulation and forwarding the PPP frames. L2TP protocol encrypts IP traffic and forwards through an environment that supports the delivery of point-to-point datagrams. Implementation of Microsoft L2TP protocol uses IP Security (IPSec) encryption to protect data flow all the way from VPN client to VPN server.

The PPPoE is a network protocol of transporting PPP frames over Ethernet. PPPoE encapsulates PPP frames into Ethernet frames. In such type of communication the virtual channel establishes between the server and the client at first, then the PPP connection establishes in this channel, and finally PPP packets are packed in IP-traffic.

IPoE fundamentally differs from PPTP and PPPoE. In general, this technology does not exist, no RFC and no standards. But by itself it is united Internet Protocol and Ethernet, what should its name from the IP over Ethernet. Such architecture is a standard local area network (LAN). Users are given statically or dynamically public IP addresses or private in combination with Network Address Translation [8].

Nowadays the network architecture that consists of IPoE combined with VLAN-Per-Customer technology (Virtual Local Area Network – VLAN [4]) intensively develops and IP unnumbered is used, for the rational use of address space, if public addresses are assigned to users. Architecture VLAN-Per-Customer involves the allocation to each user their own VLAN. As a result, each client is located in a separate broadcast segment.

Table 1. **The comparative analysis of existing methods**

	PPTP	L2TP	PPPoE	IPoE	IPoe + vlan-per-customer
Redundancy	+ (DNS)	+ (DNS)	++ (automatically)	+ (HSRP, VRRP)	–
Load Balancing	+ (DNS)	+ (DNS)	++ (automatically)	+ (HSRP, VRRP)	–
Productivity	– *	– (creating tunnel)	– *	+	+
Address allocation	+ (centralized pool)	+ (centralized pool)	+ (centralized pool)	– (uses subnets)	+ (mask /32 of the user)
Resistance to attacks	– (IP, MAC, ARP attacks)	– (IP, MAC, ARP attacks)	± (MAC)	– (IP, MAC, ARP attacks)	++ (complete isolation)
Additional options	– (username, password and IP)**	– (username, password and IP)**	± (username and password)	+ (No)	+ (No)

* Productivity falls, because that in these protocols there is a conversion of 8 bits in 7 bits.

**It is required additional options of the software for the party of the client. Each client should have Username & password.

For today, in providing access to the global network Internet, an important role plays maintenance of trouble-free access and the maximum safety in a network. Based on consideration of Table 1, the maximum protection is provided in the implementation architecture IPoE + VLAN-Per-customer. This is achieved due to complete isolation of all the customers at the second level of OSI model. As a result, the possibility of network attacks (IP or MAC-addresses substitution, the installation of unauthorized Dynamic Host Configuration Protocol (DHCP)-server, ARP Spoofing) decreases. The number of broadcast traffic also decreases, which reduces network load, and less impact on network bandwidth. If necessary, access between customers can be implemented using Proxy ARP. But there is an important issue to provide load balancing and backup of connections. It is possible to apply the protocols used in IPoE.

- HSRP[5]
- VRRP[6]
- GLBP[5]

The principle of these protocols is similar. These protocols allow multiple routers to be grouped and act as a virtual router with a virtual IP. One group member is elected as the Active router, while others remain inactive, as long as there will be no failure of the active router. The members of the group send Hello messages each other, after the determined period of time for maintaining relationship.

The disadvantage of these protocols when applied them to architecture IPoe + VLAN-Per-customer is that they work on interface basis and the settings should be performed for each network interface card. As the large number of VLAN is used in architecture VLAN-Per-customer, large number VLAN Interfaces should be configured. As result, the large number of processes and a large flow of traffic between servers will be created while significantly reducing system performance.

It was decided to create its own redundancy system and balancing that works with a group of VLAN interfaces operating in mode trunk [4], not with individual interfaces.

Implementation. To implement and test the system, a test model was assembled. Its consists of two Network Access Server (NAS), Switch (Cisco catalyst 2950) and two client stations, Access Server PC OS UNIX (FreeBSD) as a platform.

As the server to access to a network, it is possible to use specialised NAS and alternative, constructed on the basis of PC under control of OS Linux or FreeBSD. NAS on the basis of PC OS FreeBSD, with use of modern powerful processors, for example, the Intel Xeon, capable to process (without loss) one million packages a second and to work in a normal mode at speeds 1 – 2 gigabit per second (Gb / s). This is enough for the networks of the middle class. The use of such Network Access Server requires less capital than by using specialized NAS. But they need a more complex configuration for proper operation.

To work with a large number of VLANs and its easy configuration, our own DHCP server was created. At startup it loads configuration from a local database, which contains all the information on users, and given Active (pri_terminator_id) and Reserve (sec_terminator_id) gateway for each user. As gateway the virtual IP dynamically assigned to users by default. Load balancing is realized in such way that some users are connected to one server and some to another. When one of the servers receives Address Resolution Protocol (ARP) [7] request from the user before sending him ARP reply is checking whether this server is Active (pri_terminator_id) to the user from which came the query. If not, request ignored, if so, the server responds with the virtual Media Access Control (MAC)-address that is same for both servers. This process is shown in fig. 1.

So one server acts as an active gateway for one half of the users, but the backup for the other half whereas another server acts vice-versa. As a result, some network traffic is forwarded through a one server, and another part through another. That is a load balancing process, this process shown in fig. 2.

In case of failure of Active server, its users are automatically switched to Reserve. In the test version switching is occurred in such way: the command, which terminate to serve users is entered on active server, at the same time the command is sent to the command channel of backup server, so backup server starts to send ARP replies to all VLAN interfaces for which he was a backup. As the source MAC address the virtual MAC addresses common for Active and Reserve servers is specified. Then backup server starts to serve all users. The process of switching is shown on fig. 3.

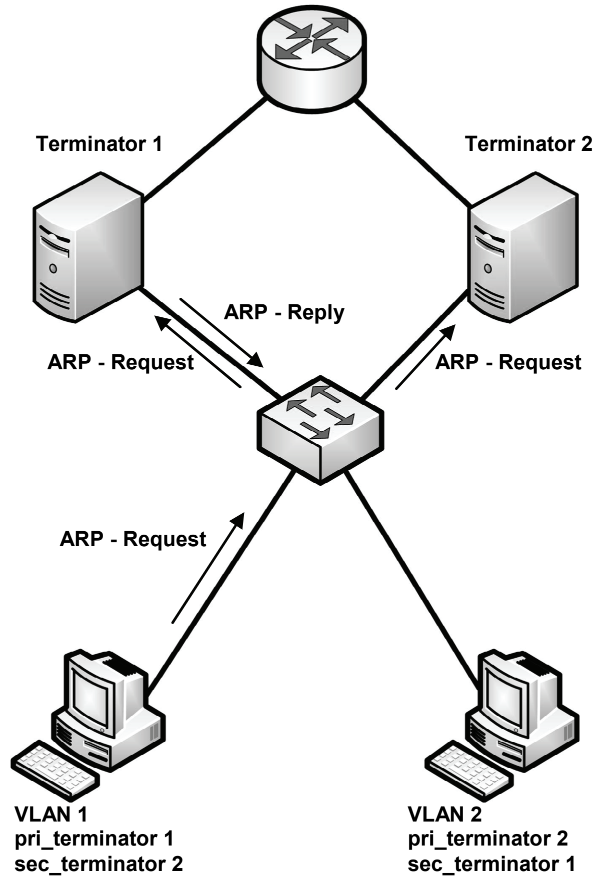

Fig. 1. Send ARP – request

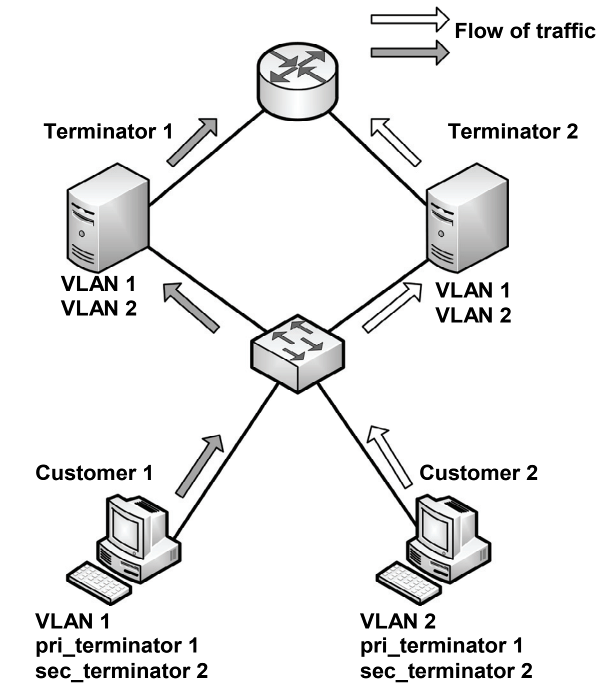

Fig. 2. Load balance process

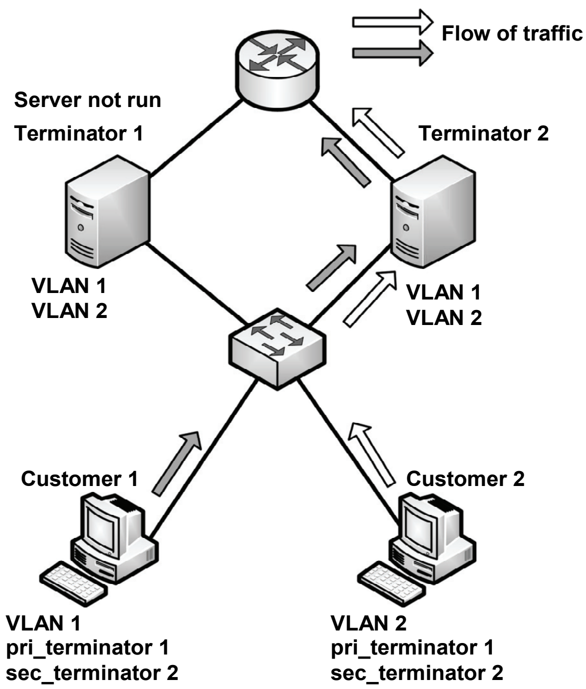

Fig. 3. Switch users

With the implementing of this architecture the problem of choosing the scheme that would be better to realize appeared: the virtual IP and real MAC, or virtual MAC and virtual IP. A preferred scheme would be to use both real and virtual MAC addresses on the interface, but to attach two MAC addresses to one network adapter is impossible. So we had to use a virtual MAC and virtual IP. Then there was another problem. As it turned by default network card does not transmit network frames in which the destination MAC address differs from its MAC address. So an Promiscuous mode, which ignored this rule, had to be enabled on adapter.

Conclusions. The described system was implemented and tested in the laboratory. The obtained results allow to implement it in real network. There is the possibility of its further improvement, such as automated mutual server monitoring and close cooperation with UP-Link.

Therefore, network architecture IPoE VLAN-Per-Customer in conjunction with DHCP and created load balancing system meets most requirements that exist currently in the construction of networks, such as to ensure a high level of protection and to provide of reliable Internet access.

1. Відкрита багатомовна енциклопедія. – Доступ до сайту: http://en.wikipedia.org/wiki/Virtual_private_network. 2. RFC 2516 – A Method for Transmitting PPP Over Ethernet. 3. RFC 791 – INTERNET PROTOCOL. 4. IEEE 802.1Q. 5. Технічна документація компанії cisco. – Доступ до сайту: http://www.cisco.com/en/US/docs. 6. RFC 3768 – Virtual Router Redundancy Protocol. 7. RFC 826 – Ethernet Address Resolution Protocol. 8. RFC 1631 – The IP Network Address Translator.

Submitted on 26.05.2011

UDC 577.3

V. Vysotskii, Dr. Sci., A. Vasylenko, post grad. stud.

3-D BLOW-UP REGIME OF A QUASILINEAR PARABOLIC HEAT TRANSFER EQUATION APPLYING TO A LOCAL HYPERTHERMIA

This article studies 3-D quasilinear heat transfer equation in a case of spherical symetries. The possibility of blow-up solutions for this equation was regarded. Also functional dependence of material parameters of radial component and temperature that makes possible blow-up solutions was found.

Keywords: local hyperthermia, blow-up regime, 3-D qusilenear heat transfer equation, patological tissue.

У роботі розглянуто тривимірне рівняння теплопровідності для випадку сферичної симетрії та досліджено можливість реалізації режиму з загостренням. Знайдено функціональну залежність матеріальних параметрів від радіальної змінної та температури, що дозволяють реалізувати цей режим. Також вказано на можливі шляхи модифікації матеріальних параметрів у випадку біологічних тканин.

Ключові слова: локальна гіпертермія, режим з загостренням, 3-D квазілінійне рівняння теплопровідності, патологія тканин.

Introduction. The human body naturally uses heat to fight disease. This fact was used to develop methods of treatment that are based are on artificially increased temperatures. Temperature may be increased locally then treatment is called local hyperthermia. In the other case it is called whole body hyperthermia if a temperature of a whole body was increased. Most common use of hyperthermia is cancer treatment. It is obviously that in most cases heating of a whole body is unnecessary and unwanted because of possibility to make damage to normal tissue while pathological tissue is localized in a small region. Hyperthermia is often used as an adjunct therapy to radio- therapy and/or chemotherapy to increase their effectiveness, but hyperthermia alone exhibits both antineoplastic and immunological effects. Nevertheless there are still a lot of problems that should be solved to permit hyperthermia become more than unfulfilled promise. One of them connected with a focusing of high percentage of temperature field energy in tumor tissue and preventing damage of normal tissue [1, 2]. In this paper blow-up regimes of a quasilinear parabolic heat transfer equation are proposed as a method to control heating during local hyperthermia and conditions for it realization in 3-D case are formulated.

1-D blow-up regimes. Blow-up regimes were well studied analytically and numerically for a one dimensional case [5]. While for a three dimensional case it was shown that for a wide range of heat conductivity coefficient functional dependences of temperature blow-up regime is prevented [4].

General form of heat transfer equation is as follows:

$$\rho c \frac{\partial T}{\partial t} = \nabla \cdot \left(\lambda \nabla T \right) + S , \qquad (1)$$

where ρ is density, c is heat capacity and λ is heat conductivity. Usually for a one dimensional case blow-up solutions are studied on equations of the next shape:

$$\frac{\partial u(t,x)}{\partial t} = \frac{\partial}{\partial x}\left(u^n\left(t,x\right) \frac{\partial u\left(t,x\right)}{\partial x} \right) + u^l\left(t,x\right) . \qquad (2)$$

This equation is written in terms of dimensionless temperature and variables. On fig. 1 blow-up regimes for different parameters n and l are shown. As it could be seen for all of them focusing of temperature field energy are true. It gives a hope to use those regimes in local hyperthermia to prevent damage of normal tissue that surrounds tumor.

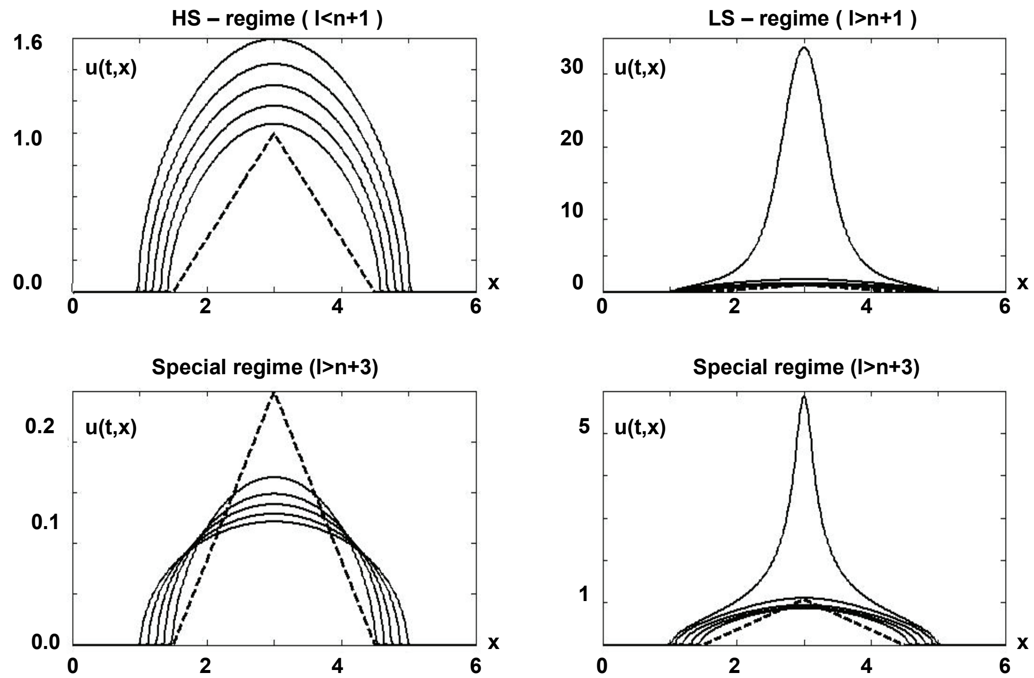

Fig. 1. Blow-up regimes of quasilinear hyperbolic heat transfer equation

Development and discussion. On fig.1 blow-up regimes for a case of one dimensional equation are presented. But in practical purposes to use blow-up regimes in hyperthermia three dimensional regimes are needed. As it was mentioned above increasing of dimensionality may prevent blow-up.

In this paper modeling of three dimensional heat transfer problem was made in spherical coordinate system regarding only radial component. The shape of equation is next:

$$\rho c\frac{\partial u(t,r)}{\partial t}=\frac{1}{r^2}\frac{\partial}{\partial r}\left(r^2\lambda(u,t,r)\frac{\partial u(t,r)}{\partial r}\right)+S(u,t,r). \quad (3)$$

Or it could be written after expanding brackets as follows:

$$\rho c\frac{\partial u}{\partial t}=\lambda\frac{\partial^2 u}{\partial r^2}+\left[\frac{2\lambda}{r}+\frac{\partial\lambda}{\partial r}+\frac{\partial\lambda}{\partial u}\cdot\frac{\partial u}{\partial r}\right]\frac{\partial u}{\partial r}+S(u,t,r). \quad (4)$$

Formally this equation differs from one dimensional case only because the term $\frac{2\lambda}{r}\cdot\frac{\partial u}{\partial r}$ is present. It couldn't be eliminated by itself because then thermal conductivity should be equal to zero identically. So below we regard a few tricks that could make equation (3) looks similar with equation (2) but first we rewrite (2) expanding brackets taking into consideration that $u^n(t,x)=\lambda(u)$:

$$\frac{\partial u(t,x)}{\partial t}=\lambda\frac{\partial^2 u(t,x)}{\partial x^2}+\left[\frac{\partial\lambda}{\partial u}\cdot\frac{\partial u(t,x)}{\partial x}\right]\frac{\partial u(t,x)}{\partial x}+u^l(t,x). \quad (5)$$

Here $\frac{\partial\lambda}{\partial r}\cdot\frac{\partial u}{\partial r}$ doesn't appear because λ is not a function of radial coordinate. Firstly, eliminate a term $\frac{2\lambda}{r}\cdot\frac{\partial u}{\partial r}$. It could be done with assumption:

$$\frac{2\lambda}{r}+\frac{\partial\lambda}{\partial r}=0. \quad (6)$$

Solving this equation gives:

$$\lambda=\frac{\lambda_0(u)}{r^2}. \quad (7)$$

Substituting (7) in (4) gives:

$$\rho c\frac{\partial u}{\partial t}=\frac{\lambda_0}{r^2}\frac{\partial^2 u}{\partial r^2}+\frac{1}{r^2}\left[\frac{\partial\lambda_0}{\partial u}\cdot\frac{\partial u}{\partial r}\right]\frac{\partial u}{\partial r}+S(u,t,r). \quad (8)$$

Supposing that $\rho c=\frac{\rho_0 c_0}{r^2}$, and $S(u,t,r)=\frac{u^l(t,r)}{r^2}$ we'll obtain equivalent to (5) equation:

$$\rho_0 c_0\frac{\partial u}{\partial t}=\lambda_0\frac{\partial^2 u}{\partial r^2}+\left[\frac{\partial\lambda_0}{\partial u}\cdot\frac{\partial u}{\partial r}\right]\frac{\partial u}{\partial r}+u^l(t,r). \quad (9)$$

There is no need to study its solutions because they are identical to solutions of a the well studied equation (5) especially for a case if $\lambda_0=u^n(t,r)$, nevertheless other functional dependencies of a heat conduction coefficient could be regarded.

In what follows two modifications of the equation (8) will be studied. The first one may be obtained if to (8) material parameters of the next shape will be substituted:

$$\rho c=\frac{1}{u^n};\ \frac{\partial\lambda}{\partial u}=0;\ \lambda=\frac{\lambda_0}{r^2};\ S(u,t,r)=S_0u^{l-n}. \quad (10)$$

Then the equation (8) will take a shape:

$$\frac{\partial u}{\partial t}=\frac{\lambda_0}{r^2}u^n\frac{\partial^2 u}{\partial r^2}+S_0u^l. \quad (11)$$

There is physical background for this shape of parameters. Biological tissue is a porous media [3], compressing it will eliminate gaps and should increase conductivity. Supporting gradient of pressure mechanically or via acoustic wave in the same time gradient of conductivity will be obtained. Temperature dependence of biotissue specific heat may be ensured by temperature dependence of water specific heat.

The second equation may be obtained from (8) via substituting materials parameters of the next shape:

$$\rho c=1;\ \lambda=\frac{\lambda_c u^n}{r^2};\ S(u,t,r)=S_0u^l. \quad (12)$$

Equation (8) will take a shape:

$$\frac{\partial u}{\partial t}=\frac{\lambda_c u^n}{r^2}\frac{\partial^2 u}{\partial r^2}+\frac{n\lambda_c}{r^2}\cdot u^{n-1}\cdot\left(\frac{\partial u}{\partial r}\right)^2+u^l. \quad (13)$$

The next step is to model numerically those two problems. But before results will be presented some explanations should be made. For one dimensional problem spatial coordinate possess the values from a set of real numbers and the beginning of axes may be shifted to any position, while for the case of a problem with spherical symmetry radial variable may possess the values only from a set of positive real numbers. And reference point couldn't be shifted arbitrarily it should be located in the center of symmetry. The range of possible values is $[0,R]$ where R is some constant value. It creates some difficulties, because point $r=0$ is the center of a heating region and in the same time is a point where boundary conditions should be specified. Both nor temperature nor heat flux couldn't be predicted in that point without knowledge about solutions. In order to solve this problem we use symmetrical reflection with a center in a reference point. Now the range of possible values is $[-R,R]$. Boundary conditions may be set as a constancy of temperature. It fits to the original problem to find regimes that could be used in local hyperthermia.

Functions that have singularities were modified during calculations and all singularities were replaced with average values of two adjacent points. It don't import any meaningful inaccuracy because in practice singularities are smoothed by nature.

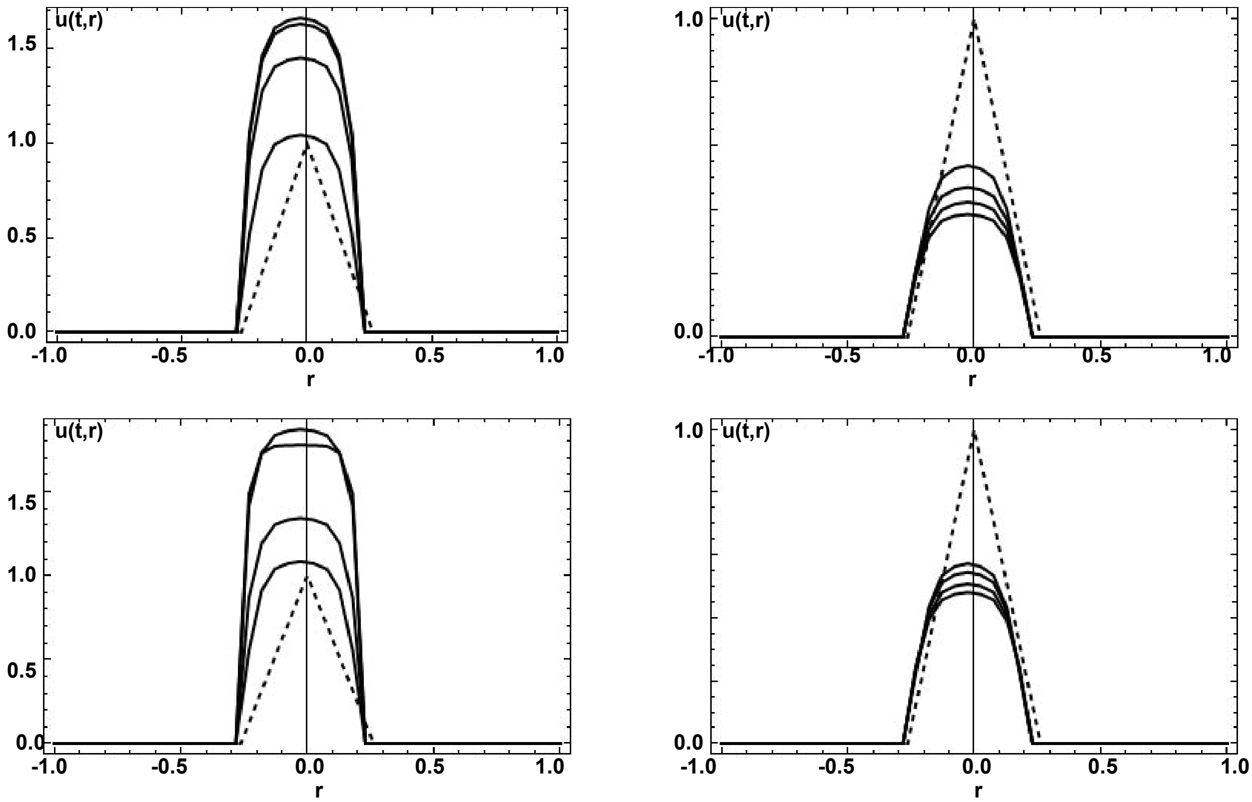

Fig. 2. Numerical solution of a 3-D heat transfer equation in spherical coordinates

On fig. 2 numerical solutions for equations (11) and (13) are shown. On the top left solution of the equation (11) with values of parameters $\lambda_0 = 10^{-3}$ $S_0 = 10^2$ $n = 2$ $l = 1$ and on the top right solution of the same equation with values of parameters $\lambda_0 = 10^{-3}$ $S_0 = 10^2$ $n = 1$ $l = 3$. On the bottom left solution of the equation (13) with values of parameters $\lambda_c = 10^{-3}$ $S_0 = 10^2$ $n = 2$ $l = 1$ and on the bottom right solution of the same equation with values of parameters $\lambda_c = 10^{-3}$ $S_0 = 10^2$ $n = 1$ $l = 3$. Dashed line shows initial conditions, they are the same for the all four cases. Continuous curves show an evolution of solutions in time. First of all, it should be mentioned that there is no big difference between solutions of equations (11) and (13). Both of them give two similar regimes as their solutions. The one that is located on the left side is similar to classical blow-up regime and is more perspective for application in local hyperthermia. Regime that is shown on the right side of fig.2 for both equations is similar to special regime $l > n+3$ on fig.1, but there is a principle distinction. It is obviously that in three dimensional case temperature field energy is decreasing while there is no any term corresponding to heat adsorption in equations. It is strange enough that such kind of solution is not physical. And also it reveals inconsistence of heat transfer equation with laws of thermodynamics. Maybe, this paradoxical solution is conditioned by singularity in heat conduction coefficient spatial dependence. This singularity is "unphysical" by itself. But it demands further investigation. Another difference between blow-up solutions of one dimensional equations and three dimensional equations is that there is no strike increase of temperature with time and it seems that solution do not converge to a infinity but to a some finite value. So these are not blow-up regimes in classical understanding, nevertheless those solutions are suitable for application in local hyperthermia.

Conclusions. It was shown that analogue of 1-D blow-up regime of quasilinear heat transfer equation exists also for 3-D case with spherical symmetry and demands heat conduction coefficient dependence of a radial component such that term describing spatial heat dissipation will be eliminated. Heat transfer equations of two shapes studied numerically obtained results were presented. It was shown that for 3-D equations blow-up regimes don't differ significantly. Only two solutions that differ meaningfully were found. Nevertheless 3-D blow-up regimes are suitable for application in local hyperthermia.

1. *Baronzio G. F., Hager E. D.* Hyperthermia in cancer treatment: a primer – NY: Springer, 2006. 2. *Lagendijk J.J.W.* Hyperthermia treatment planing // Phys. Med. Biol. – 2000. – Vol. 45. – P. 61–76. 3. *Nakayama A., Kuwahara F.* A general bioheat transfer model based on the theory of porous media // International Journal of Heat and Mass Transfer. – 2008. – Vol. 51. – P. 3190–3199. 4. *Tersenov A. S.* Space dimesion can prevent the blow-up of solutions for parabolic problems // Electonic Journal of Differential Equations – 2007. – Vol. 165. – P. 1–6. 5. *Самарский А.А., Галактонов В.А., Курдюмов С.П., Михайлов А.П.* Режимы с обострением. – М.: Наука, 1987.

Submitted on 31.05.2011

UDC 621.272.832.01

Yu. Gaidai, Ph. D., V. Sidorenko, Ph. D., O. Sinkevich, eng., Yu. Semenets, eng.

FORM PRESERVING REGULARIZATION IN NEAR-FIELD MICROWAVE MICROSCOPY INVERSE PROBLEMS

A modification of the Levenberg-Marquardt algorithm (LMA) for near-field microscopy inverse problems solving was analyzed. A method can be applied when the edges between homogeneous areas are known. It provides higher accuracy of quantitative restoration comparing to simple LMA implementation.
Keywords: near-field microscopy, regularization, a-priori information.

Розглянуто модифікацію алгоритму Левенберга-Марквардта для вирішення зворотніх задач у ближньопольовій НВЧ мікроскопії. Метод може бути застосований у випадку коли відомі границі між однорідними областями і забезпечує суттєво кращу точність відновлення матеріальних параметрів.
Ключові слова: ближньопольова мікроскопія, регуляризація, апріорна інформація.

Scanning near-field microwave microscopy (SNMM) is one of the most effective methods of dielectrics and semiconductors examination [1].

A lot of works were dedicated to microwave measurements schemes optimization and forward problems calculations from the electrodynamical point of view. But the conversion of the measured data to object's material properties is not always a trivial task, especially when investigating subsurface properties or some volumetric inhomogeneities of the object. Most of such problems are ill posed and require some regularizing algorithm to solve them. Furthermore, some properties of investigated object allow using conditional optimization when solving the inverse problem. A-priory information about an object can contain:

- Information about investigated defect type or its form (crack, exfoliation, bubble etc.)
- Information about object structure (film, ceramic evaporation etc.)
- A set of allowed permittivity values (problem close to pattern recognition)

This (or any other information) can seriously influence on the inverse problem solution accuracy.

Our main aim was to investigate the potential of the form preserving (FP) LMA for the quantitative solutions of SNMM inverse problems and compare accuracy of simple, form preserving and mixed regularization methods.

We propose a sensibly simple model for SNMM inverse problems solving using Levenberg-Marquardt algorithm with projection on given solutions range. In a general almost any inverse problem can be formulated as finding $\boldsymbol{\varepsilon}$ from

$$\mathbf{A}\boldsymbol{\varepsilon} = \mathbf{F}. \tag{1}$$

Here $\mathbf{A}$ is some forward problem operator. In our case $\boldsymbol{\varepsilon}$ is a permittivity vector, $\mathbf{F}$ is measured frequency shift and $\mathbf{A}$ can be calculated using some numerical SNMM model. For instance, we consider finite-difference model in quasistatic approximation.

Even in a linear approximation (where $\mathbf{A}$ is some constant matrix) $\boldsymbol{\varepsilon}$ can not be found as $\mathbf{A}^{-1}\mathbf{F}$ because of high condition number of $\mathbf{A}$ (i.e. $\mathbf{A}$ is ill-conditioned matrix). But we can modify (1) by introducing regularization parameter α

$$(\mathbf{A}^{\mathrm{T}}\mathbf{A} + \alpha\mathbf{I})\,\boldsymbol{\varepsilon} = \mathbf{A}^{\mathrm{T}}\mathbf{F}. \tag{2}$$

and find $\boldsymbol{\varepsilon}$ as

$$\boldsymbol{\varepsilon} = (\mathbf{A}^{\mathrm{T}}\mathbf{A} + \alpha\mathbf{I})^{-1}\mathbf{A}^{\mathrm{T}}\mathbf{F}. \tag{3}$$

Finally, to improve solution accuracy we can use iterative procedure (Levenberg-Marquardt iterations)

$$\boldsymbol{\varepsilon}_{i+1} = \boldsymbol{\varepsilon}_i + (\mathbf{A}^{\mathrm{T}}\mathbf{A} + \alpha\mathbf{I})^{-1}\mathbf{A}^{\mathrm{T}}(\mathbf{F}_i - \mathbf{F}_i^E). \tag{4}$$

Where $\mathbf{F}_i^E$ is frequency shift measured in experiment and $\mathbf{F}_i$ – data calculated on computer model at current iteration.

Such algorithm works fine but there is a problem with ε values such that ε < 1. Actually, its not a problem for the algorithm (it stays stable and convergent) but for quantitative restoration its better to limit possible ε range. We applied projection operator

$$P_{\mathrm{E}}(\varepsilon) = \begin{cases} \varepsilon, & 1 \le \varepsilon \le \varepsilon_{\max} \\ 1, & 1 > \varepsilon \\ \varepsilon_{\max}, & \varepsilon > \varepsilon_{\max} \end{cases} \tag{5}$$

at each iteration:

$$\boldsymbol{\varepsilon}_{i+1} = P_{\mathrm{E}}\left(\boldsymbol{\varepsilon}_i + (\mathbf{A}^{\mathrm{T}}\mathbf{A} + \alpha\mathbf{I})^{-1}\mathbf{A}^{\mathrm{T}}(\mathbf{F}_i - \mathbf{F}_i^E)\right). \tag{6}$$

Projection operator application is well known from the conjugate gradients projection method. But it its application directly to Levenberg-Marquardt iterations gives also good results.

We also found that with respect to SNMM inverse problem such approach gives better results when compared with simple restoration (without conditional optimization).

It is however not always possible to obtain SNMM inverse problem solution with required accuracy. But in the case when the inhomogeneity edge is known (for instance, it can be obtain optically) the accuracy of the permittivity restoration can be increased significant [2]. Considering, that $\varepsilon = \varepsilon_S = const$ inside of some region S we can form regularization matrix $\mathbf{R}$ (instead of identity matrix $\mathbf{I}$ in (4)) that will "correspond" to object's structure.

Elements of $\mathbf{R}$ can be written like

$$r_{ij} = \begin{cases} \alpha_S, & i = j \\ -\alpha_S / N_S, & \{i,j\} \in S \\ 0, & otherwise \end{cases} \tag{7}$$

where N_S is a number of elements in area S, α_S – regularization coefficient for area S. Our approach differs from

[2], where $\alpha_S \equiv 1, \forall S$. By using different regularization coefficients for different regions we apply smaller α_S values in areas with undefined edges and larger α_S for areas with known edges.

Using $\mathbf{R}$ in (4) leads to smoothing of restored values inside of an area S. Final formula for permittivity restoration can be written:

$$\boldsymbol{\varepsilon}_{i+1} = \boldsymbol{\varepsilon}_i + (\mathbf{A}^{\mathrm{T}}\mathbf{A} + \alpha\mathbf{R})^{-1}\mathbf{A}^{\mathrm{T}}(\mathbf{F}_i - \mathbf{F}_i^E) \qquad (8)$$

Fig.1 shows the model of the test sample (a) (which was used for form preserving restoration method work through) and its scan result (b). A test sample was made from polypropylene ($\varepsilon \approx 2.5$) film with air grooves.

A scan image was obtained using near-field microwave microscope with an active probe [3].

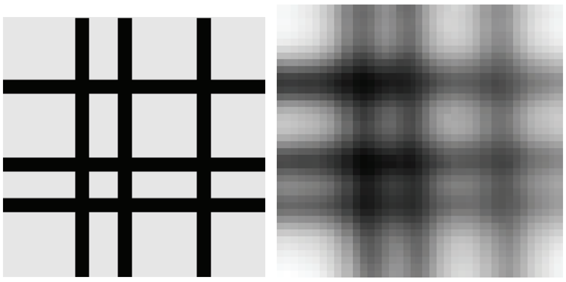

a) b)

Fig. 1. Test sample model (a) and scan result (b)

On can see that form preserving restoration (or "soft prior regularization", as it called in [2]) can be very effective for solving SNMM inverse problems.

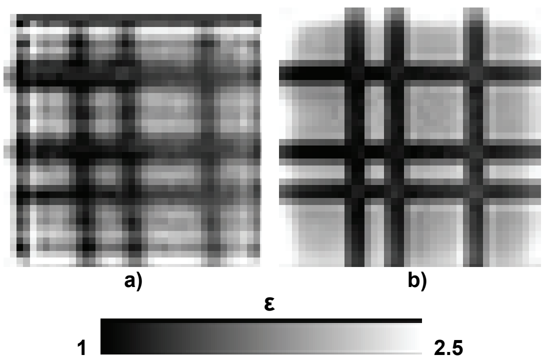

Fig. 2. A result of simple LMA restoration (a) and form preserving restoration (b)

It may seems enough to just "fill" area within known edges with some permittivity value and reduce the problem to picking optimal ε values within these areas. But if not all edges are known such approach will fail while proposed method will behave correctly (like if identity matrix was used). This, however, requires suitable regularization coefficients α_S selection. For areas with known and sharp edges α_S can be several orders higher than for the rest areas. Such approach works fine because "image sharpness" is provided by regularization matrix structure and greater α_S value provides smoothing inside the constant permittivity areas.

For method accuracy estimation the residual between measured and calculated data is often used. In our case it could be scanned and calculated images difference. But as we know $\varepsilon(x,y)$ for the real sample, we can calculate restoration error for N*M image as

$$\Delta\varepsilon = \frac{\sqrt{\sum_{n,m}(\varepsilon_{n,m}^r - \varepsilon_{n,m}^o)^2}}{NM}, \qquad (9)$$

where $\varepsilon_{n,m}^r$ – restored ε value at point {n,m} and $\varepsilon_{n,m}^o$ - original value.

But restoration error is not only parameter suitable for method accuracy estimation. Another important factor is image quality. It is well known that total error can be small while restored data can be noisy and do not correspond to real object data. It's hard to represent image quality quantitatively in general case (different histogrammic, spectral, entropy and other criteria are used), but again, as we know initial $\varepsilon(x,y)$ we can use correlation coefficient (between restored and original data):

$$\rho(\varepsilon^r, \varepsilon^o) = \frac{\sum_{n,m}(\varepsilon_{n,m}^r - \overline{\varepsilon}^r)(\varepsilon_{n,m}^o - \overline{\varepsilon}^o)}{\sqrt{\sum_{n,m}(\varepsilon_{n,m}^r - \overline{\varepsilon}^r)^2}\sqrt{\sum_{n,m}(\varepsilon_{n,m}^o - \overline{\varepsilon}^o)^2}}. \qquad (10)$$

We found that these two values ($\Delta\varepsilon$ and $\rho(\varepsilon^r,\varepsilon^o)$) depend differently on regularization parameter α for different restoration techniques.

Table 1 represents this dependence for simple LMA and form preserving regularization.

Table 1. **Restoration error and correlation coefficient for simple and FP LMA**

α	$\Delta\varepsilon$ **(simple)**	$\Delta\varepsilon$ **(FP)**	$\rho(\varepsilon^r,\varepsilon^o)$ **(simple)**	$\rho(\varepsilon^r,\varepsilon^o)$ **(FP)**
10^{-1}	0.0290	0.0203	0.4285	0.9999
10^{-2}	0.0289	0.0109	0.4309	0.9999
10^{-3}	0.0275	0.0077	0.4510	0.9996
10^{-4}	0.0212	0.0079	0.5290	0.9829
10^{-5}	0.0159	0.0105	0.5987	0.8899
10^{-6}	0.0154	0.0135	0.6048	0.7325
10^{-7}	0.0166	0.0158	0.6029	0.5674
10^{-8}	0.0193	0.0188	0.3391	0.3774

It's worth to mention that for simple LMA both $\Delta\varepsilon$ and $\rho(\varepsilon^r,\varepsilon^o)$ reach their optimal value at $\alpha \sim 10^{-6}$ (this also corresponds to our subjective "image quality" estimation). At the same time, for form preserving regularization optimal α value is $\sim 10^{-3}$ and correlation coefficient decreases monotonically with α reduction. Visually, image quality is also optimal at $\alpha = 10^{-3}$ (although it is almost the same until $\alpha > 10^{-5}$). So, we conclude that for a test objects with known $\varepsilon(x,y)$ correlation coefficient $\rho(\varepsilon^r,\varepsilon^o)$ corresponds fine to visual image quality estimation and can be used for its quantitative analysis.

We also found that FP regularization provides better absolute values restoration accuracy $\Delta\varepsilon$ (0.0077 using FP regularization against 0.0154 using simple LMA). Furthermore, $\Delta\varepsilon$ is better for any α value and some lower value can be used to avoid unnecessary smoothing.

We also tested FP regularization algorithm for volumetric inhomogeneities defectoscopy. By choosing the restoration grid in the form of slices in XY plane we can restore subsurface (or 3D) permittivity distribution (for this experiment we used only two layers). A simple test sample with volumetric inhomogeneities was made (Fig. 3) and scanned at a few different probe/sample distances (0 mkm and 350 mkm).

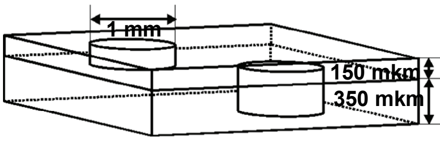

Fig. 3. Test sample for 3D permittivity restoration

Resulting data were processed with the same algorithm, as described below (LMA with projection and form preserving). This time, however, we used mixed restoration mode. As surface layer structure can be known and subsurface most likely not, we used FP LMA for top layer and simple LMA for bottom layer. Regularization parameters were different for different modes ($\alpha = 10^{-6}$, $\alpha_S = 10^{-3}$).

Restoration result is show in Fig.4. Overall restoration error for simple LMA was 0.022 (0.051 for bottom layer) and 0.02 (0.04 for bottom layer).

Conclusion

It was shown that form preserving regularization provides higher accuracy of SNMM inverse problem solution. This is true for both 2D and 3D problems. Also, we have found that the knowledge of all edges between uniform areas is not necessary and the accuracy will grow with each correct edge definition. Optimal regularization parameter also depends on the information we have about inhomogeneities. In the case when all edges are known, regularization parameter can be chosen several orders higher then using simple regularization procedure.

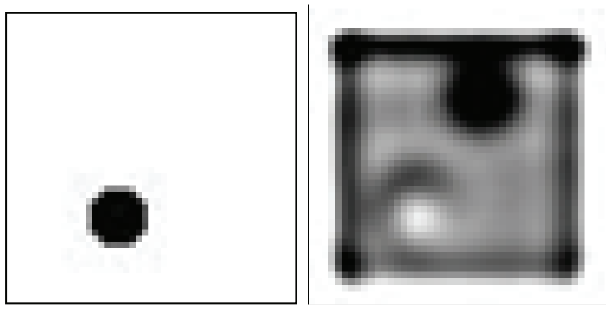

a) **b)**

Fig. 4. Layers restoration result:
a) – surface layer (FP LMA);
b) – subsurface layer (simple LMA)

Proposed method can be succesfully used for 3D inhomogeneities defectoscopy. Since we can define surface layer structure (from optical microscopy or in some other way) it will improve the accuracy of the subsurface layer restoration.

1. *Steinhauer D. E., Vlahacos C. P., Wellstood F. C.* // Rev. Sci. Instrum. – 2001. – Vol. 71, № 7. 2. *Golnabi A., Meaney P., Geimer S., Fanning M., Paulsen K.* // Proc. of SPIE. – 2009. – Vol. 7262. 3. *Гайдай Ю.О., Сидоренко В.С., Сінькевич О.В.* Ближньопольовий мікроскоп для дослідження дисперсії діелектричної проникності // Вісник Київського національного університету ім. Т. Шевченка. Радіофізика та Електроніка. – 2008. – Вип. 11. – С. 16–18.

Submitted on 20.05.2011

UDC 544.723.232

Y. Gulaga, stud., V. Il'chenko, Dr. Sci.,
O. Kravchenko, Ph. D., M. Shyshkin, stud., V. Telega, Ph. D.

KINETICS INVESTIGATION OF RESPONSE TO CHANGING GAS ENVIRONMENT OF THE SEMICONDUCTOR HETEROSCTRUCTURE SnO_2 – Si

The kinetics of current through gas sensitive heterostructure SnO_2 – Si as a n-p-heterojunction were investigated. It was shown that the adsorption or desorption of water molecules from the surface of heterostructure under the influence of constant voltage can be divided into 2 subprocesses: fast and slow. The time constant of these subprocesses differs by about ten times of each other.

Keywords: heterostructure, adsorption, desorption, steady time.

У роботі досліджувалася кінетика струму через газочутливу гетероструктуру, яка являє собою n-p-гетероперехід SnO_2 – Si. Було показано, що процес адсорбції або десорбції молекул води з поверхні гетероструктури під дією сталої напруги можна розділити на 2 підпроцеси: швидкий та повільний зі значеннями сталих часу, які відрізняються на порядок.

Ключові слова: гетероструктура, адсорбція, десорбція, стала часу.

Introduction. Analysis of the gas environment is an important problem in many areas: in research, industry, household, medicine, ecology and more. In such cases you need the unit, whose purpose – to transform a particular gas concentration into an electric signal. Actual is the creation of high-speed, low-cost gas sensors that do not require high electricity costs during the operation. The aim of this work was to study the kinetics of adsorption and desorption on the surface of gas sensible semiconductor heterostructures.

Experimental technique. Gas sensible heterostucture used in experimental research, is n-p-junction: tin dioxide is used as a semiconductor with electronic conductivity, p-silicon – as a semiconductor with hole conductivity. SnO_2 – Si was put in the form of strips with a maximum thickness of 100nm on silicon wafers 0.3mm thickness by magnetron sputtering. As ohmic contacts used nickel and aluminum, which were deposited by magnetron sputtering. In Fig. 1. heterostructure is shown in cross-section.

As atmosphere were used air at 100% humidity and air dried with liquid nitrogen, at the room temperature 18°C. Experimental device provided measuring of the dynamic and current-voltage characteristics of heterostructures using a PC. Device scheme is presented in Figure 2.

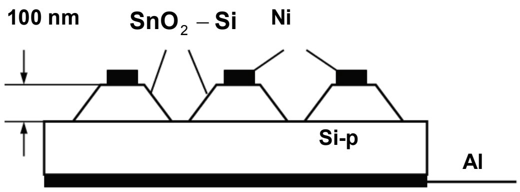

Fig. 1. Scheme of experimental heterostructure

The feature of used methods are pulsed (cyclical) power supply of heterojunction. This provides power cycling unit 4, which gives the voltage on the heterostructure for 2s with pause at 10s.

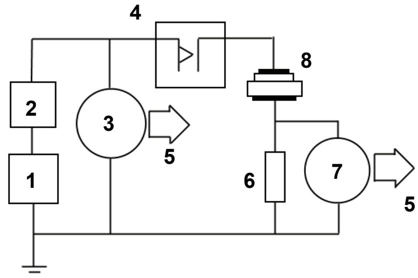

Fig. 2. Device scheme: 1 – power supply; 2 – bias block; 3 – measuring unit UT 70B; 4 – power cycling; 5 – interface; 6 – measuring resistance; 7 – measuring unit UT 70B; 8 – heterostructures

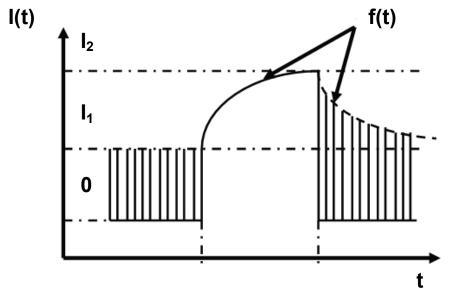

Fig. 3. Time dependence of current on the sensor

Experimental results. For quantitative analysis of gassensible heterostructures performance were obtained dependences of the current through the heterojunction on time of adsorption and desorption. Typical of such dependence graph is shown in Fig. 3.

Until the time $t = t_1$ rectangular pulses with a period of 10s, duration of 2s and amplitude –2V are applied, in time $t = t_1$, a constant voltage –2V is provided to the heterostructure, resulting in heterojunction water molecules are gathered and current increases.

Using the software package Origin Pro, it was discovered that the best current kinetics are approximated by the sum of two exponentials:

$$f(t) = A\left[1-\exp\left(-t/\tau_1\right)\right]+ +B\left[1-\exp\left(-t/\tau_2\right)\right]+I_1,\ \tau_2 >> \tau_1. \qquad (3)$$

At the point of time $t = t_2$ sensor should almost completely saturate so $t_2 - t_1 \cong (2 \div 3)\tau_2$. Since that point of time rectangular pulses are applied on a sensor, envelope curve represents sensor purification from adsorbate and should be approximated with the same formula. Results obtained in experiments with 100% humid air and air dried with liquid nitrogen, are shown below (Fig. 4-7).

By comparing the obtained numerical constant time, it is clear that with adsorption and desorption differ more than an order of magnitude, which indicates the existence of 2 separate subprocesses, which differ in speed of order. Here are the dependencies and calculated values for different conditions (Figure 4-7).

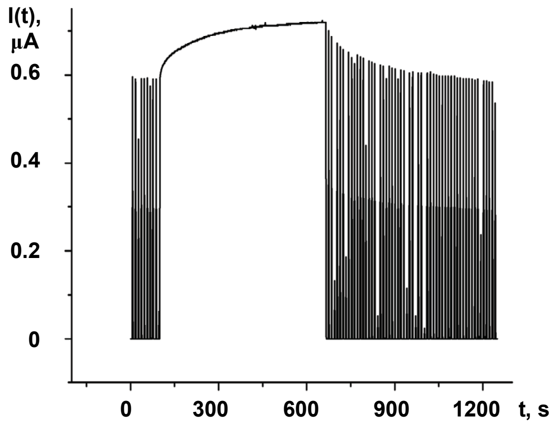

Fig. 4. Humid air. Adsorption: $\tau_1 = 11.7$ s ; $\tau_2 = 164$ s . Desorption: $\tau_1 = 15.7$ s ; $\tau_2 = 183$ s

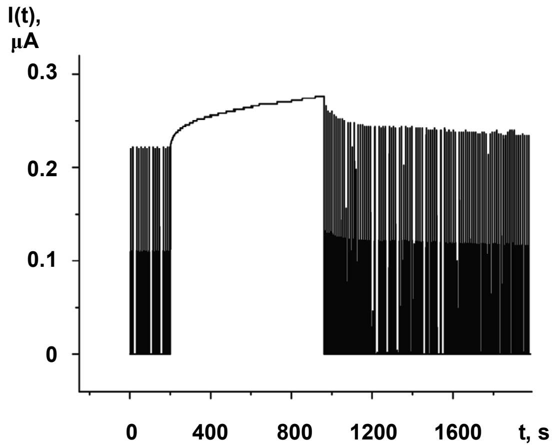

Fig. 5. Dry air. Adsorption: $\tau_1 = 36$ s ; $\tau_2 = 619$ s . Desorption: $\tau_1 = 20$ s ; $\tau_2 = 237$ s

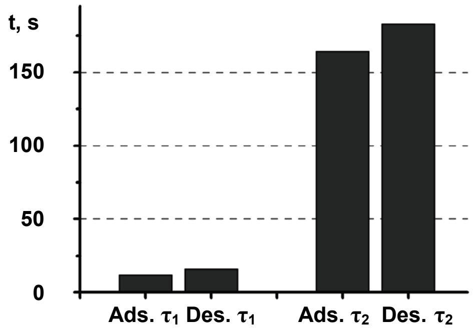

Fig. 6. Comparative diagram of time constants for adsorption and desorption in an environment of air with 100% humidity

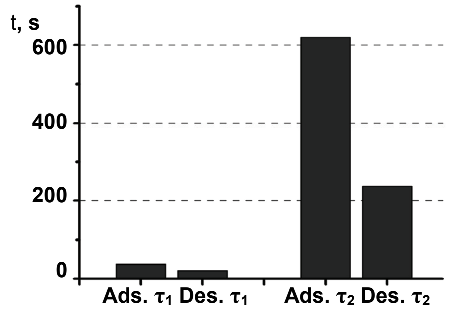

Fig. 7. Comparative diagram of steady time for adsorption and desorption in an environment of air, drained liquid nitrogen

Taking into consideration this and the fact that the gas that affects the heterostructures was water vapor, because water molecules have a dipole moment in comparison with other components of air and a high enough partial pressure (at 18°C and 100% humidity – 5.15Torr.) we can make the assumption that some water molecules involved in faster adsorption (desorption) on the surface, the other diffuses deep into the porous tin dioxide. A similar effect is observed for air-dried, but the absolute values of time several times larger, because the concentration of water molecules is considerably smaller than in the previous case.

Conclusions. Response constant time of nanosized semiconductor heterostructures SnO_2 – Si can be determined by two processes: rapid adsorption on the surface and slower diffusion in order molecules deep into the porous tin dioxide.

The effect should be taken into account when choosing the topology heterojunction sensor based on SnO_2 – Si.

1. *Bomk O. I., Il'chenko V. V., Kuznetsov G. V., Strikha V. I., Pinchuk A. M., Pinchuk V. M.* About the gas sensitivity of contacts metal – silicon with the superthin nickel and titanium films to the ammonia environment // Sensors and Actuators B. Chemical. – 2000. – Vol. 62. – P. 131–139. 2. *Morimitsu M., Ozaki Y., Suzuki S., Matsunaga M.* Effects of surface modification with platinum and ruthenium on temperature and humidity dependence of SnO – based CO gas sensors // Sensors and Actuators B. – 2000. – Vol. 67. – P. 184–188. 3. *Peka P., Striha V.I.* Surface and contact phenomena in semiconductors. – K.: Libid, 1992. – 240 p. 4. *Vasiliev R.B., Gaskov A.M., Rumyantsev M.N. et al.* Properties of heterodiode-type structures based on nanocrystal n-SnO_2 on p-Si in terms of gas adsorption. – Moscow State University, Russia, 2000. 5. *Vasilev R.B.* Thin films and heterostructures based on nanocrystal metal oxides for gas sensors. Abstract of the thesis on scientific degree of Candidate of Chemical Sciences. – M., 2001. – 115 p.

Submitted 13.05.2011

UDC 519.9

O. Ilchehko, post. grad. stud., V. Obukhovsky, Dr. Sci., V. Lemeshko, Ph. D., V. Nikonova, post. grad. stud., A. Kutsyk, stud.

THE CONTRIBUTION OF WATER CLUSTER VIBRATION MODES IN RAMAN SPECTRUM

The analysis of quantum-chemical calculations for small clusters of water (one to six molecules in the complex) was performed. The regions in the spectrum where shape broadening of the valence band vibrations of hydroxyl OH-groups corresponds to specific types of the clusters were selected. The shape of the band in the region 2800 – 3300 cm^{-1} is formed mainly by trimers, tetramers, pentamers and gexamers and the shape of the band in the region 3300 – 3800 cm^{-1} is formed mainly by dimmers, trimers and tetramers. Trimer is the most common water cluster at the room temperature. Its contribution to the valence vibration band of hydroxyl OH-groups is 51% relatively to the other clusters.

Key words: Raman scattering, valence OH-vibrations of water, hydrogen bond, cluster, the contribution of vibration modes.

Проведено аналіз даних квантово-хімічних розрахунків для малих кластерів води (від однієї до шести молекул в комплексі). Виділені ділянки в спектрі, де за уширення форми валентної смуги коливань гідроксильних ОН-груп відповідають певні типи кластерів. Частина контуру в інтервалі частот від 2800 – 3300 см$^{-1}$ утворена переважно тримерами, тетрамерами, пентамерами та гексамерами, а інша частина, в інтервалі частот від 3300 см$^{-1}$ до 3800 см$^{-1}$ утворена переважно димерами, тримерами і тетрамерами. При кімнатній температурі найбільш розповсюдженим є тример води, його внесок у спектр валентної смуги коливань гідроксильних ОН груп складає 51% відносно внеску інших кластерів води.

Ключові слова: Комбінаційне розсіювання, валентні ОН-коливання води, водневий зв'язок, кластер, внесок коливальних мод.

Introduction. The Investigation of structural formations in liquid water is becoming increasingly relevant today. Effects of long-term "memory" of water, changing its electrical and physical parameters in the interaction with low-frequency magnetic field still remain without explanation [6]. Liquid water has the largest number of known physical anomalies among liquids, for example: a negative volume of melting, density maximum at 4ºC, isothermal compressibility minimum at 46ºC, very high melting, boiling and critical temperature, high heat of vaporization, high constant-pressure heat capacity, high dielectric constant, decreasing viscosity with increasing pressure and the effect of temperature on the intensity distribution in the stretching vibration region of the Raman spectra of liquid water.

Historically, there are two competing and, to some extent, complementary theoretical approaches used to describe the molecular structure of liquid water. Generally, they are represented by the continuum (uniform) models and the mixture (cluster) models. Both categories make use of some experimental properties of water and a great deal of intuition. Unfortunately, though the countless models put forward, over more than a century, none can adequately fit both the physical properties and the available structural data.

In the early 1960s the high resolution Raman technique became available and the spectral band shapes have since been carefully analysed to find evidence for the mixture theory. The spectroscopic model of Walrafen [7] involves nonhydrogen-bonded monomeric water and lattice water. According to Walrafen, the experimentally demonstrated existence of isosbestic points in both the isotropic and anisotropic Raman spectra of liquid water constitutes strong evidence for a mixture model of water involving at least two different structural components. In several other spectroscopic studies, the Raman spectra were also interpreted in favour of the mixture models [1,3].

With the advent of supercomputers more rigorous quantitative studies on water structure could be performed based on quantum and statistical mechanics. Various molecular interaction potentials for the water molecule (fitted either to results of ab initio calculations or to empirical data) have been used, together with powerful computational techniques, such as the Monte Carlo or Molecular Dynamics method. The first computer "experiment" of this type was carried out by Rahman and Stillinger [5] with a model of 216 water molecules. This study can be regarded as a turning point in the theoretical approach. Since that time, the need for classic continuum and mixture models has been overcome by the possibility of performing more rigorous analyses via the molecular simulation techniques. A number of new models have been published over the past two decades, in which more and more complicated structural units were suggested as the building blocks for liquid water, including aggregates of water in ice-like arrangements discussed by Luck [2], a network of hexagonal, pentagonal and dodecahedral arrays or a fluctuating arrangement of 14-molecule tetrahedral units, leading to the formation of three-nanometer 280-molecule expanded icosahedral clusters. Naturally, with the growing size of basic structural units believed to constitute liquid water, the fundamental differences between mixture and continuum theories have become meaningless and are now semantic rather than based on physical arguments.

The purpose of this work was to evaluate contributions of vibrational modes of small water clusters in the formation of the valence band vibrations of hydroxyl OH-groups in Raman spectrum. These data will help to make conclusions about the cluster structure of liquid water.

Experiment. The distilled water, which purity was controlled by the absence of impurities nitrates and heavy metals was used in research.

The modernized and automated spectral-computing system based on double monochromator DFS-52 (Fig. 1) has been used. The comparison channel was added to registration scheme (the change of laser radiation intensity was taken into account). Both channels transmit data to the computer through an analog-digital converter. The software building Raman scattering spectrum on these data has been designed. Panoramic spectra within the range 2800... 3800 cm^{-1} with a spectral resolution of 2 cm^{-1} were recorded when registering a consistent signal. Accumulation time of the spectrum record amounted to a range of 40 minutes.

Argon laser (wavelength 488 nm, power 80 mW) was used as a source exciting the Raman scattering. Heating the sample during the measurement of Raman scattering spectra did not practically occur, due to small value of absorption coefficient under excitation frequency.

Scattered light is observed at 90 ° relatively to the direction of incident laser beam. The spectra were recorded with the width of input and output gaps, which did not exceed 200 μ. The temperature of liquid samples was within the range 293 ÷ 294 K.

Results and Discussion. A part of the spectrum of Raman scattering in water within the range 2800-3800 cm^{-1} is shown in Figure 1.

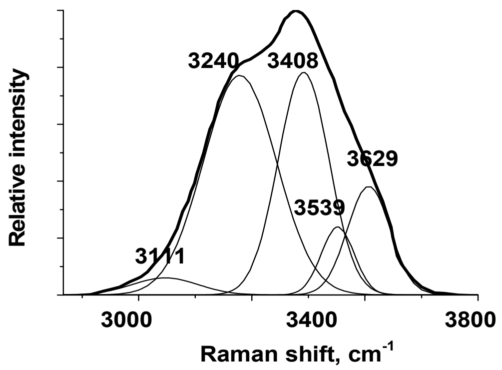

Fig. 1. Raman scattering spectra for water-ethanol mixture at different concentrations of ethanol

Broad line describes the shape of the spectrum, and the narrow lines break the contour shape for the gauss components. The contour was decomposed by five Gaussian components. This is the minimum number of components that are necessary to describe the valence vibration band of hydroxyl OH-groups. The authors calculated the frequency and intensity corresponding to the possible valence vibrations of OH groups for different types of clusters in the work [4]. The obtained values turned out in the range of experimentally measured valence band vibrations of hydroxyl OH groups in water. If we attach the Lorentz broadening to the each of the theoretically derived peaks, we can satisfactorily describe both form of valence vibrations of OH hydroxyl groups and its change at different temperatures of water.

The data of quantum-chemical simulation of small water clusters (n = 1,2,.. 6) in [4] were used to assess the contribution of vibrational modes in the valence band of hydroxyl OH groups for each of the five Gaussian components. For this purpose the intensities of vibrational modes of a certain cluster types were normalized to their concentration in liquid water at T = 20°C. The next step was to determine the proportional contribution of each normalized intensity of the vibrational modes of the cluster in a separate Gaussian component. The percent contribution of the each type of the cluster in a separate Gaussian component is represented in the table 1.

Table 1. **The concentration contribution of each type of cluster in a separate Gaussian component of the valence band vibrations of hydroxyl OH-groups of water**

n	3111 cm^{-1},%	3240 cm^{-1},%	3408 cm^{-1}, %	3539 cm^{-1}, %	3629 cm^{-1}, %
1	0	0	0	0,28	0,61
2	0	0	0,97	19,44	2,1
3	0	13,33	91,45	38,9	36
4	34,7	52	1,7	11,57	30,4
5	44,2	27,62	0,08	8,2	23,08
6	21,1	7,05	5,8	21,61	7,83

Thus the largest contribution in the lowest-frequency Gaussian component with the central frequency 3111 cm^{-1} makes pentamers (~44%). The largest contribution in the Gaussian component with the central frequency 3240 cm^{-1} make tetramers (~52%), the largest contribution in the Gaussian component with the central frequency 3408 cm^{-1} make trimers (~91%), the largest contribution in the Gaussian component with the central frequency 3539 cm^{-1} make trimers (~39%) and the largest contribution in the most high-frequency Gaussian component with the central frequency 3629 cm^{-1} make also trimers (~36%).

From Table 1 we can see that the contribution of monomer concentration in the five Gaussian component is very small. Therefore we can neglect it. The concentration contribution of water dimers largely was manifested only in the high region in the Gaussian component with the central frequency 3539 cm^{-1}. This contribution was ~19%.

Some theoretical calculations of the diffusion process in aqueous solutions [18] require the approximation model of liquid water in the form of only one type of clusters. It follows from the analysis carried out by the authors that trimer is the most common water cluster at the room temperature. Its contribution to the valence vibration band of hydroxyl OH-groups is 51% relatively to the other clusters.

Conclusions. The cluster model, which considers liquid water as a set of cluster types $(H_2O)_n$, n = 1, 2,...6 was used to interpret the formation mechanism of vibration band of hydroxyl OH-groups of water. Deconvolution of this band into five Gaussian components was carried out to study in detail the influence of the vibrational modes of small water clusters on the valence band of hydroxyl OH-groups in the Raman spectrum. The data of quantum-chemical simulation for small water clusters (n = 1,2,.. 6) in [4] were used to assess the contribution of vibrational modes to the valence band of hydroxyl OH groups for each of the five Gaussian components.

The regions of the spectrum where shape broadening of the valence band vibrations of hydroxyl OH-groups corresponds to specific types of the clusters were selected. The shape of the band in the region 2800 – 3300 cm^{-1} is formed mainly by trimers, tetramers, pentamers and gexamers and the shape of the band in the region 3300 – 3800 cm^{-1} is formed mainly by dimmers, trimers and tetramers.

Trimer is the most common water cluster at the room temperature. Its contribution to the valence vibration band of hydroxyl OH-groups is 51% relatively to the other clusters.

1. *Durig, J. R., Gounev, T. K., Nashed, Y., Ravindranath, K., Srinivas, M., & Rao, N. R.* On the Raman spectra of liquid water as a function of temperature // Asian J. Spectrosc. – 1999. – Vol. 3(4). – P. 145–154. 2. *Luck, W. A. P.* Water in biological systems // Topics Curr. Chem. (Inorganic Biochemistry). – 1976. – Vol. 64. – P. 113–180. 3. *Luu, C., Luu, D. V., Rull, F., & Sopron, F.* Etude par effet Raman de la perturbation structurale de l'eau liquide par une substance etrangere. Partie I. Modele d'association de l'eau liquide // J. Mol. Struct. – 1982. – Vol. 81(1-2). – P. 1–10. 4. *Maciej Starzaka, Mohamed Mathlouthi.* Cluster composition of liquid water derived from laser-Raman spectra and molecular simulation data // Food Chemistry. – 2003. – Vol. 82. – P. 3–22. 5. *Rahman, A., & Stillinger, F. H.* Molecular dynamics study of liquid water // J. Chem. Phys. – 1971. – Vol. 55(7). – P. 3336–3359. 6. *Vysotskii V. I., Kornilova A. A.* Physical Model and Direct Experimental Observation of Water Memoryand Biophysical Activity of Magnetic-Activated Water // Journal of Scientific Exploration. – 2009. – Vol. 23, № 4. – P. 500–505. 7. *Walrafen, G. E.* Raman spectral studies of the effects of temperature on water structure // J. Chem. Phys. – 1967. – Vol. 47(1). – P. 114–126.

Submitted 07.06.2011

UDC 535

N. Kachalova, Ph. D., V. Voitsekhovich, Ph. D.,
V. Khomenko, post grad. stud., R. Pilgun, stud.

QUASI-DISCRETE SPECTRAL FEMTOSECOND SUPERCONTINUUM INVESTIGATION

An interference signal of two spectral supercontinua derived from a single source was experimentally investigated. Appearance of a quasi-discrete structure was detected on the whole spectrum length of supercontinuum from 550 to 900 nm. The distance between adjacent spectral maxima of quasi-discrete spectral femtosecond supercontinuum is proved to be inversely proportional to the time delay between pulses of supercontinua.

Key words: supercontinuum, photonic crystal fiber, femtosecond laser.

Експериментально зареєстровано сигнал інтерференції двох суперконтинуумів, отриманих від одного джерела. Спостережено появу квазідискретної структури в спектральному діапазоні від 550 до 900 нм. Досліджено поведінку інтерференційного сигналу в залежності від часу затримки між сигналами. Отримано обернено пропорційну різницю частот між інтерференційними піками від часової затримки.

Ключові слова: суперконтинуум, фотонно-кристалічне волокно, фемтосекундний лазер.

Introduction. Femtosecond laser systems allow to research a time-dependent spectrum broadening, when the width of the spectrum becomes comparable to its central frequency [7]. This is also called the spectral supercontinuum (SC) generation. This kind of spectrum widening can be achieved in various transparent media, if a duration of pumping pulses lay in a femtosecond range. The spectral supercontinuum generation has been originally observed in 1970 by passing picosecond pulses through bulk media [1]. Due to the progress in the development of new femtosecond lasers and the appearance of new waveguides this phenomenon still being actively investigated [7;9].

Up to date, the number of papers dedicated to the researches of pulse interaction in nonlinear media and their interference at the output of a nonlinear media is actively increasing [4,8]. In particular, the quasi-discrete structure of spectrum has been observed at a superposition of two SC generated independently by different femtosecond pulse [2]. Such structure can be interpreted as multiple individual radiation sources with different central frequencies. The use of the spectral supercontinuum interference effect can lead to laser systems creation with fundamentally new properties. Sources of radiation with a quasi-discrete wide spectrum can become a promissory basis of creating new frequency standards and modern super-fast data transfer systems, and have proved themselves to be useful in spectroscopic and nano-technical applications [3].

The aim of this paper includes analyse of the quasi-discrete supercontinuum spectral characteristics, obtained from the interference of pulses with wide continuous spectrums and investigation of controlled pulse parameters.

Experimental setup. In papers [5,6] is reported about creation of a femtosecond supercontinuum source based on the Ti:Sa laser Mira Optima 900 – F and series of microstructured photonic – crystal fibers (PCF). Results of spectral characteristics analysis were also introduced in those papers. The supercontinuum source, created for our experiment, is based on 20 cm length PCF-H 071015_125. The pump radiation, generated by the femtosecond Ti:Sa laser, has the following characteristics: pulse duration – 150 fs, central wavelength – 800 nm, average power – 500 mW at the PCF input. The diagram of the experimental setup is shown on Fig. 1.

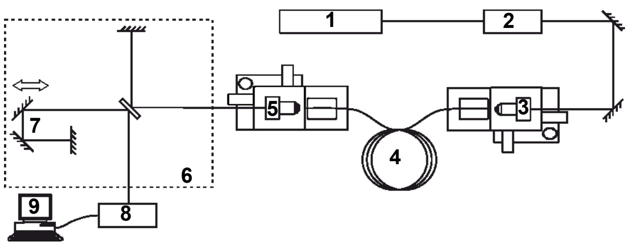

Fig. 1.The experimental setup for interference signal registration: 1 –femtosecond Ti: Sapphire laser Mira Optima 900 – F; 2-Faraday isolator; 3 –objective lens; 4 – PCF; 5 – collimator lens; 6 – Michelson interferometer; 7 – delay line; 8 – spectrometer Ocean Optics USB 4000; 9 – personal computer

The radiation of the Ti:Sa laser (1) passed through optical isolator, in order to avoid a disruption of the laser generation. Such isolator operates on the Faraday effect, and has an attenuation of inverse beam (> 91 %). Using mirrors and 20X objective lens (3) with a numerical aperture of 0.4, the radiation was directed into the core of PCF (4) with a diameter of 2.5 mkm. Shaping of nondivergent beam at the output of fiber, was performed using the collimator lens (5). Afterwards, the SC beam entered to Michelson interferometer (6), with a delay line (7) formed by aluminum mirrors with a spectral reflectance range of 400 – 10000 nm. This beam was divided into two coherent beams of equal intensity by a translucent beam splitter. Each one of them passed its own optical path in interferometer arms and recombined providing an interference pattern formation. The shape of the interference pattern depends on the optical path difference. Control of an optical path difference was provided by a micrometer screws with 5 μm step, what equals to 17 fs delay. The interference signal registration was held by a spectrometer Ocean Optics USB 4000 (8).

Results and analysis. The supercontinuum spectrum obtained at the output of PCF (Fig. 2) covers range from 550 nm to 900 nm.

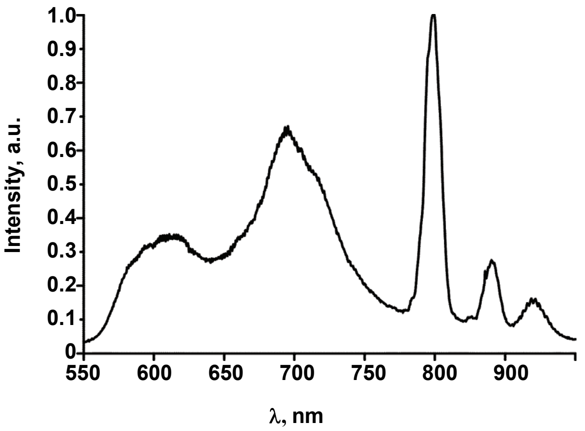

Fig. 2. Supercontinuum spectrum generated in 20 cm microstructured fiber by pumping femtosecond Ti: Sapphire laser

Series of experimental supercontinuum interference spectrums for various time delays between impulses are shown on Fig. 3.

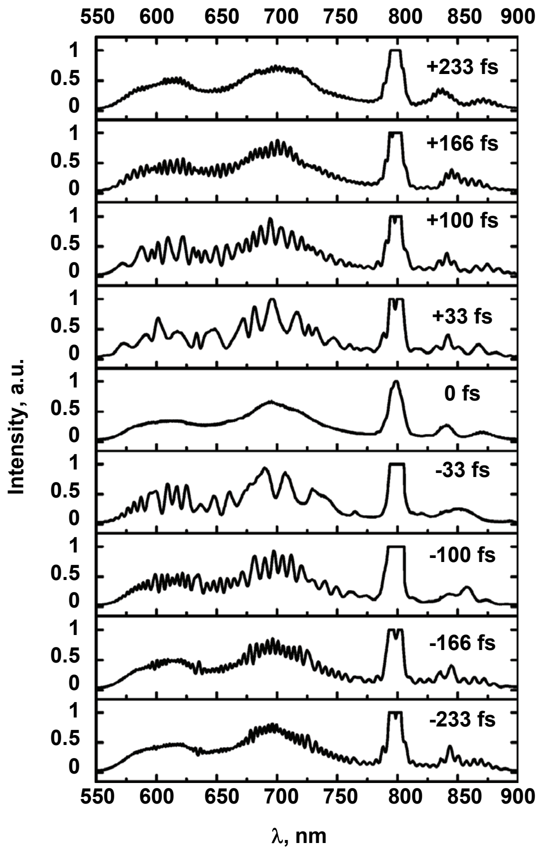

Fig. 3. Broadband spectrum with quasi-discrete structure derived from interference of two supercontinuums. Values of time delays between pulses are following: +233 fs, +166 fs, +100 fs, +33 fs, 0, -33 fs, -100 fs, -166 fs, -233 fs

As it appears from Fig. 3, the spectrum corresponding to a zero delay between pulses, has a similar form to a spectrum of recombined non-coherent beams and matches with initial SC. An estimate shows that a frequency difference between nearest spectral maxima is inversely related to a path length difference $\Delta\omega \propto 1/\Delta t$, here $\Delta\omega$ – frequency difference between spectral maximums, Δt – temporal interval between interfering pulses. Obtained experimental results are in a good correspondence with a theory.

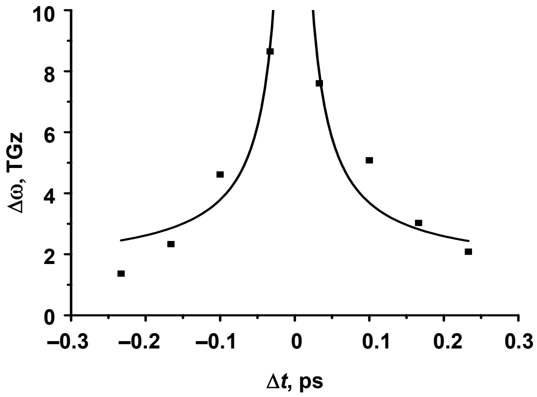

Fig. 4. Inverse dependence of frequency difference between spectral maxima on temporal interval between interfering pulses: experimental – points, theoretical – solid curve

Conclusions. The appearance of the quasi-discrete structure of the supercontinuum spectrum was observed experimentally by means of interference of pulses with wide spectra. It testifies about spatial coherent of interfering supercontinuum pulses.The following dependence was obtained experimentally: increasing of a time delay between interfering pulses leads to a decrease of a spectral distance between adjacent maxima. An estimate shows that the frequency difference between nearest spectral maxima is inversely related to a delay between pulses $\Delta\omega \propto 1/\Delta t$, here $\Delta\omega$ – frequency difference between spectral maxima, Δt – time interval between interfering pulses.

A comprehensive program of fundamental research NASU "Fundamental problems of nanostructured systems, nanomaterials, nanotechnologies" supported the experiment on 2010-2014 years.

1. *Alfano R.R., Shapiro S.L.* Emission in the region 4000 to 7000 Å via four-photon coupling in glass // Phys. Rev. Lett. – 1970. – Vol. 24, № 11. – P. 584–587. 2. *Bakhtin M.A., Kozlov S.A.* Generation of the discrete spectral supercontinuum in twointensive ultrashort pulses interaction // Optical Memory and Neural Network – 2006. – Vol. 15, № 1. – P. 1–10. 3. *Bakhtin M.A., Bespalov V.G., Krylov V.N., Shpolyanskiy Yu. A., Kozlov S. A.* Ultrafast information transmission by quasi-discrete spectral supercontinuum // Advances in Information Optics and Photonics – 2008. – P. 405–423. 4. *Dudley J.M., Genty G., Coen S.* Supercontinuum generation in photonic crystal fiber // Rev. Mod. Phys. – 2006. – Vol. 78, № 11. – P. 1135–1184. 5. *Kachalova N.M., Voitsekhovich V.S., Borodin A.M., Yatsenko L.P.* Investigation of possibilities to control femtosecond supercontinuum characteristics // Ukrainian Journal of Physics. – 2010. – Vol. 55, N. 9. – P. 961–965. 6. *Kachalova N.M., Voitsekhovich V.S., Khomenko V.V.* Supercontinuum generation in photonic crystal fibers // Bulletin of Taras Shevchenko national university of Kiev. Series: Physics & Mathematics. – 2010. – N. 4. – P. 279–283. 7. *Ranka J.K., Windeler R.S., Stentz A.J.* Visible continuum generation in air-silica microstructure optical fibers with anomalous dispersion at 800 nm // Opt. Lett. – 2000. – Vol. 25, № 1. – P. 25–27. 8. *Shpolyanskiy Yu.A., Belov D.L., Bakhtin M.A., Kozlov S.A.* Analytic study of continuum spectra pulse dynamics in optical waveguides // Appl. Phys. B. – 2003. – Vol. 77, № 2-3. – P. 349-355. 9. *Zheltikov A.M.* Supershort Impulses and Methods of. Nonlinear Optics: Textbook. – M., 2006.

Submitted on 17.05.2011

UDC 533.9

A. Knurenko, post grad. stud., E. Martysh, Dr. Sci.

THE ANALYSIS OF EARTH'S GEOMAGNETIC ACTIVITY FOR THE K-INDEX IN APRIL AND MAY OF 2011

The study of the solar wind and Space Weather interaction with planetary magnetospheres basically is the investigation of the physics of flowing magnetized plasmas. Space Weather is the set of conditions on the Sun and in the solar wind, magnetosphere, ionosphere and thermosphere that can influence the performance and reliability of space-borne and ground-based technological systems and can endanger human life or health. Space Weather on the Earth is manifested as geomagnetic activity.

Geomagnetic activity can be divided into two main categories: substorms and storms. Magnetic storms are relatively rare phenomena. Geomagnetic activity can be represented in the form of so called K-index. The K-index is a code that is related to the maximum fluctuations of horizontal components observed on a magnetometer relative to a quiet day.

The features of K-index function for magnetic field fluctuations in the Earth's magnetosphere on different time scales were investigated using data of NOAA / Space Weather Prediction Center program. Changes of shape and parameters of the K-index function for the periods of geomagnetic activity were studied.

Key words: Space Weather, geomagnetic activity, magnetosphere, solar wind, plasma.

Взаємодія сонячного вітру, космічної погоди з магнітосферою Землі зводиться в основному до вивчення процесів в намагніченій плазмі. Космічна погода зумовлена багатьма факторами, такими як процеси що відбуваються при взаємодії потоку сонячного вітру з магнітосферою, іоносферою і термосферою Землі. Ці процеси в свою чергу можуть вплинути на продуктивність праці космічних і наземних технологічних систем. Також зміна геомагнітної активності може викликати загрозу життю або здоров'ю людини.

Геомагнітна активність може бути розділена на дві основні категорії: суббурі і бурі. Магнітні бурі є відносно рідкісними явищами. Геомагнітна активність може бути представлена у вигляді K-індексу. K-індекс – код, який пов'язаний з максимальною амплітудою коливання горизонтальної складової магнітного поля Землі у відносно спокійний день.

В роботі проаналізовано зміну K-індексу на протезі двох місяців – квітень, травень 2011року. І показано які типи збурень мали місце в цей період і які наслідки були в буденному житті.

Ключові слова: Космічна погода, геомагнітна активність, магнітосфера, сонячний вітер, плазма.

Introduction. When using appellation "space weather", one should keep in mind conditions in space that are changing from time to time. Sometimes the Sun gives off more radiation and solar wind, sometimes it gives off less. The speed and the pressure of solar wind change all the time. Space is filled with magnetic fields, which control the motions of charged particles of the solar wind. The strengths and directions of the magnetic fields are shifting often. So, changes in radiation, the solar wind, magnetic fields, and other factors make up space weather.

Most of space weather parameters start at the Sun. The large amount of energy the Sun gives off is what makes space weather occurred. Sometimes there are storms on the Sun, called solar flares and Coronal Mass Ejections (CMEs). These storms fling showers of radiation and powerful magnetic fields outward through in the Solar System.

Space Weather is the concept of changing environmental conditions in near-Earth space. It is distinct from the concept of weather within a planetary atmosphere, and deals with phenomena involving ambient plasma, magnetic fields, radiation and other matter in space. "Space Weather" often implicitly means the conditions in near-Earth space within the magnetosphere, but it is also studied in interplanetary space [1].

The magnetosphere of Earth. The magnetosphere of Earth is a region in space whose shape is determined by the Earth's internal magnetic field, the solar wind plasma, and the interplanetary magnetic field (IMF) [2]. In the magnetosphere, a mix of free ions and electrons from both the solar wind and the Earth's ionosphere is confined by electromagnetic forces that are much stronger than gravity and collisions. Despite its name, the magnetosphere is distinctly non-spherical. All known planetary magnetospheres in the solar system possess more of an oval tear-drop shape because of the solar wind. On the side facing the Sun, the distance to its boundary (which varies with solar wind intensity) is about 70,000 km (10-12 Earth radii or R_E, where 1 R_E = 6371 km; unless otherwise noted, all distances here are from the Earth's centre). The boundary of the magnetosphere ("magnetopause") is roughly bullet shaped, about 15 R_E abreast of Earth and on the night side (in the "magnetotail" or "geotail") approaching a cylinder with the radius of 20-25 R_E. The tail region stretches well past 200 R_E, and the way it ends is not well-known.

Figure 1 illustrates the magnetosphere of Earth.

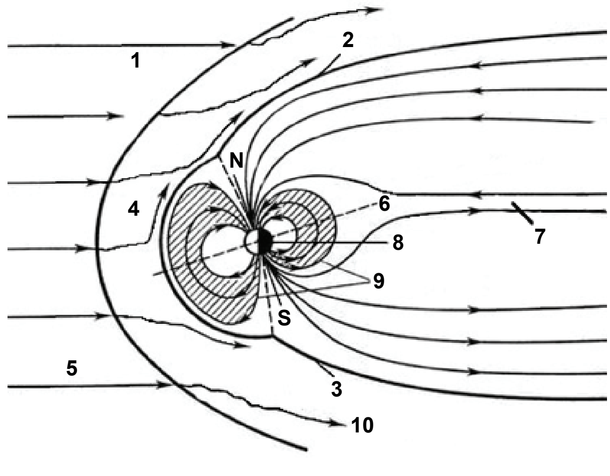

Fig. 1. The magnetosphere of Earth: 1 – Bow Shosk; 2, 3 – Magnetopause; 4 – Transition region; 5 – Solar wind; 6 – Plane of geomagnetic equtor; 7 – Neutral layer; 8 – Earth; 9 – Radiation belts; 10 – Magnetosheasth

Geomagnetic substorms and storms. Geomagnetic activity can be divided into two main categories: substorms and storms. Geomagnetic storms are major disturbances of the magnetosphere that occur when the interplanetary magnetic field turns southward and remains southward for an prolonged period of time. During a geomagnetic storm's main phase, which can last as long as two to two and a half days in the case of a severe storm, charged particles in the near-Earth plasma sheet are energized and injected deeper into the inner magnetosphere, producing the storm-time ring current. This phase is characterized by the occurrence of multiple intense substorms, with the attendant auroral and geomagnetic effects. When the interplanetary field turns northward again, the rate of plasma energization and inward transport slows and the various loss processes that remove plasma from the ring current can begin to restore it to its pre-storm state.

Substorm:

- common events, happening all the time, with more frequency at solar maximum, but also at solar minimum.
- manifestation as perturbation of the geomagnetic field and auroral display.
- they develop over periods of an hour.
- regular solar wind conditions are sufficient, typically triggered by switch of the IMF from northward to southward (i.e. B_z is negative), but not always.

Storm:

- much more rare and strongly linked to the solar cycle, with the number of storms following the same temporal variation as the number of sunspots.
- manifestation as sudden increase of the geomagnetic field.
- they last for a few days.
- peculiar conditions in the solar wind cause it (stronger impact of the ejection from the Sun on the magneto-sphere).

The K-index. Having understood the nature of a geomagnetic substorm, which is also known as a magnetosphere substorm, it's helpful to start from the very beginning. Substorms are short lived (2-3 hours) magnetospheres disturbances which occur when the interplanetary magnetic field turns southward, which permits interplanetary and terrestrial magnetic field lines to merge at the dayside magnetopause and energy to be transferred from the solar wind to the magnetosphere. Simply, space weather of the Earth is the fluctuation of the geomagnetic activity. Classification for geomagnetic storms has 5 types. Each of them is described in the table 1.

Table 1. **Space Weather Scale for Geomagnetic Storms**

Category		Kp values*	nT
Scale	Descriptor		
G 5	very extreme	Kp = 9	>500
G 4	Extreme – Severe	Kp = 8	330-500
G 3	Strong	Kp = 7	200-330
G 2	Moderate	Kp = 6	120-200
G 1	Minor	Kp = 5	70-120

The official planetary Kp index is derived by calculating a weighted average of K-indices from a network of geomagnetic observatories.

The K-index is a code that is related to the maximum fluctuations of horizontal components observed on a magnetometer relative to a quiet day, during a three-hour interval. The conversion table from maximum fluctuation (nT) to K-index, varies from observatory to observatory in such a way that the historical rate of occurrence of certain levels of K are about the same at all observatories.

We monitor the preliminary values of the K-index, minute by minute, and we notify our rapid alert customers when we exceed critical thresholds of 6, 7, and 8. The final real-time K-index is determined after the end of prescribed three hourly intervals (0000-0300, 0300-0600,..., 2100-2400) and is used on our announcements and appears on our web site. The maximum positive and negative deviations during the 3-hour period are added together to determine the total maximum fluctuation. These maximum deviations may occur anytime during the 3-hour period and is being calculated as the relationship between K, Kp.

Geomagnetic activity in April. (by data of National Oceanic and Atmospheric Administration's (NOAA) USA.

The features of K-index function for magnetic field fluctuations in the Earth's magnetosphere on different time scales were investigated using data of NOAA / Space Weather Prediction Center program. Changes of shape and parameters of the K-index function for the periods of geomagnetic activity were studied. Figure 1 illustrates Kp-index of Earth's geomagnetic activity fluctuations in April of 2011. NOAA / Space Weather Prediction Center program data has been used in calculations.

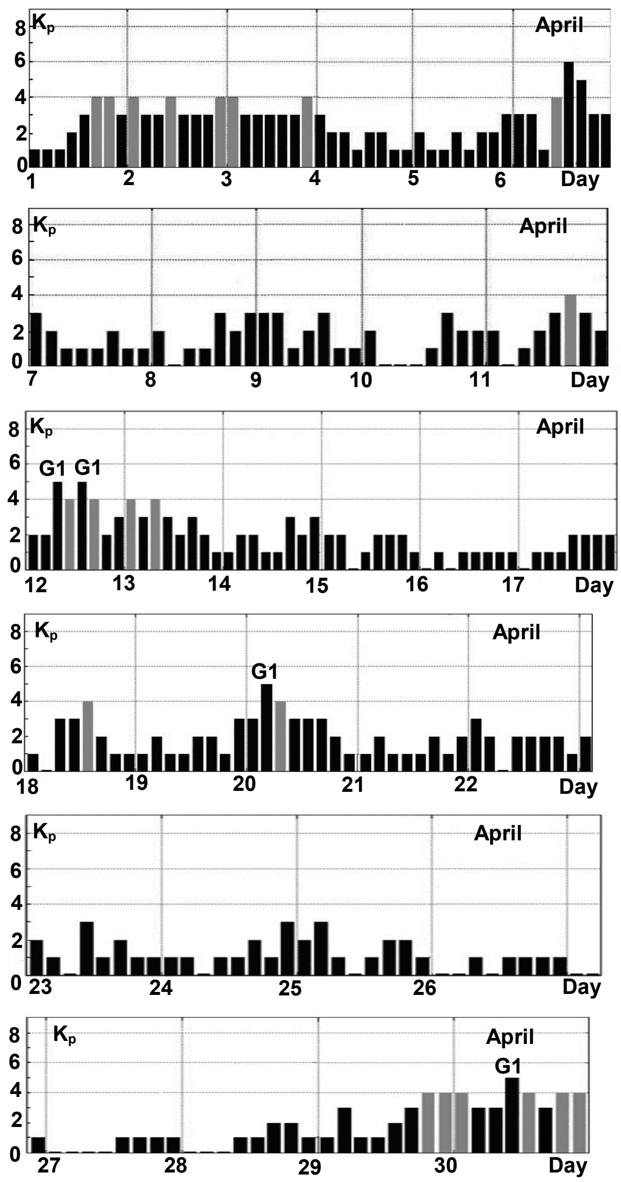

Fig. 2. The geomagnetic activity fluctuations in April of 2011

The analysis of geomagnetic fluctuations on Earth in April 2011 showed that this month, in terms of geomagnetic activity, was relatively quiet. There were four geomagnetic bursts, which led to the magnetic storms of type G1 and G2. This corresponds to the fluctuations of Earth's magnetic field from 70 to 200 nT.

Geomagnetic activity in May (by data of National Oceanic and Atmospheric Administration's (NOAA) USA. Kp-index of Earth's geomagnetic activity fluctuations in May of 2011 **illustrates of Figure 3,** using data of NOAA / Space Weather Prediction Center program.

The analysis of geomagnetic fluctuations on Earth in May 2011 showed that this month, in terms of geomagnetic activity, was relatively quiet. There were five geomagnetic bursts, which led to the magnetic storms of type G1 and G2. This corresponds to the fluctuations of Earth's magnetic field from 70 to 200 nT.

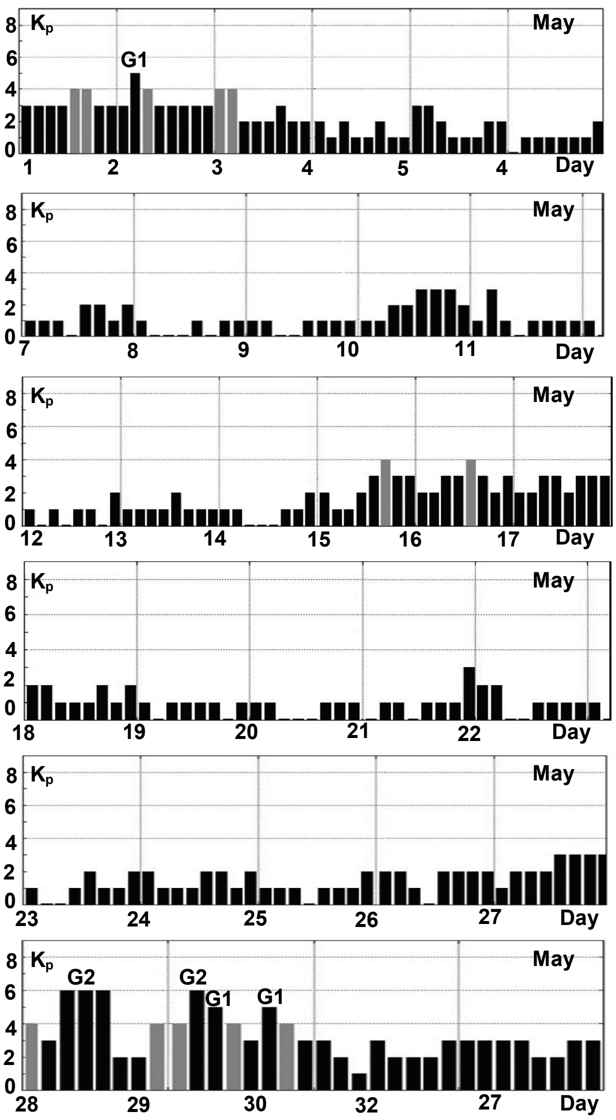

Fig. 3. The geomagnetic activity fluctuations in May of 2011

G1, minor [4]**.** Power systems are weak, power grid fluctuations may occur. Spacecraft operations are minor impact on satellite operations possible. Other systems: migratory animals are affected at this and higher levels. Values Kp is equal 5. Kp values for the type of storm G1 is shown in Fig. 2, 3.

G2, moderate. Power systems are high-latitude and may experience voltage alarms, long-duration storms may cause transformer damage. Spacecraft operations are corrective actions to orientation may be required by ground control; possible changes in drag affect orbit predictions. Other systems:

HF radio propagation can fade at higher latitudes. Values Kp is equal 6. Kp values for the type of storm G2 is shown in Fig. 2, 3.

Degradation in mobile communications and minor malfunctions in the television and radio has been seen in the days after the geomagnetic bursts.

Also, it was observed the worsening of health of the people, which are sensitive to the changes of geomagnetic activity. Particularly, it happened during periods from 2nd to 4th and from 28th to 31st of May.

Conclusions. The analysis of geomagnetic fluctuations on the Earth in April and May 2011 showed that these months in terms of geomagnetic activity were relatively quiet. There were eleven geomagnetic bursts which led to the magnetic storms of type G1 and G2.

Also, it was observed the worsening of health of the people who are sensitive to the changes of geomagnetic activity in these months. The number of people who applied for medical assistance has doubled. If during a normal day the number of calls is close to 1400-1500, then during the day with high geomagnetic activity it reaches 2200-2400. Those who have heart problems and cardiovascular system taken up to 60 percent of the mentioned count.

Despite the fact that these months have been quiet loss of quality of mobile communication, television and radio signals had been taken place.

1. *Clark T. D. G., and Clarke E.* Space weather services for the offshore drilling industry // Space Weather Workshop: Looking Towards a Future European Space Weather Programme. ESTEC, ESA WPP-194. – 2001. 2. *Knurenko A.I., Martysh E.V.* Comparison of planetary magnetospheres // IX international young scientists' conference on applied physics, Taras Shevchenko National University of Kyiv, Radiophysics Faculty, June, 17-20, 2009, Kyiv, Ukraine. – P. 91. 3. National Oceanic and Atmospheric Administration's (NOAA). – http://www.swpc.noaa.gov. 3. *Mullan, Dermott J.* Physics of the Sun: A First Course. – Taylor & Francis, 2009. – 450 p. 4. *Knurenko A.I., Martysh.E.V., Sidorenko V.S.* Space Weather and Processes in the Earth's Magnetosphere // Bulletin of Taras Shevchenko National Univ. Ser. Radio Physics & Electronics. – 2011. – Iss. 15. – P. 34–36.

Submitted on 15.06.2011

UDC 533.9

A. Knurenko, post grad. stud., E. Martysh, Dr. Sci.

FASTER-THAN-DIFFUSION MAGNETIC FIELD PENETRATION INTO PLASMA

The interaction of a moving plasma cloud (also called a plasmoid) with a magnetic barrier is discussed. The fast penetration of magnetic fields into plasmas is needed in definite set of magnetosphere parameters. A possible mechanism, based on the formation of small-scale density fluctuations that lead to field penetration via the Hall mechanism, is presented. The penetration occurs in nonuniform plasmas of a characteristic length smaller than the ion skin depth, it is much faster than the ion motion, and its rate is independent of the resistivity.

Key words: magnetosphere, solar wind, plasma.

Обговорюється взаємодія плазмової хмари, що рухається (її також називають плазмоїд) крізь магнітний бар'єр. Швидке проникнення магнітного поля є необхідним для цілого ряду магнітосфер них параметрів. Представлений можливий механізм цього явища, який базується на формуванні малих неоднорідностей плазми, що призводить до швидкого проникнення поля за допомогою ефекту Холла. Проникнення відбувається в неоднорідній плазмі з характерним розміром неоднорідності меншим від довжини іонного скін-ефекту. Це значно швидше іонного руху, а його швидкість не залежить від опору плазми.

Ключові слова: магнітосфера, сонячний вітер, плазма.

Introduction. Plasma structures, here typified by the term 'plasmoids', in the solar wind impacting on the magnetopause, i.e. the boundary between the solar wind and the Earth's magnetosphere, can penetrate this boundary and be injected into the magnetosphere. Solar wind determines the large-scale structure of the magnetic field of Earth to a high extent. The basic structural components are transition regions and regions between them:

1. At the bow shock the solar wind arriving at a supersonic velocity of 500 km/s encounters Earth's magnetic field and is transformed to a subsonic flow and dissipates energy inside magnetosheath where the plasma is denser and hotter than in the solar wind. The distance of the bow shock is roughly 12-14 R (R denotes Earth's radius).

2. The shocked solar wind cannot penetrate Earth's magnetic field and a cavity called magnetosphere is formed. Interplanetary magnetic field and and magnetosphere is separated by a transition region called magnetopause, which is accompanied by a plasma mantle.

At the day side magneto-pause is at distance of about 10 R but when solar wind is particularly strong in can move down to 6-7 R. At the night side magnetosphere is stretched into long cylindrical magneto-tail of length about 1000 R and radius about 20 R. Magnetosphere consists of clearly separated regions with widely different densities and temperatures. The main division is into inner and outer magnetosphere. In the inner magnetosphere magnetic field lines are co-rotating with the Earth: in the outer magnetosphere they are stationary. Magneto-pause contains an ionic current determined by the discontinuity of the magnetic field and orthogonal to it.

The penetration process can happen either by expulsion of the magnetic field from the structure and subsequent diffusion of the magnetic field into the structure or by the formation of a polarization electric field that lets the plasma structure $\vec{E}\times\vec{B}$-drift into the Earth's magnetic field. In both cases a collisionless resistivity is required at some stage of the process. While magnetic expulsion requires electromagnetic models for its description, polarization can be modelled electrostatically and both processes can be and have been studied in laboratory experiments [1]. In laboratory plasmas it is demonstrated in magnetic fusion devices, theta pinches, ion diodes, plasma switches, and in plasma–beam transport across magnetic fields [2]. In space and astrophysics, plasma transport across magnetic fields is studied not only in relation to the interaction of the solar wind with the Earth's magnetic field, but in the evolution of solar flares, the coronal heating, and in accretion discs [3].

Due to the low plasma collisionality, the magnetic field dynamics in such phenomena are not dominated by classical diffusion. Moreover, it was found that in low-density plasma, the magnetic signal propagates without noticeable plasma compression [3]. For some configurations it has been suggested that the rapid field penetration into the plasma results from an instability-induced anomalous collisionality. For another configuration (a reversed-field theta pinch) an explanation based on magnetic tearing and reconnection has been suggested, while in yet another configuration rapid magnetic field penetration due to the Hall field has been demonstrated.

Dynamics of the magnetic field in magnetosphere plasma. Plasmoid penetration across magnetic barriers has been the subject of the series papers [4-5]. Several interlocking processes are important for the penetration mechanism. Here, we will focus on only one of them, anomalous fast magnetic field diffusion. Fig. 1 shows the magnetic diffusion mechanism schematically in a case where it is comparatively slow, so that different phases can be distinguished. A plasmoid (a fast plasma cloud) is here assumed to have penetrated into a region with a transverse magnetic field. The magnetic field diffusion into the plasmoid goes though three phases. First, a diamagnetic phase where the transverse magnetic component is excluded from the plasmoid by a diamagnetic current loop around the edge. Second, a diffusion phase where the magnetic field diffuses into the cloud and, third, a propagation phase when the magnetic field has fully diffused into the plasmoid, which is able to continue its motion because it has self-polarized to the $\vec{E}=-(\vec{v}/c)\times\vec{B}$ field strength. The parameter of interest is surveyed in terms of three energy densities also: the directed kinetic energy density $W_k = nmv^2/2$ in the plasmoid (n, v are plasma density and velocity respectively), the electric field energy density $W_E = E^2/8\pi$ in a polarized plasmoid (here $\vec{E}=-(\vec{v}/c)\times\vec{B}$ is the self-polarization electric field) and the magnetic energy density $W_B = B^2/8\pi$ of the transverse field into which the plasma is attempting to penetrate.

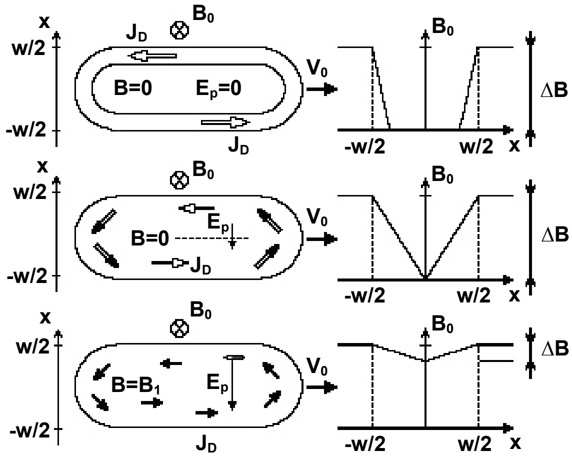

Fig. 1. The penetration of magnetic fields into a moving plasma cloud (or plasmoid) in three phases. (a) Diamagnetic exclusion of the field. (b) Diffusion of the field. (c) Continued plasmoid propagation by the *E*×*B* drift

With usage of magnetosperic parameters from [4], someone can concludes that the magnetic diffusion time must be of the same order as the transition time, and thus about a factor 100 faster than classical. (A comment might be necessary here. We claim that magnetic field diffusion of some kind is necessary for a plasmoid to enter a region with a transverse magnetic field, in such a fashion that the plasmoid keeps is general shape, velocity, and orientation, and the transverse field penetrates the plasmoid. We motivate this claim in the rest frame of the plasmoid. In this frame, the plasma cloud is stationary and is subject to a time-changing transverse magnetic field. For the magnetic field to penetrate the plasma, some magnetic diffusion process is clearly necessary)

If classical magnetic diffusion is too slow, some anomalous process is needed. There are two fundamentally different types of mechanisms which can give anomalous fast magnetic penetration into a plasmoid: violation of the frozen-in condition due to parallel (magnetic field-aligned) electric fields, or enhanced magnetic diffusion on the micro-scale, by waves or turbulence.

The action of the waves is thus identical to the action of electron-ion collisions in the sense that it represents a momentum exchange between ions and electrons, in the direction of the macroscopic current. The role of electron-ion collisions in magnetic diffusion is to dissipate the current, and allow magnetic field penetration. The waves should therefore have a similar effect.

The idea that parallel electric fields can arise in the vicinity of cross-B-moving plasmoids was first proposed in connection with ionospheric injection experiments [5]. Parallel electric fields on the edges of a moving plasma cloud were proposed to partly screen the internal self-polarization field $\vec{E}=-(\vec{v}/c)\times\vec{B}$ from the ambient medium.

This weakens the frozen-in condition and allows a plasmoid injected in the ionosphere to move across B without dragging along all ambient plasma in the magnetic flux tube. This is the mechanism invoked by Delamaire (see [4]) to explain anomalous long skidding distances observed in the ionospheric CRRES releases of Barium clouds.

We here focus on the resulting anomalous magnetic field diffusion into the plasma cloud, two orders of magnitude faster than classical, which is one important aspect of the plasma cloud penetration mechanism. Without such fast magnetic diffusion, clouds with kinetic bk below unity would not be able to penetrate magnetic barriers at all.

The evolution of a magnetic field in a plasma, derived from Faraday's law, generalized Ohm's law, and Ampére's law with neglect of the displacement current can be expressed by:

$$\frac{\partial \vec{B}}{\partial t} = rot\left[\vec{v}_i \times \vec{B}\right] - rot\left[\vec{j} \times \vec{B} / en_e\right] + {c^2}\big/{4\pi\sigma}\,\Delta\vec{B}, \qquad (1)$$

where the first term on the right hand side is the convection term, the second is the Hall term and the third is the diffusion term. Here, v_i is the ion velocity, n_e is the electron density, e is the electron charge, j is the current density, B is the magnetic field, $1/\sigma$ is the resistivity. If the Hall and diffusion terms are neglected (likely to occur in relatively dense and/or uniform plasmas and in low resistivity plasmas) the magnetic field is frozen into the ion fluid. In this case the dominant process is expected to be plasma pushing by the $\vec{j} \times \vec{B}$ force. The Hall term is expected to be dominant for scale lengths $L = \left[d\ln(n)/dx\right]^{-1}$ that are smaller than the ion inertial length, i.e., $L \ll c/\omega_{pi}$, where ω_{pi} is the ion plasma frequency and c is the speed of light.

The Hall term can lead to a drift wave mode that can rapidly transport magnetic flux in an inhomogeneous plasma. In a detailed picture of this process we can assume that the electrons are drifting in quasineutral plasma, while the ions are not magnetized and motionless.

We assume again that the magnetic field has one component only in the ignorable coordinate y. Equation (1) is then reduced to:

$$\frac{\partial B}{\partial t} = -\frac{c}{4\pi e}\frac{\partial}{\partial x}\left(\frac{1}{n}\right)B\frac{\partial B}{\partial z} + \frac{c^2}{4\pi\sigma}\frac{\partial^2 B}{\partial z^2}. \qquad (2)$$

In a two-dimensional case, when ***gradn*** along the flux of electrons exists, equation (2) (so-called Burger's equation) has a nontrivial analytical solution. The most general characteristic function for the 1-D Burgers equation when analyticity is imposed. It indicates that a planar disturbance will be propagated outward at the characteristic speed for the medium, as expected. We can have a single shock front moving in either direction, dual shocks moving in opposite directions, a permanent pressure change propagating in either or both directions, or a derivative soliton moving in either or both directions. While these are all possibilities in a real medium, we can see that the Burgers equation overstates the amplitude in a shock situation. The magnetic field wave generates a steep front and converts into a shock wave

$$B = B_y(z - V_H t), \qquad (3)$$

with the front width ${c^2}\big/{4\pi\sigma V_H}$, where

$$V_H = \frac{cB}{8\pi eL}. \qquad (4)$$

The shock wave also exists in a weekly collisional plasma; the thickness of its front is determined by scale size c/ω_{pe}, while the ohmic dissipation is weak, i.e. behind the wave front $W_E < W_B$.

The magnetic field is "frozen" into the electron fluid, according to equation (1). In the traditional MHD, we assume that the electron and the ion velocities are close to each other, and therefore, the relative displacement of these two components (for the characteristic time scale) is small compared to the characteristic spatial scale *L*. In our case, the electron displacement is finite. Electrons transfer the "frozen-in" magnetic flux and the magnetic energy. They preserve the "frozen-in" condition $B/n = const$ along the wave front, moving towards the increasing density *n* in the magnetic field, which increases in time. However, there is no local "frozen-in" law for ions in such a wave, in contrast to a conventional MHD wave.

The magnetic-field energy changes in the bulk of the plasma because of the plasma nonuniformity. It can easily be shown that since the magnetic-field flux has to be conserved, magnetic-field energy has to be dissipated during the magnetic-field penetration into the plasma. It can be shown that half of the energy that is penetrating the plasma is dissipated.

Let us to consider energy densities, mentioned above, as illustrated in Fig.2.

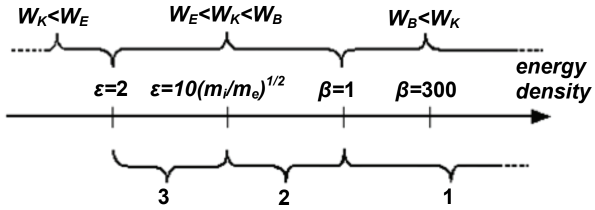

Fig. 2. Classification of plasma flows according to their energy density W_K. Above the axis are the dimensionless variables $\varepsilon = W_K / W_E$, and $\beta_K = W_K / W_B$.

Consider the parameter regime marked '2' in Fig.2. A low energy $(\beta_K < 1)$ plasmoid has only energy enough to expel a fraction of the magnetic field $\Delta B / B < 1$. It can therefore only penetrate through magnetic diffusion combined with self-polarization. The energy budget however requires that $\Delta B / B < 1$ is maintained at all times, also during the transition. The magnetic field has to penetrate the plasma on the same time scale as the transition time. For an abrupt transition in the sense studied here, this requires very efficient magnetic penetration. Such mechanisms have to exist: the laboratory experiments, mentioned in [5] show this for β_K values far below unity. This requirement of fast magnetic diffusion becomes stricter for lower β_K, where there is only enough energy for a small fraction $\Delta B / B$ to be expelled.

When we discussed collisional diffusion, the following scaling exists:

- collisionality is low. Plasma is pushed by magnetic field with Alfven velocity $V_A = B\big/\sqrt{4\pi m_i n}$;
- collisionality is high. The main process is classical diffusion – magnetic field penetration into plasma with velocity $V_D = c^2 / 4\pi\sigma\Delta$, where Δ is characteristic of diffusion length;
- the fast penetration of magnetic field (collisionalless or low collisionality) with velocity V_H, see equation (4).

At this case *L* is only geometrical characteristics of dencity gradient. But also it can be a curvature radius of magnetic field. We can introduce the magnetic Rainold's number $R_M = L / c / \omega_{pi}$. If $(R_M << 1)$ then fast penetration is main process.

Conclusions. The single most important feature that must be understood, and the central finding is that the transverse magnetic field component in the magnetic barrier can diffuse into the plasmoid at an anomalously fast rate. For low β_K plasmoids, with $\beta_K \sim 1$, such magnetic diffusion is a requirement. They do not have enough energy to expulse the magnetic field, and can only penetrate a magnetic barrier through fast magnetic field diffusion and self-polarization. For high β_K plasmoids, with $\beta_K \sim 1$, there is the possibility of either magnetic expulsion, or magnetic diffusion combined with self-polarization. An understanding of the anomalous magnetic field diffusion mechanism is therefore a central issue for understanding penetration of both high β_K and low β_K plasmoids. The treatment in this paper focused on the problem of anomalous magnetic field diffusion and magnetic shock wave formation. Future work should include a combination of space, laboratory and simulation studies. The relationship between impulsive penetration and magnetic reconnection can be studied by comparing these results with results from reconnection experiments with colliding magnetized plasmas.

1. *Arad R., Tsigutkin K., Maron Y., etc.* Observation of faster-than-diffusion magnetic field penetration into a plasma // Phys. Plasma. – 2003. – Vol. 10, № 1. – P. 112–125. 2. *Kingsep A.S., Chukbar K. V., and Yan'kov V. V.* Reviews of Plasma Physics / Ed. by B. B. Kadomtsev (Consultants Bureau, New York, 1990). – Vol. 16. 3. *Mullan, Dermott J.* Physics of the Sun: A First Course. – Taylor & Francis, 2009. – 450 p. 4. *Echim M M, Lemaire J.F. and Roth M.* Self-consistent solution for a collisionless plasma slab in motion across a magnetic field // Phys. Plasmas. – 2005. – Vol. 12. – 072904. 5. *Gunell H., Hurtig T., Nilsson H., Koepke M. and Brenning N.,* Simulations of a plasmoid penetrating a magnetic barrier // Plasma Phys. Control. Fusion. – 2008. – Vol. 50. – 074013 (11 pp).

Submitted on 15.06.2011

UDC 537.622.4

V. Koronovskyy, Ph. D., N. Gorchinskii, eng.

INFLUENSE OF HIGH-TEMPERATURE PROCESSING ON MAGNETO-ELECTRIC PROPERTIES OF THE BISMUTH-SUBSTITUTED YTTRIUM IRON GARNET FILMS

The magnetic domains local areas of epitaxial bismuth-substituted yttrium iron garnet films are investigated with using an optical polarimetry method – the electromagneto-optical (EMO) scanning method. We registered the linear and nonlinear on electric field components of EMO effect. The EMO effect value changed essentially at laser scanning of various points of the magnetic domains. High-temperature influense on a film has not led to essential changes of nonlinear EMO components. However, the linear component of EMO effect was observed only in several points of the thermal-influensed sample. Partial temperature removal of mechanical pressure in a film can cause the specified features of effect.

Keywords: magneto-electric effect, electromagneto-optical effect, electric field, magnetic field.

Окремі ділянки магнітних доменів епітаксійних плівок вісмут-заміщених залізо-ітрієвих гранатів досліджувались із застосуванням методу оптичної поляриметрії – електромагнітооптичний (ЕМО) скануючий метод. Нами зареєстровані лінійна та нелінійна за електричним полем компоненти ЕМО ефекту. Величина ЕМО ефекту суттєво змінювалась при лазерному скануванні різних ділянок магнітних доменів. Високотемпературний вплив на плівку не призвів до значних змін величини не лінійної ЕМО компоненти. Однак, лінійна компонента ЕМО ефекту спостерігалась лише на декількох ділянках термічно обробленого зразка. Часткове термічно-стимульоване зняття механічних напружень в плівці може бути причиною вказаних особливостей ефекту.

Ключові слова: магніто-електричний ефект, електромагнітооптичний ефект, електричне поле, магнітне поле.

Introdustion. Bismuth-substituted ferrite garnets are well known to have a giant magnetooptical response and experimental and theoretical research of garnets has a long history [10]. They have found a widespread use as optical switchers and spatial light modulators. The iron garnet can be used as an optical isolator in the near infrared because of its nearly zero absorption from [7]. In spite of their successful applications, relatively few studies have been directed towards the understanding of the magneto-electric properties of bismuth-substituted ferrite garnets themselves. Behavior and optimization of the Faraday rotation changes in electric fields for bismuth-substituted ferrite garnet films is of a particular interest [3].

Substitution of part of the $Y3^{+}$ on dodecahedral sites by the diamagnetic Bi^{3+} has been found to increase the Curie temperature and it also strongly enhance the magneto-optical properties of yttrium iron garnets (YIG). For this reason bismuth-substituted yttrium iron garnets have had an important impact in the area of magneto-optic materials [9].

The sensitivity of the magneto-optical response of bismuth-substituted yttrium iron garnets to an external field is one of the main properties of interest for imaging applications. Critical to understanding the magnetic properties of bismuth-substituted garnets is the ability to observe and measure magnetic domain structure and separate magnetic domains. The magneto-optic method allows us to follow the kinetics of formation, motion, and annihilation of these domains.

After founding by O'Dell of the magneto-electric (ME) effect (MEE) in single crystals of YIG ($Y_3Fe_5O_{12}$) [6] the active researches of ME properties of this material have begun.

One of the experimental methods for ME properties investigations is a laser polarimetry method. In this case we are registering the effect of light polarization plane rotation in crystal induced by the electric field. This effect was determined as the electromagneto-optical (EMO) effect (EMOE) [5]. A numerous researches of EMOE in YIG have been carried out to make it a potential candidate for some devices (for modulation of amplitudes, polarizations of optical waves).

In our earlier investigations we also used EMO method for investigation of MEE in garnet films [1,2,3]. In this paper we inform about results of the further researches of the EMOE in separate magnetic domains of the bismuth-substituted YIG films. Besides, we also carried out researches of the effect of thermal influence on ME characteristics of the bismuth-substituted ferrite garnet film.

Experiment. A combination of optical polarimetry and a polarising microscope was used as our experimental technics [1]. This technics allows us to measure a local values of the changes of light polarization plane rotation (Faraday rotation) under action of variable electric field applied to the sample. This rotation, as the α_{EMO} parameter, was measured from separate sites of the magnetic domains of the film. For that we used a round scanning diaphragm with aperture size of about 0.3 mm in diameter. The diaphragm allowed us to allocate the film sites of about 4 µm in diameter. Our polarimeter allows us to carry out measurements of linear and nonlinear components of the EMOE. The linear component registered on the basic frequency of an electric field and nonlinear component registered on the double frequency (square law on electric field component of EMOE).

A bismuth-substituted yttrium iron garnet film grown by liquid phase epitaxy on 0.6 mm thick gadolinium gallium garnet substrate was investigated by us. Thickness of the film was 12 µm range. The domain magnetisation of the film was normal to the film plane. A variable voltage, with a frequency $\omega = 1000\,\mathrm{Hz}$ and a static magnetic field could be applied to the film. The investigated film was placed between the optically transparent electrodes. Experiments were carried out at room temperature in longitudinal geometry (**E**|| **k**, **H** || **k**, where **k** is a light wave vector, **H** is a static magnetic field, **E** is an electric field). A He-Ne laser (λ = 0.63 µm) was used in our experiments. Thermal influence on the sample (the second part of our experiments) was carried out at temperature T = 953 K throughout 300 minutes with the subsequent slow cooling of the sumple.

Results and Discussion. Our experimental setup, which is added by a polarising microscope with a scanning diaphragm, can allocate on the sample small sites in diameter about 4 µm. Thus it allows us to spend measurements of EMOE on various sites of the separate magnetic domain. We also have possibility to carry out simultaneously measurements of the square law on the electric field component of EMOE ($\alpha^{2\omega}$) and the linear component (α^{ω}).

In Fig. 1 one series of the received dependences of the EMOE value from positions of scanning diaphragm (X) in the central areas of separate magnetic domain is presented.

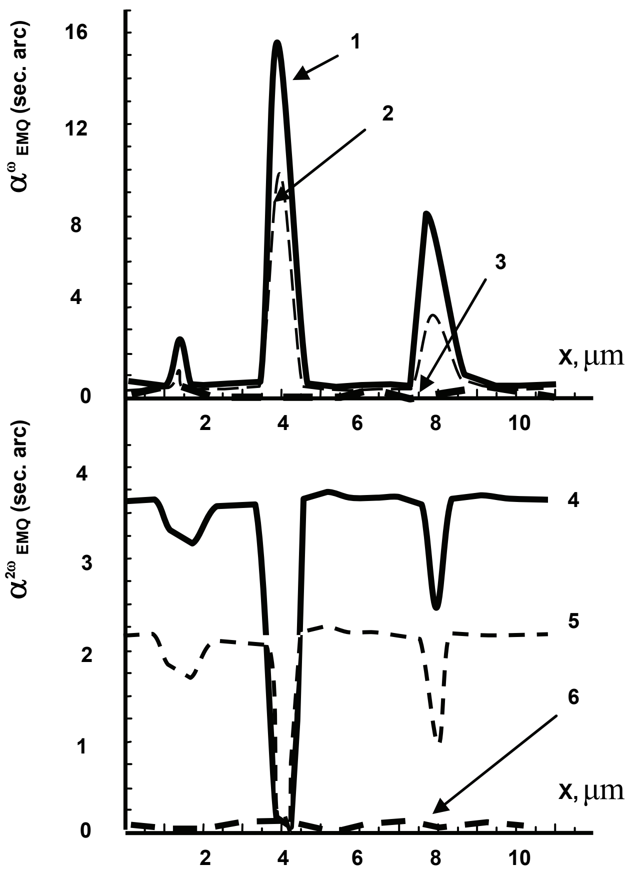

Fig. 1. Dependences of the linear (1,2,3) and nonlinear (4,5,6) components of EMOE from positions of scanning diaphragm

Measurements were spent at: 1 and 4 curves – $H = 0\mathrm{Oe}$, $E = 3\mathrm{kV/cm}$; 2 and 5 – $H = 0\mathrm{Oe}$, $E = 2.2\mathrm{kV/cm}$; 3 and 6 – $H = 280\mathrm{Oe}$, $E = 3\mathrm{kV/cm}$. We moved of a scanning diaphragm in longitudinal direction in relation to positions of domain walls. We can see from the presented curves that a linear (α^{ω}) and not linear ($\alpha^{2\omega}$) components of the electric-field-induced changes of the Faraday rotation were supervised simultaneously. From presented curves we see, that the EMO signal in some points of optical scanning differs essentially from a signal average level. It is necessary to note, that linear component of EMOE appears only in those areas of scanning in which falling of a nonlinear component of effect is observed. EMO effect measurements in others, any way chosen domains, have shown similar results. Differences were observed only in density, localisation and width of a signal change peaks.

We have carried out the experiment, which results are presented in a Fig. 1, once again on the given sample, but the investigated sample has undergone to thermal processing. Thermal influence on the sample was carried out at temperature $T = 953\,\mathrm{K}$ throughout 300 minutes with the subsequent slow cooling.

In Fig. 2 one series of the received dependences of the EMOE from positions of scanning diaphragm (X) in the central areas of separate magnetic domain (the investigated domain got out arbitrarily) is presented. EMO signal registered on the basic frequency of variable electric field (curves 1, 2) and on the double frequency of electric field (curves 3, 4). Measurements were carried out at following values of magnetic and electric fields: 1 and 3 curves – $H = 0\mathrm{Oe}$, $E = 3\mathrm{kV/cm}$; 2 and 4 curves – $H = 280\mathrm{Oe}$, $E = 3\mathrm{kV/cm}$.

We also did optical EMO scanning when sample was in a mono-domain condition which has been preliminary created by a magnetic field ($H = 280\mathrm{Oe}$). At these measurements we did not manage to register EMO signal essential on value. The specified results are presented on Fig. 1 and Fig. 2. As we can see from the presented curves (a curves 3, 6 on Fig. 1, and a curves 2, 4 on Fig. 2), it is not revealed the film areas in which it would be possible to register changes of the EMOE (linear and nonlinear components) – EMO effect in all points remained about zero value.

Presented in Fig.1 experimental results, in our opinion, have a following explanation. On the separate magnetic domains, as on the areas with homogeneous magnetisation, the EMO effect of invariable value can be registered [1]. But, as we can see from Fig. 1, stability of the EMO signal in different areas (or points) of the domain is broken. We have registered occurrence and radical increase of the linear component of EMOE in some separate areas of the investigated magnetic domain. Simultaneously with it we registered drastic decrease of square law on the electric field component of EMO signal in the same points of the investigated domain. Such decrease of square law on the electric field component of EMOE are probably can be connected to the changes of the local value of demagnetizing fields in the small scanning areas. This component of Faraday rotation is modulated by the variable electric field in our experiments. We are shown earlier [1] that EMO parametre, at invariable magnetisation depends on the value of demagnetization fields in vicinities of a point of optical probing. A magnetization, which mainly defines the light polarization plane rotations, does not change under the electric-field action in YIG films.

Thus, the registered features in displays of square law on the electric field component of EMOE can be in the film areas with not uniform magnetisation. These are the areas with changeable local values of a demagnetization fields. Defects on a surface or in film volume can be such areas. Defect breaks a continuous condition of material and the local magnetisation difference is formed on it. The magnetisation directions in vicinity of defects can essentially differ from crystallo-graphic directions of easy magnetisation for considered material.

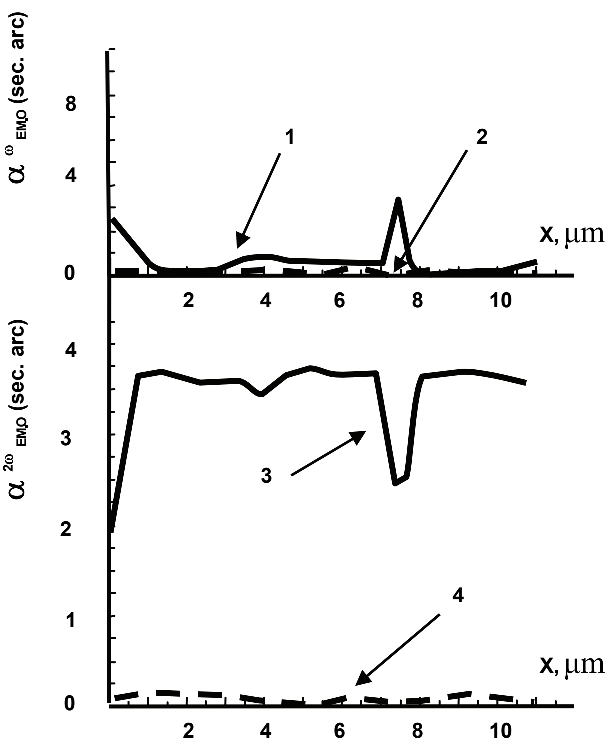

Fig. 2. Dependences of the linear (1,2) and nonlinear (3,4) components of EMOE from positions of scanning diaphragm after temperature influense

Such our assumptions confirm also the results of experiments presented in a Fig. 2. We carried out experiment similar to previous (see Fig. 1). In Fig. 2 four of the received dependences of EMOE from positions (X) of scanning diaphragm in the central areas of any way chosen separate magnetic domain are presented. From the Fig. 2 we can see that after temperature influence on the investigated sample ($T = 953\,K$ throughout 300 minutes with the subsequent slow cooling) displays of the linear component of EMOE has essentially decreased. It is possible to see also that instability of a square law on the electric field component of EMO signal is observed, but not so clearas as before temperature influence.

When we discuss display of a linear effect component, is necessary to take into account some of the features of epitaxial ferrite garnet films structure in comparison with single crystals of this material. In particular, due to the conditions at which there is an origin and formation of garnet film, macro-, micropressure and deformations arise in them. Significant mechanical pressure can be accumulated in films during the growth because of the mismatch of parameters of crystal lattices of a film and a substrate or because of rather large cooling rates of films. The process of film growth can be accompanied by formation of crystal lattice defects due to the large supercoolings and supersaturation. The epitaxial film layer has nonuniform pressures, i.e. the film lattice constant differs from the substrate lattice constant and there are existing surface transitive layers on substrate/film and film/air. Chemical compound of transitive layers differ from chemical compound of the central area of a film. On the thickness of garnet film there are two areas: the basic undistorted (a thin layer of a film with centrosymmetrical structure, characteristic for single crystals) and area where the structure is no longer centrosymmetrical. It is known, the MEE that are linearly dependent on the electric field are forbidden for the centrosymmetric cubic crystal structure of garnets [8]. Only square-law on the electric field MEE can be observed in single crystals of YIG and bismuth-substituted ferrite garnets. But EMO signal occurrence on the basic frequency of electric field in our experiments (see Fig. 1 – a curves 1, 2, 3, and Fig. 2 – a curves 1, 2) allows us to assume that at least some of the investigate film's areas have non-centrosymmetric structure. That is, in this case of the strained garnet film we can hope also for the occurrence of the effects, caused by changing (lowering) of symmetry of lattice. In our case, it is effect of occurrence of a linear component of EMOE in separate areas (or points) of the investigated bismuth-substituted ferrite garnets film. Apparently from a Fig. 1, in these points also sharply decreases square law on the electric field component of EMO signal and under our assumption it is local areas of mechanical deformation or separate points of defects. Decrease or disappearance of linear EMOE after temperature influence, is possibly connected with partial removal of the specified pressure by long thermal influence. Possible relaxation of interfacial strain for the film surface and interface regions after temperature influence was registered also at measurements of the EMOE from multidomain areas of garnet films [4].

Conclusions. Thus, in our experiments when probing by optical beam various sites of separate magnetic domain of the bismuth-substituted yttrium iron garnet film and using EMO method, we registered the nonlinear (square law on the electric field) and linear components of EMOE. Local areas or separate points on a surface or in film volume where sharp changes of EMO signal were registered, under our assumption can be areas of strain or local points of defects of the sample. Long high-thermal influence on the garnet film has led to changes of electromagneto-optical dependences and in character of EMO effect.

1. *Koronovskyy V.E., Ryabchenko S.M., and Kovalenko V.F.* Electromagneto-optical effects on local areas of a ferrite-garnet film // Phys. Rev. B. – 2005. – Vol. 71. – P. 172402–172406. 2. *Koronovskyy V.E.* Influence of an external mechanical strain on the character of the magnetoelectric effect in epitaxial films of yttrium iron garnet // Phys. Stat. Sol. (a). – 2006. – Vol. 203, №. 8. – P. 2007–2011. 3. *Koronovskyy V.E.* Influence of powerful laser irradiation on electromagneto-optical dependences of yttrium iron garnets // J.Appl.Phys. – 2009. – Vol. 106. – P. 063914–063916. 4. *Koronovskyy V.E., Gorchinski N.D.* The electromagnito-optical effect in local areas of single magnetic domains in epitaxial films of yttrium iron garnet // Functional Materials. – 2011. – Vol. 18, №1. – P. 37–41. 5. *Krichevtsov B.B., Pisarev R.V., Selitskij A.G.* The electromagneto-optical effect in yttrium iron garnets $Y_3Fe_5O_{12}$ // JETP Lett. – 1985. – Vol. 41. – P. 317–319. 6. *O'Dell T.H.* The electrodynamics of magnetoelectric media. – Philos. Mag., 1967. 7. *Scott G.B., Lacklison D.E., and Page J.L.* Absorption spectra of Y3Fe5O12(YIG) and Y3Ga5O12:F3+ // Phys. Rev. B. – 1974. – Vol. 10. – P. 971–974. 8. *Velleaud G., Sangare B., Mercier M., and Aubert G.* Magnetoelectric properties of Yttrium Iron Garnet // Solid State Commun. – 1984. – Vol. 52. – P. 71–74. 9. *Wemple S.H., Blank S.L., Seman J.A., and Biolsi W.A.* Optical properties of epitaxial Iron garnet thin films // Phys. Rev. B. – 1974. – Vol. 9. – P. 2134–2137. 10. *Zvezdin A.K., Kotov V.A.* Modern Magnetooptics and Magnetooptical Materials: Institute of Physics Pub. – Taylor & Francis, 1997.

Submitted on 16.05.2011

UDC 004.(55+58+633)

A. Kotenko, stud., V. Bilonenko, eng., V. Gryaznova, Ph. D., Yu. Boyko, Ph. D., A. Bey, stud.

DEVELOPMENT AND IMPLEMENTATION OF THE LEARNING MANAGEMENT SYSTEM WITH SOCIAL COMPONENT: GROUPS.UNIV.KIEV.UA

Existing approach to the development of learning management systems is studied and analyzed. Alternative approach based on principle of self-organization of users' activity is suggested. A new learning management system is designed in the framework of this alternative approach and implemented on base of web-technologies. The purpose of development of this system is to complement the traditional structure and learning potential of the university by means of social learning tools.
Keywords: learning management system, self-organization of users, social learning, version control system.

Розглянуто та проаналізовано існуючий підхід до створення систем автоматизації навчального процесу. Запропоновано альтернативний підхід, що базується на принципі самостійної організації власної діяльності користувачами. В рамках цього підходу розроблено нову систему автоматизації навчального процесу та реалізовано її на основі веб-технологій. Мета розробки цієї системи – не дублюючи традиційну структуру та можливості навчального закладу, доповнити їх засобами для самостійної діяльності.
Ключові слова: система автоматизації навчального процесу, самоорганізація користувачів, самостійна робота студентів, система контролю версій.

Introduction. Rapid development of informational technologies (IT) nowadays became the reason of wide usage of different learning management systems (LMS) and educational software at universities. The purposes of implementation of such systems include, in particular:

● creating, editing, saving and disseminating electronic textbooks and other educational materials;

● testing knowledge level of students;

● logging educational results of students, teaching load of staff and other administrative information.

Popular learning management systems (f.g., Moodle or ILIAS) are based on rather determined behavioral models with built-in administrative impact. It is natural for the systems directly modeling educational process, which is formalized by itself. But this approach lacks flexibility and restricts users' behavior to formal situations of teacher-student interaction.

Nevertheless, the educational process does not come to only formal interaction. As it is mentioned in [1], one of the strongest determinants of students' success in higher education is their ability to form or participate in small study groups. In our reality, this type of students' interaction appears during their unsupervised work or during the work in non-administratively formed (f. g., scientific) groups.

One more imperfection of popular LMS is inefficiency of their usage as knowledge bases. It is induced by limitation of users who can fill knowledge base with materials only to teachers and therefore potential lessening the knowledge base scope. In addition, as a rule of users' interaction within popular LMS, students' access to educational resources is regulated and a student can reach only the resources concerning current courses.

Therefore, as existing popular LMS's are designed according to the model of a traditional university and reflect advantages and limitations of this model, there exists the need to build the new LMS based on different principles, namely, self-organization of students' and teachers' activity, that can create new opportunities for learning and working. Functionality and composition of this new system also have to be designed for maintenance of students' self-studying as a constituent of the university learning process.

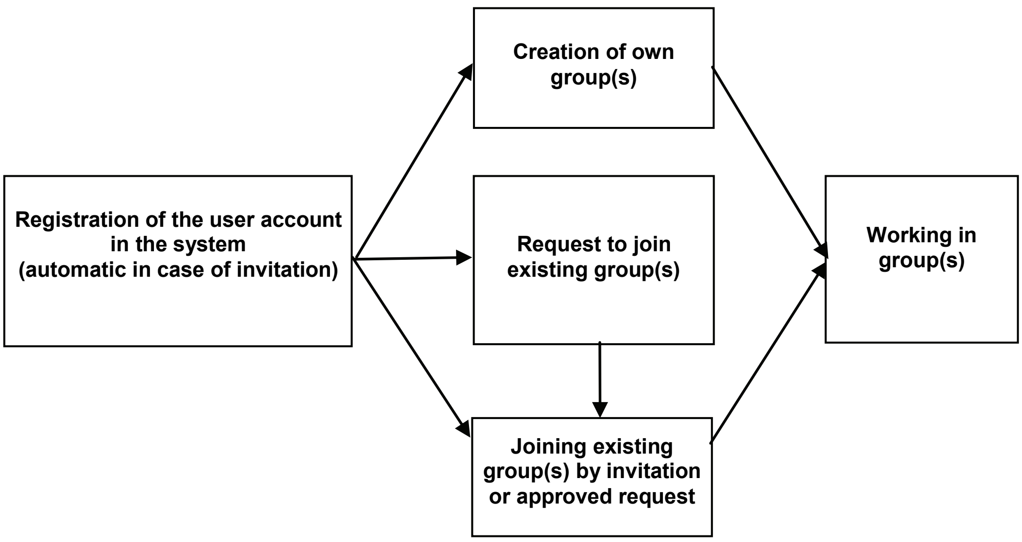

Fig. 1. Stages of user's usage the Groups LMS

Development and discussion. The LMS named Groups was designed in Kyiv National Taras Shevchenko University to satisfy all the above-listed requirements. The Groups LMS is implemented as a part of the computer network of the University and can be reached at http://groups.univ.kiev.ua.

The Groups LMS uses the same base element of users' structuring as other LMS's, namely, "groups", but the mode of a group activity is different. Traditionally, a group is a model of a university structure element and can be used in accordance with this fact. In the Groups LMS, a group reflects by default an informal community of users and, therefore, has not built-in policy.

The groups in the Groups LMS can be open and closed, official and unofficial. Openness or closedness of the group defines accessibility of the group data for the users of the system, who are not members of this particular group. An official group reflects one of existing structure elements of the University and this fact is indicated respectively in the list of all groups.

Every group in the Groups LMS consists of users and administrators. The administrator of the group can change group properties and users list. One more difference of the Groups LMS from traditional LMS's lies in the fact that there is no need to be a lecturer or other university official for being the group administrator.

For using the Groups LMS (Fig.1) one needs to:

- register at the system website http://groups.univ.kiev.ua;
- create one or several new groups AND/OR join one or several existing groups.

As compared with other systems, such an approach requires additional user activity, which is caused by the freedom to choose at the moments of joining or creating a group. At the same time, traditional LMS's determine group membership of the LMS user on the base of membership of the corresponding person of the university structure element.

From the moment of being registered as a group member, the user of the Groups LMS can invite other users or even external persons to this group. In case of accordance of an external person to such an invitation, a new user account in the Groups LMS is created automatically.

The user who created a group acquires a right to administer this group. This user can also delegate authority to administrate this group to other members of the group.

Also any registered user of the Groups LMS can send a request for joining some group to the group administrators, who can approve or reject it.

The above-mentioned mechanisms provide possibilities for joining the users into the groups, but do not impose superfluous constraints on this process. Instead of built-in tight regulations, group administrators, who establish interaction rules in the group and keep their fulfillment under control, implement necessary management of the group activity.

Existing popular LMS's use sets of parametrized rules of possible users' interaction that are defined at the moment of the system creation. Afterwards, authorized users can change these parameters to some extent for highest possible match with specific needs.

As contrasted to other LMS's, in the Groups LMS group users' agreement is vitally important factor of the group management. Such an approach makes the system more flexible and enhances possibilities of the users' self-organization, as they are able to work out rules of communication that could not be provided at the time of the system designing. One more advantage of the Groups LMS is the way of working out such rules: they are just a result of natural human communication, which means that there is no any special qualification demand for the system users, as well as there is no need for users to have access to the source code of the system.

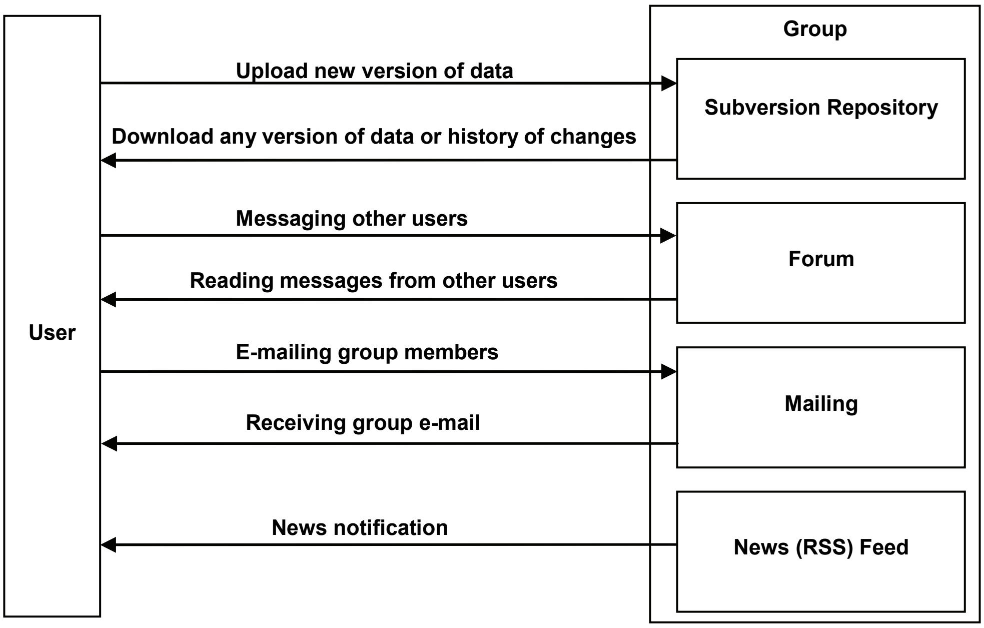

Fig. 2. User tools in the Groups LMS

A user of some group in the Groups LMS has following working tools (Fig.2):

- user account management mechanism;
- group forum;
- group mailing;
- group file repository;
- web interface of the repository.

The Groups LMS also allows user to monitor events in all the groups he/she belongs to and to manage group properties in case of appropriate access level.

One of the most prominent features of the Groups LMS is a Subversion repository, which makes possible for different users to modify and manage the same set of data from their respective locations and thereby encourage collaboration [2].

Subversion repository is used for storing, distributing and exchanging files of different nature (mostly learning aids, but not limited to them). It can be used as an important tool for the self-learning process of a group of students. As repository implementation uses version control system, which is standard de-facto in software engineering, repository can be also successfully used for group software development.

As opposed to other LMS's that also offer file storage and exchange tools, the Groups LMS does not impose constraints on data format. A user can access the repository through web interface or special client software.

Group mailing serves for e-mail messaging from a group user to all the members of this particular group.

Presence of a similar feature is a standard for other LMS's also.

Group forum is meant for discussion on assigned tasks, ways of problem solving and other topics. A user can also place links to repository files or images for illustration and/or better understanding of the issue. Other LMS's also have similar feature, but some authority, not by group members themselves, usually moderates their forums as it takes place in the Groups LMS.

Implementation and usage. Implementation of the Groups LMS was performed by web technologies. Such a decision makes the system more universal, as there is no need to create different versions for supporting different software or hardware platforms. A user interacts with the system through a web-browser, anyone of which already has implementations for almost all the platforms. The other advantage of this approach is that information is delivered to the user through network, thus, it is always possible to have the up-to-date version of news feed or files.

Realization of the approach described above was done with open-source components. The reason for such a choice is work experience and proven dependability of these components in other projects of Information and Computing Center of National Taras Shevchenko University of Kyiv, that is the base for the Groups LMS development also. The other advantage of using open-source components is possibility to research and change all parts of the source code of the system that may be useful for system adaptation for some specific needs.

The main part of the system functionality is implemented using PHP programming language. Architectural pattern used for creation the system is Model-View-Controller (MVC) that was first described by T. Reenskaug [3] and is widely used in web-development nowadays. According to the MVC pattern, there are three types of the system components: object model, user interface and controller joining them into holistic system. So, the logic of object operation and the user interface are separated and can be developed independently.

In the Groups LMS development process, the three parts of classical MVC approach were implemented as separate modules in the framework of common environment that provides interaction between these modules. The feature of this environment is possibility of generating webpage using components defined by different modules of the system.

The main scenarios of using the Groups LMS are interaction of the lecturer with academic group of students, interaction of a scientific group members and collaboration in self-education or software development.

An academic group is to some extent closed system and interaction pattern of the academic group member with external persons or objects is often defined by the fact that he/she is a member of particular academic group. It means, for example, that a lecturer rather frequently interacts with the group as a whole, not with individual students. That is why classic LMS approach to conception of a group associating it with academic group of students was considered worth implementation also in the Groups LMS. It grants the following opportunities:

- students can exchange different information, as homework tasks, learning aids and so on;
- a lecturer can place recommended learning aids for students, as well as tasks for homework or labs in group repository. The latter is very useful for the students of technical specialties, as their tasks have to be done very often with help of computers. If tasks already are in electronic form, then the process of carrying information to paper and back becomes unnecessary. The same situation takes place at handing in students' work to lecturer;
- active information exchange between students or lecturer and students results in accumulation of teaching materials in the group repository and comments to them in the group forum. Therefore, in the course of time the group turns into knowledge base on particular subject.

Scientific work also can be facilitated to some extent with help of the Groups LMS. The system provides ability of interaction and information exchange between student and his/her scientific adviser, between group of students from different academic groups and/or students of different academic years.

A scientific adviser can use the system for provision necessary scientific literature or links to it to a student. Also a scientific adviser and a student can use communication features of the Groups LMS in case of difficulties in face-to-face meeting for some reason (f. g., academic trip of the scientific adviser).

The group of students rather often works on the same or related research issues. In such a case there appears requirement of coordination of activity and/or information exchange. Also it may be convenient for a scientific adviser of such a group of students to communicate with all the members of this group at the same time.

Similar but nevertheless different case is when students of different academic years do research on different aspects of the same or related scientific problems. In this case students that just started their research need the materials already used by their predecessors. Also, by reason of common research area successors may need results obtained by their predecessors. The features of the Groups LMS (repository, in the first place) allow solution of all these problems.

Nowadays, computers are widely used in scientific researches, for example, in automatization of experiment or implementation of numerical computing. That is why, need for realization of some specific algorithms arises continually.

In connection with this necessity, the Groups LMS takes advantage of making available for the system users the open-source version control system Subversion [2] which is widely exploited in professional software development. The version control tools are most useful for collaboration of the software developers group, but it is very convenient for individual work also.

Conclusions. Development of a learning management system directly modeling the formal interaction scheme of an university results in inheritance of limitations of the last, namely, lack of attention to social learning.

That is why, another approach for creating an LMS, compensating this deficiency, was suggested. This approach is based on the idea of self-organization of activity of the LMS users.

The Groups LMS (http://groups.univ.kiev.ua) was developed and implemented in the framework of this approach taking into account potentialities of social learning.

The version control system Subversion proposed for usage in the Groups LMS considerably expands potential of its application for cooperative data processing, storage and accumulation of learning and/or scientific materials and as software development tool.

1. *Brown J.S., Adler R.P.* Minds on Fire: Open Education, the Long Tail, and Learning 2.0 // EDUCAUSE Review – 2008 – Vol. 43, № 1. 2. *Collins-Sussman B., Fitzpatrick B.W., Pilato C.M.* Version Control with Subversion – O'Reilly Media, 2004. 3. *Reenskaug T.M.H.* MVC–XEROX PARC 1978-79 – http://heim.ifi.uio.no/~trygver/themes/mvc/mvc-index.html.

Submitted on 25.05.2011

UDC 533.9:51-73

O. Kravchenko, Ph. D., T. Lisitchenko, head Sci. Sec., G. Levada, eng.

DOUBLE LAYERS IN LOW PRESURE DC-DISCHARGES WITH DUST PARTICLES

Direct current (dc) discharge in argon with dust particles is studied by computer simulation. PIC/MCC method is used to describe electron and ion plasma components. Dust particles were distributed uniformly in space in our model and were supposed immobile. The results show that dust particles may be responsible for the formation of double layers in the discharge. The layered structures in the discharge is formed in this case, which causes heating of the electrons. The influence of dust density and neutral gas pressure in the discharge chamber is investigated on the structure of the discharge.

Keywords: dust particles, dc-discharge, computer simulation.

За допомогою комп'ютерного моделювання досліджується розряд постійного струму в аргоні з пиловими частинками. Для описання електронної та іонної компонент плазми використовується PIC/MCC метод. Пилові частинки в нашій моделі розподілялись однорідно в просторі і були нерухомими. Результати показують, що пилові частинки можуть спричиняти утворення подвійних шарів в розряді. В цьому випадку формуються шаруваті структури в розряді, які призводять до нагрівання електронів. Досліджується вплив концентрації пилу та тиску нейтрального газу в розрядній камері на структуру розряду.

Ключові слова: запорошена плазма, розряд постійного струму, комп'ютерне моделювання.

Introduction. Dust plasmas are of great interest for technological applications as well as from the point of view of basic physics. For both fields, the influence of microparticles on the plasma is of significant importance. It has been known for a long time that a losses of plasma particles on the surface of the microparticles suspended in a plasma, may be comparable to that on the walls of the setup, resulting in faster decay of the plasmas. Dust particles were observed in different discharges, particularly in low pressure dc discharges [5, 10]. They can appear in discharge plasmas as the product of the plasma-wall interaction and their subsequent penetration into the plasma or be created due to coagulation of various components in chemically active plasmas.

Many interesting phenomena are observed and investigated in dusty plasma, e.g., formation of dusty structures (Coulomb crystals, liquids and gases), phase transitions, vortexes, wave propagation, and different kinetic processes.

These dust particles can essentially influence on plasma properties due to the continuous selective collection of background electrons and ions that can cause an essential change of electrons in low pressure discharges and therefore cause a change of the electron non-elastic process rates. Therefore it is very important for applications to simulate preliminary parameters of these discharges in gases used in plasma processing in the frame of a kinetic treatment.

For the conditions of RF discharge used for thin films preparation in the semiconductor industry, the influence of dust particles on discharge properties was investigated in [2, 3] by PIC/MCC simulations. Recently, the dusty plasma of RF discharge was investigated with the help of Boltzmann equation for EEDF [4]. Different models for reactive dusty plasma of RF discharge were also presented in [6, 7]. It was understood that each dust particle acted as an electron and ion sink, and a large concentration of dust particles would have some effect on the plasma properties and on the plasma sustainment conditions. The electron and ion losses on dust particles should be compensated in ionizing collisions, and an averaged electric field in a discharge should increase in the region containing dust particles.

The main aim of this paper is to study dc glow discharges with dust particles using kinetic model and to describe the influence of dust particles on the discharge parameters in argon in the wide range of dust particle concentrations and radii.

Model. It is considered an one-dimensional direct current (dc) discharge between two plane electrodes separated by the gap of $d = 0.1\,m$ which is filed by Ar at pressure of $p = 0.1 \div 0.5$ Torr. Immobile dust particles of the radius $r_d = 1 \div 10\ \mu m$ are distributed uniformly in the interelectrode gap with the density n_d. The dust particles collect and scatter electrons and ions, distributed in the discharge with density n_e and n_i, respectively.

The PIC/MCC method [1] used for computer simulations of the dc discharge with dust particles. This method is based on a kinetic description of the motion of positive and negative "superparticles" in phase space under an influence of an self-consistent electric field E obtained by solving of Poisson equation. An electrode collects a "superparticle" if its center reaches an electrode surface. The secondary emission is taken into account in the framework of the models of [8].

The Monte Carlo technique [1, 12] is used to describe electron and ion collisions. The collisions include elastic collisions of electrons and ions with atoms, an ionisation and excitation of atoms by electrons, the change exchange between ions and atoms, Coulomb's collisions of electrons and ions with dust particles, as well as the electron and ion collection by dust particles. In addition to a usual PIC/MCC scheme, the weighting procedure is used also for the determination of a dust particle charge with which a superparticle is interacting. The electron-argon collision cross-sections used in the model are the same as those used in [9]. The Coulomb's cross-section for electron and ion scattering by immobile dust particles is taken from [11].

The simulation starts with an initial uniform distribution of electrons and ions with densities equal to $2 \cdot 10^{14} m^{-3}$ and is prolonged in time up to the moment when the change of the discharge parameters is less a given limit.

Results. Spatial distributions of the potential of self-consistent electric field are plotted in fig. 1 at different dust densities n_d, the dust radius $r_d = 10\ \mu m$ and the effective secondary electron emission yield $\gamma = 0.3$. As can be seen in this figure, almost all the voltage drops on the cathode layer in the absence of dust particles (the solid line). In this case, the potential is almost constant in the positive column of the discharge. In discharge with dust particles we can see one (the dash line) or several (the dot line) potential drops in the position column, which are double layers.

The double layers number is increased at the dust density increasing. At that the voltage drop across the cathode layer is decreased, just as a cathode layer thickness.

The reason for the formation of the potential drops lies in the fact that in the presence of dust particles an electric field is appeared in the plasma of the positive column. It is the result of a decreasing of electron and ion densities in the discharge due to their recombination on dust particles. Consequently, electrons are accelerated when moving from the cathode to the anode. In the region where they attain sufficient energy to ionize the gas, substantially increases the ionisation rate and, the concentration of plasma particles. It is show in fig. 2a, where electron density as function of spatial coordinate x is plotted at different dust densities n_d and the dust particle radius $r_d = 10\ \mu m$. We can see that on the edge of cathode layer peaks of electron density are formed, that is caused high rate ionisation in this area. The electron density is defined by balance between a gas ionisation and a recombination on dust particles. Dust particles at $n_d = 10^8\ m^{-3}$ led to an increase in the concentration of electrons at the edge of the cathode layer, but at $n_d = 5\cdot10^{10}\ m^{-3}$ electron density peak are decreased. Spatial distribution of electrons is almost uniform in positive column of the discharge without dust particles. On the contrary, electron density is decreased rapidly in a positive column of the discharge at $n_d = 5\cdot10^{10}\ m^{-3}$ and at some distance from the cathode, electrons almost disappear due to the deposition on dust particles. However, in double layers the plasma density increases again, so that peaks of electron density are formed (fig. 2a).

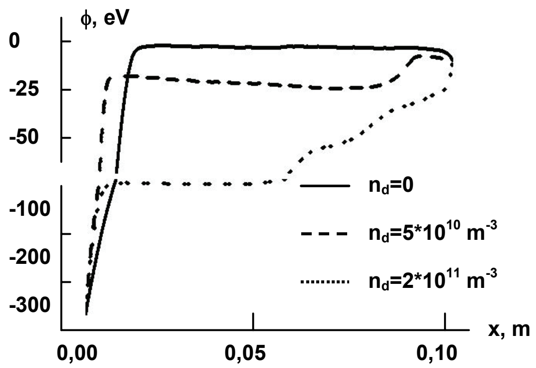

Fig. 1. Spatial distribution of the potential ϕ at different dust densities n_d

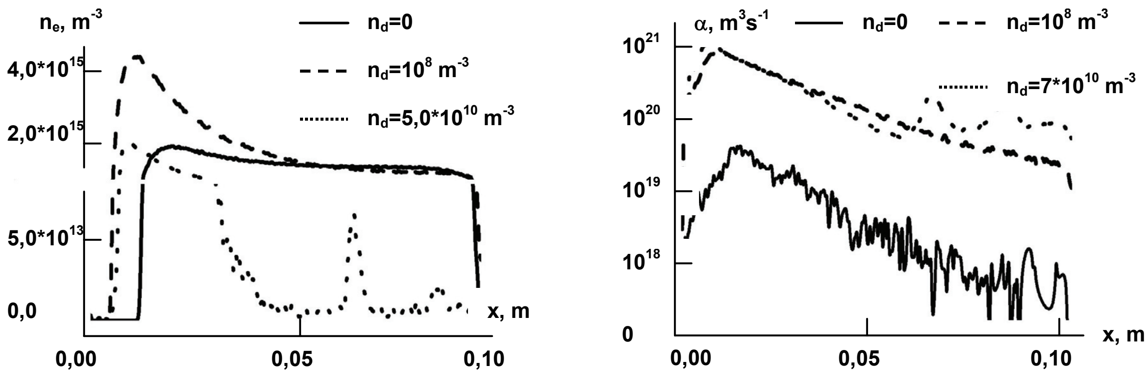

Fig. 2. Spatial distributions of the electron n_e density (a) and spatial distributions of ionization rate (b) at different n_d and $r_d = 10\ \mu m$

Spatial distributions of the ionization rate are show in fig. 2b. It is seen that dust particles in discharge enhance the gas ionization. Moreover, the ionization rate is increased at double layers positions. The cause of that is the electron acceleration by the electric field in double layers. It confirms the fig. 3, where the phase-plane portrait of electrons is represented.

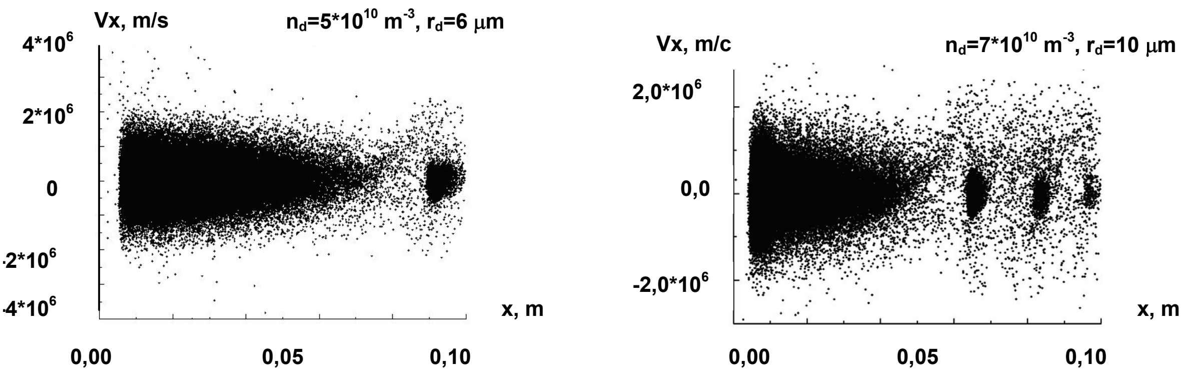

Fig.3. Phase portraits of electrons in dc-discharges for cases $n_d = 5\cdot10^{10}\ m^{-3}$, $r_d = 6\ \mu m$ (a) and $n_d = 7\cdot10^{10}\ m^{-3}$, $r_d = 10\ \mu m$ (b)

One can see the high energy electron flow is formed at the double layer, that causes a heating of electrons and the electron density peak forming in this place. We will notice also, that the stratified structure of the discharge appears at presence of dust particles. The areas of finite motion of low energy electrons appear between double layers. The number of double layers is increased in the discharge at the increasing of dust density and dust particle radius. As can be seen from the fig,3b, the three electron clouds are formed in the discharge at $n_d = 7\cdot 10^{10}\ m^{-3}$, $r_d = 10\ \mu m$.

The acceleration of electrons in double layers and their subsequent scattering by neutrals leads to heating of electrons in the discharge. The fig.4 shows the average kinetic energy of electrons in the discharge for several cases with different density and radius of the dust particles.

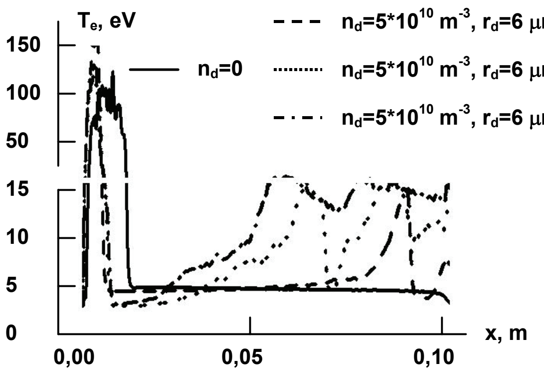

Fig. 4. Spatial distributions of mean electron energy in dc-discharge

It is seen that the electrons in all the cases have high energy at the edge of the cathode layer. Hoverer, the energy of the electrons is much lower in the positive column of discharge without dust particles. The appearance of dust particles in the discharge leads to a significant increase in the energy of the electrons in the positive column.

Conclusion. Obtained results show that the dust particles essentially influence the spatial distribution of the discharge parameters, in particular an increase of a dust particle density causes a decreasing of a sheath width and a cathode jump. At certain dust density if formed a layered structure of the discharge, which causes heating of the electrons. At the dust density increasing multiple double layer can be formed. In area of layers there is an increase of concentration of electrons and ions from the increase of energy of electrons and, accordingly, ionization rate. It is set, that reason of formation of layers is appearance of the electric field in the positive column of discharge with dust particles due to the plasma particles decreasing.

1. *Birdsall C.K.* Particle- in-Cell Charged-Particle Simulations, Plus Monte Carlo Collisions With Neutral Atoms, PIC-MCC // IEEE Trans. Plasma Sci. – 1991. – Vol. 19. – P. 65–85. 2. *Bouchole A., Boufendi L.* Particulate formation and dusty plasma behavior in argon-silane RF discharge // Plasma Sources Sci. Technol. – 1993. – Vol. 2. – P. 204–213. 3. *Chutov Yu.I., Goedheer W.J.* Dusty radiofrequency discharges in argon // IEEE Trans. Plasma Phys. -2003. – Vol. 31. – P. 606. 4. *Denysenko I., Yu M.Y., Xu S.* Effect of plasma nonuniformity on electron energy distribution in a dusty plasma // J. Phys. D: Appl. Phys. – 2005. – Vol. 38. – P. 403–408. *5. Fortov V.E., Khrapak A.G., Khrapak S.A. et al.* Mechanism of dust-acoustic instability in a direct current glow discharge plasma // Physics of Plasmas. – 2000. – Vol. 7. – P. 1374–1380. 6. *Goedheer W.J., Land V., Venema J.* Modelling of Voids in Complex Radio Frequency Plasmas // Contributions to plasma physics. – 2009. – Vol. 49. – P. 199–214. 7. *Schweigert I.V., Schweigert V.A.* Combined PIC–MCC approach for fast simulation of a radio frequency discharge at a low gas pressure // Plasma Sources Sci. Technol. – 2004. – Vol. 13. – P. 315. 8. *Surendra M., Graves D.B., Jellum G.M.* Self-consistent model of a direct-current glow discharge: Treatment of fast electrons // Phys. Rev. A. – 1990. – Vol. 41, № 2. – P. 1112–1126. 9. *Surendra M., Graves D.B.* Particle simulations of radiofrequency glow discharges // IEEE Trans. On Plasma Sci. – 1991. – Vol. 19, № 2. – P. 144–156. 10. *Thomas E.* Observations of high speed particle streams in dc glow discharge dusty plasmas // Physics of Plasmas. – 2001. – Vol. 8. – P. 329–333. 11. *Trubnikov B.A.* Problems of plasma theory. – M.: Gosatomizdat, 1963. 12. *Vahedi V., Dipeso G., Birdsall C.K. et al.* Capacitive RF discharges modeled by particle-in-cell Monte Carlo simulation. I. analysis of numerical techniques // Plasma Sources Sci. Technol. – 1993. – Vol. 2. – P. 261–272.

Submitted on 07.06.2011

UDC 537.523

O. Nedybaliuk, post grad. stud., V. Chernyak, Dr. Sci., S. Olszewski, Ph. D., E. Martysh, Dr. Sci., T. Lisitchenko, head Sci. Sec.

AIR FLOW DIRECTION EFFECT ON THE PARAMETERS OF PLASMA OF DIELECTRIC BARRIER DISCHARGE

Parameters of dielectric barrier discharge plasma at atmospheric pressure as dependence from value and direction of air flow relative to current-lines were investigated. Emission spectra of dielectric barrier discharge plasma in the range of wavelengths 200-1000 nm were analyzed. Excitation temperatures (rotational T_r^*, vibrational T_v^* and electronic T_e^*) were calculated.

Key words: plasma, dielectric barrier discharge, emission spectrum, flow.

Досліджено параметри плазми діелектричного бар'єрного розряду атмосферного тиску в залежності від напрямку потоку повітря відносно ліній струму. Проаналізовано емісійні спектри плазми діелектричного бар'єрного розряду в діапазоні довжин хвиль 200-1000 нм. Обраховано температури заселення збуджених рівнів (обертальних T_r^*, коливальних T_v^* та електронних T_e^*).

Ключові слова: плазма, діелектричний бар'єрний розряд, емісійний спектр, потік.

Introduction. Dielectric barrier discharge (DBD) is widely used in various technological systems and devices, including chemical reactors, disinfection systems, ozone generators, plasma displays, pressure sensors, etc. Processes like pollution control and surface treatment with DBD show great promise for the future. The most important characteristic of DBD is that non-equilibrium plasma conditions can be provided at high pressure, for example, atmospheric one. In DBD this can be achieved in a much simpler way than with other alternative techniques like low pressure discharges, fast pulsed high pressure discharges or electron beam injection. The flexibility of DBD configurations with respect to geometrical shape, operating medium and operating parameters is remarkable. In many cases discharge conditions optimized in small laboratory experiments can be scaled up to large industrials installations. Efficient low cost power supplies are available up to very high power levels.

Numerous experimental investigations performed in the past decade showed that DBD-based devices called actuators can also be used in the systems of gas flow control [1].

This work presents the results of an experimental investigation of air flow direction effect to current-lines on the parameters of dielectric barrier discharge plasma.

Experimental setup. Scheme of experimental setup of DBD are shown on Fig. 1. The voltage was supplied between the two electrodes made from aluminum foil (thickness by 0.1 mm) with the help of the power source (4). Upper (1) and lower electrodes (2) were separated by dielectric (3). Upper electrode (1) is on the surface of commercial glass plate (3) which contacts with air. Lower electrode (2) is between two plates from commercial glass (3) by the sizes of 50 x 50 x 2.5 mm. Both electrodes consist of six rectangular strips the sizes of 35 x 1.5 x 0.1 mm connected between itself. The strips of upper and lower electrodes alternate forming the matrix 30 x 30 mm. The distance between the strips of upper and lower electrodes (top view) was 1 mm.

The emission spectroscopy was used for plasma diagnostics. Emission spectra were measured with system that was made up of spectrum device S-150-2-3648 USB (5) and light guide (6). Input cut of the light guide was in the distance 30 mm from the plane of upper electrode (1) and was oriented to the center of matrix (30 x 30 mm), which is formed by electrodes. The spectrometer worked in range 200 – 1200 nm with resolution 0.6 nm.

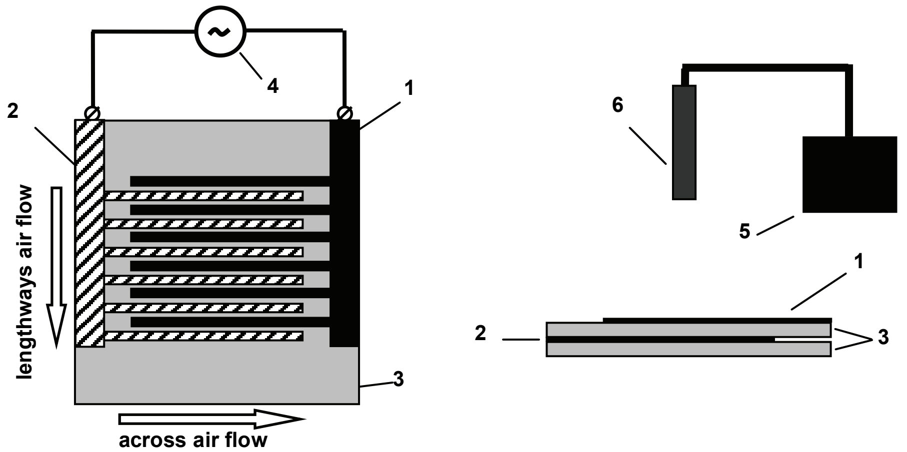

Fig. 1. Scheme of experimental setup DBD

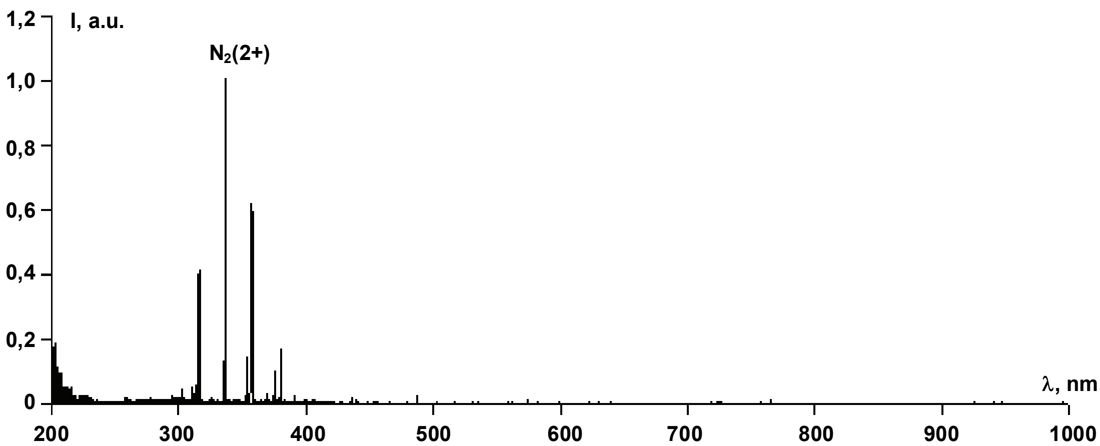

Fig. 2. Typical emission spectra of DBD-plasma in air

Results and Discussion. The time-averaged typical emission spectrum of dielectric barrier discharge plasma in atmospheric air is shown on Fig. 2. Bands of second positive system of nitrogen molecule $N_2(2+)$ are presents on this emission spectrum.

The temperatures of vibrational and rotational excited levels population of second positive system of nitrogen molecule $N_2(2+)$ were determined by the procedure [3]. Comparison of emission spectra $N_2(2+)$ measured experimentally and simulated by the program SPECAIR [2], for more accuracy determination of temperatures, were used. Emission spectra of second positive system of nitrogen molecule $N_2(2+)$ measured at frequency of signal generator 4 kHz and simulated by the program SPECAIR at $T_v^* = 3000$ K and $T_r^* = 300$ K are shown on Fig. 3. All this spectra were normalized on maximum at wavelength $\lambda_n = 337$ nm.

Temperature dependences of vibrational and rotational excited levels population of second positive system of nitrogen molecule $N_2(2+)$ at different air flow rates lengthways (Fig. 4a) and across (Fig. 4b) to direction of current lines are shown on Fig. 4.

Rotational temperature T_r^* of excited levels population of second positive system $N_2(2+)$ is independed from direction and rate of air flow and numerically equal 300 K. Vibrational temperature T_v^* decreased with presence of air flow lengthways and across to current lines (Fig. 4). Power input in discharge correlated with frequency of signal generator very well. Vibrational temperature T_v^* has maximum at frequency 4.2 kHz. This is due to the fact that power inputted in discharge has maximum at this frequency. T_v^* is decreased with increasing of air flow speed from 0 to 0.05 Mach in direction lengthways to current line. Vibrational temperature was not changed at increasing air flow speed from 0.05 to 0.1 Mach (Fig. 4a). Another situation is observed when air flow directed across to current lines. T_v^* decreased (Fig. 4b) more than in case when flow directed lengthways (Fig. 4a) to current lines with increasing of air flow speed from 0 to 0.05 Mach. Vibrational temperature T_v^* was increased at increasing of air flow speed from 0.05 to 0.1 Mach (Fig. 4a).

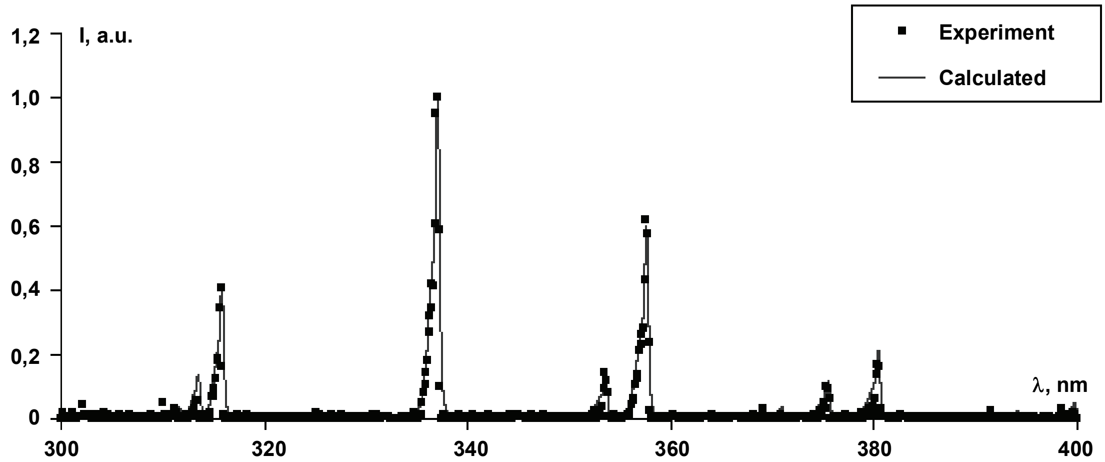

Fig. 3. Emission spectra of $N_2(2+)$ measured experimentally and simulated by the program SPECAIR at $T_v^* = 3000$ K and $T_r^* = 300$ K

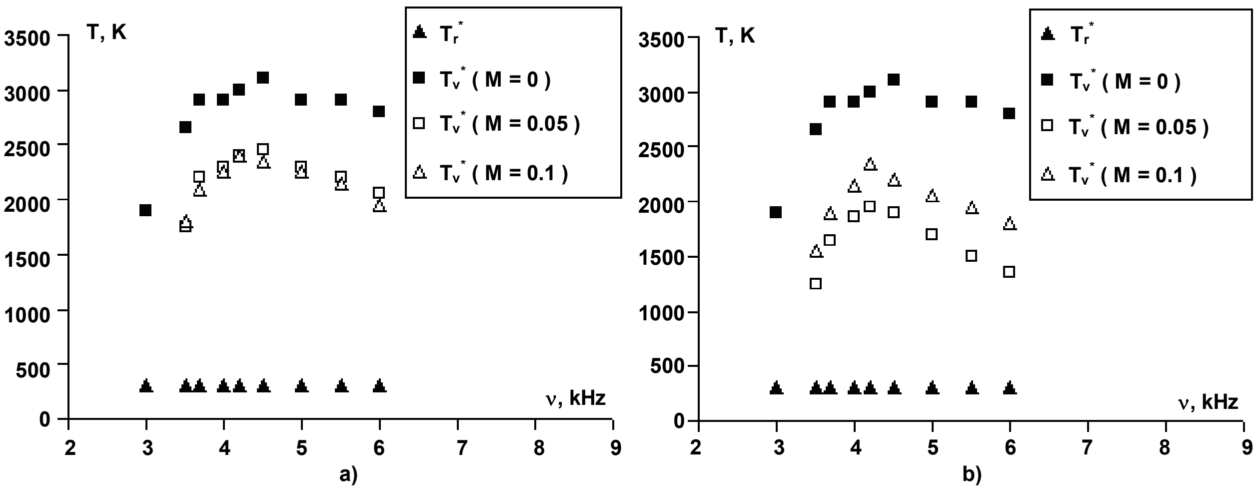

Fig. 4. Dependence of vibrational T_v^* and rotational T_r^* temperatures of $N_2(2+)$ from frequency of signal generator at different air flow rate lengthways (a) and across (b) to direction of current lines

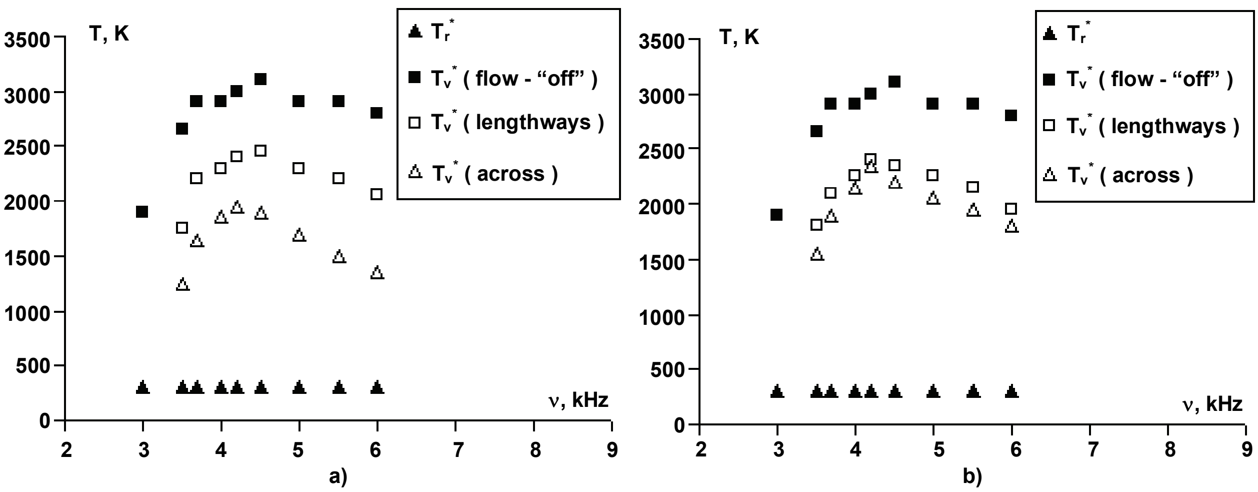

Fig. 5. Dependence of vibrational T_v^* and rotational T_r^* temperatures of $N_2(2+)$ from frequency of signal generator and air flow direction to current lines at different flow speeds 0.05 Mach (a) and 0.1 Mach (b)

Dependence of vibrational T_v^* and rotational T_r^* temperatures from frequency of signal generator and air flow direction to current lines at different flow speeds 0.05 Mach (Fig. 5a) and 0.1 Mach (Fig. 5b) are shown on Fig. 5. Direction of air flow to the current lines has effect on the temperature value of vibrational T_v^* excited levels population at air flow speed 0.05 Mach. Direction of air flow to the current lines has not effect on the vibrational temperature T_v^* at air flow speed 0.1 Mach.

Conclusions.

The rotational temperature of excited levels population of second positive system of nitrogen molecule $N_2(2+)$ is independent from air flow direction and rate in the range of air flow speeds from 0 to 0.1 Mach.

Plasma of DBD has the maximum temperature difference of vibrational T_v^* and rotational T_r^* at frequency of signal generator 4.2 kHz, which correspond to maximum of power supply.

1. *Corke T.C., Post M.L., Orlov D.M.* Single Dielectric Barrier Discharge Plasma Enhanced Aerodynamics: Physics, Modeling and Applications // Plasma Enhanced Aerodynamics. – 2007. 2. *Laux C.O.* Internet source: http://www.specair-radiation.net. 3. *Prisyazhnevich I.V., Chernyak V.Ya., Olszewsky S.V., Solomenko Ok.V.* Determination of excitation temperatures for vibrational and rotational molecular levels in an atmospheric-pressure gas-discharge plasma // Ukr. J. Phys. – 2010. – Vol. 55, № 10.

Submitted 21.06.2011

UDC 535. 36

V. Obukhovsky, Dr. Sci., V. Nikonova, post grad. stud., O. Ilchenko, post grad. stud.

NONLINEAR DIFFUSION IN BINARY SOLUTION WITH FORMATION COMPLEX OF 1-1 TYPE

It is considered the process of mass transfer in some molecular solutions, taking into account chemical reactions. It is obtained material parameters of intermolecular complexes with a simplifisd model based on the three componential solution.

Keywords: nonlinear diffusion, molecular solutions, intermolecular complexes, chemical reactions, associates, effective diffusion coefficient, enthalpy, concentration.

Розглянуто явище масопереносу у деяких молекулярних розчинах з урахуванням хімічних реакцій. За допомогою спрощеної моделі на базі трьохскладової суміші отримано матеріальні параметри міжмолекулярних комплексів.

Ключові слова: нелінійна дифузія, молекулярні розчини, міжмолекулярні комплекси, хімічні реакції, асоціати, ефективний коефіцієнт дифузії, ентальпія, концентрація,.

Introduction. This paper analyzes the phenomenon of nonlinear diffusion in molecular solutions, taking into account chemical reactions as inseparable process of mass transfer phenomena. The main problem is to use a general theory to a specific case – the ternary mixtures (two initial components and intermolecular complex). It is simplified model compared with real solutions. It is considered several binary solutions: acetone – benzene, benzene – cyclohexane, acetone – chloroform, toluene – benzene, cyclohexane – carbon tetrachloride.

Based on the obtained general formula for the effective diffusion coefficient, as only it is determined experimentally, it is obtained effective material parameters of intermolecular complexes and it is analysed presented results.

Development and discussion. This paper considers a nonlinear diffusion process, based on a model of exchange positions [2-3,9] and takes into account the inseparability of chemical reactions on mass transfer phenomena. In binary solutions of substances X and Y can be two-way reaction.

$$mX + nY \leftrightarrow X^mY^n. \qquad (1)$$

X and Y can be a single molecule of relevant substances and their associates, and m and n – number of corresponding particles in the complex. So we can see that molecules of pure substances and their molecular complexes participate in the processes of diffusion. In real solutions it is formed quasi complex from different molecular composition and X^mY^n is certain generalizations. Thus, the binary mixture is considered as three componential system (X, Y, X^mY^n). Basic equations used to describe such a system [4,7,9]

$$\begin{cases} \dfrac{\partial M_i}{\partial t} + \operatorname{div} \vec{j}_i = S_i, \\ \vec{j}_i = \sum\limits_j d_{ij}[M_j \nabla M_i - M_i \nabla M_j], \\ \sum\limits_{i=1}^{n} M_i = 1. \end{cases} \qquad (2)$$

Here i – the number of solution component, M_i –volume fraction of components i, j_i – volume's flow of *i*-substance, S function of sources for reactions (1), they are:

$$S_i = \alpha M_1^m M_2^n - \beta M_3, \qquad (3)$$

where α – a value that characterizes the probability of the complex formation, and β – probability of its decay.

Under this model, it can be found general expression for the effective diffusion coefficient as a function of solute concentration:

$$D_1^{ef}(M_1^{total}) = \frac{(d_{12} - q_{11}M_3) + \dfrac{\partial M_3}{\partial M_1}(\eta d_{23} + q_{11}M_1)}{1 + \eta \dfrac{\partial M_3}{\partial M_1}}. \qquad (4)$$

Where $M_1^{total} = M_1 + \eta_1 M_3$, – relative volume of first components both in pure form and in complex, $\eta_1 = \dfrac{m\Delta V_1}{m\Delta V_1 + n\Delta V_2}$ — volume fraction of 1 type molecules in the complex, $\Delta V_{1,2}$ – volume of the corresponding molecules, $d_{11} = d_{12} - d_{13} - \eta_1 d_{23} + \eta_1 d_{13}$. This derivative explicitly represented as

$$\frac{\partial M_3}{\partial M_1} = \frac{M_3[n(1 - M_1 - M_3) - mM_1]}{M_1(1 - M_1 - M_3 + mM_3)}. \qquad (5)$$

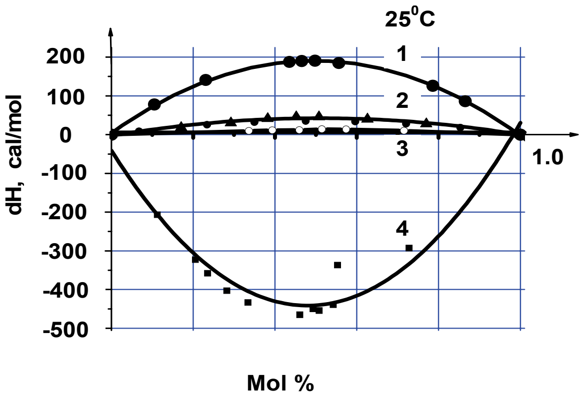

Fig. 1. Heat of mixing solution of 1 – benzene-cyclohexane, 2 – acetone-benzene, 3 – cyclohexane-carbon tetrachloride, 4 – acetone-chloroform

Analyzing the enthalpy of mixing data of molecular solutions acetone-benzene, benzene-cyclohexane, acetone-chloroform, toluene-benzene, cyclohexane-carbon tetrachloride [6], we can see that thermal functions symmetrical relative molar fraction of the first component of x = 0,5 (Figure 1).

For reasons of symmetry we assume that in such mixtures of simple molecular complexes formed of 1-1. We know that solutions are considered not able to form associates [9], so that for them we can applied the theory of nonlinear diffusion. Chemical reaction in these systems is look like:

$$A+B\leftrightarrow\left[A^1B^1\right]\equiv C. \qquad (6)$$

Analyzing the expression for the effective diffusion coefficient (4) can be found:

$$D_1^{ef}\left(M_1^{total}=0\right)=\frac{d_{12}+\left(\gamma\cdot\eta_1\right)d_{23}}{1+\left(\gamma\cdot\eta_1\right)}, \qquad (7)$$

$$D_1^{ef}\left(M_1^{total}=1\right)=\frac{d_{12}+\left(\gamma\cdot\eta_2\right)d_{13}}{1+\left(\gamma\cdot\eta_2\right)}, \qquad (8)$$

$$\frac{dD_1^{ef}}{dM_1^{total}}\left(M_1^{toalt}=0\right)=+2\left(\gamma\eta_1\right)\left(1+\gamma\right)\frac{\left(d_{12}-d_{23}\right)}{\left(1+\left(\gamma\cdot\eta_1\right)\right)^3}, \qquad (9)$$

$$\frac{dD_1^{ef}}{dM_1^{total}}\left(M_1^{total}=1\right)=-2\left(\gamma\eta_2\right)\left(1+\gamma\right)\frac{\left(d_{12}-d_{13}\right)}{\left(1+\left(\gamma\cdot\eta_2\right)\right)^3}, \qquad (10)$$

where $\frac{\partial M_3}{\partial M_1}\left(M_1^{total}=0\right)=\gamma$, $\frac{\partial M_3}{\partial M_1}\left(M_1^{total}=1\right)=\gamma\frac{1-\eta_1}{\eta_1}=\gamma\eta_2$.

Since the chemical reaction goes slower than the diffusion, from (2) we have $M_3\approx\gamma M_1(1-M_1-M_3)$ ($\gamma=\frac{\alpha}{\beta}$ – the ratio of corresponding probabilities of formation or decay of the complex). Using (7)-(10) we can found four parameters: d_{12}, d_{13}, d_{23}, γ.

As a result of mathematical processing of experimental data [1,5] it is found the diffusion coefficients of selected mixtures. Results of theoretical simulation presented in fig. 2. Found effective material parameters of the considered solutions are presented in Table.1.

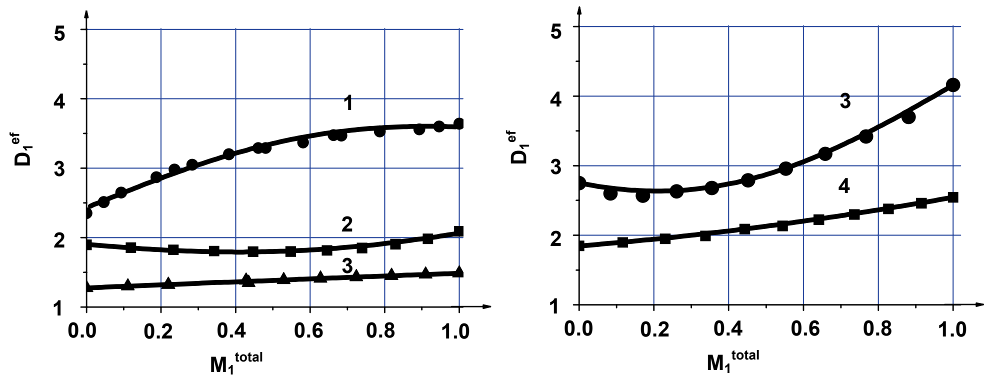

Fig. 2. Concentration dependence of diffusion coefficient 1 – acetone-chlorophorm, 2 – benzene-cyclohexane, 3 – cyclohexane-tetrachlormetane, 4 – acetone-benzene, 5 – benzene-toluene

Table 1. **Effective material parameters of the considered solutions**

Solution	ΔV_1, A^3	ΔV_2, A^3	η_1	d_{12}	d_{13}	d_{23}	γ
Benzene-cyclohexane	148,61	180,13	0,45	1,61	3,14	2,48	0,93
Acetone-benzene	122,60	148,61	0,45	2,18	7,24	3,83	1,17
Acetone-chlorophorm	122,60	132,43	0,48	3,71	3,43	0,47	1,36
Toluene-benzene	177,20	148,61	0,54	2,08	4,76	0,94	0,46
Cyclohexane-tetrachlormetane	180,13	160,23	0,53	0,31	1,39	2,18	0,56

As we can see the error of theoretical modeling for these mixtures does not exceed 5%.

As we can from the graphs for the dependence of diffusion coefficients on the concentration with "bulge down" (acetone-benzene, benzene-cyclohexane) characteristic ratio $d_{13}>d_{23}>d_{12}$, which can be explained by the slow cross of molecules of type 1 by molecules of type 2. Herewith is likely can form complexes 1-2. Therefore, diffusion is slowed down and observe a minimum of diffusion coefficient D_1^{ef}.

For the dependencies of "bulge up" (acetone-chlorophorm) characteristic ratio $d_{12}>d_{13}>d_{23}$, ie by the increase of complexes number the diffusion ia accelerated, which allows to watch the maximum on the graph.

For almost linear dependences (toluene-benzene, cyclohexane-tetrachlormetane) is rather small factor γ (ratio of probability of formation and decay of complexes), indicating a small amount of third component in the mixture.

Conclusions. This paper is demonstrated the possibility of using nonlinear diffusion theory to describe mass transfer phenomena in certain liquids. As a result of chemical reactions the binary solution is actually multi-component, and in the simplest case it consists of three components (molecules chemically do not change, but with some probability "attached" to each other).

On the example of the simplest solutions it is found material parameters of complexes and it is analyzed the features of diffusion in these systems.

Theoretical simulation is showed good correspondence with experimental data and it is testifies to the applicability of the theory of nonlinear diffusion to simple solutions.

1. *David W. McCall, Dean C. Douglass.* Diffusion in binary solutions // J. Phys. Chem. – 1967. – Vol. 71. – P. 987–997. 2. *Gyulnazarov E.S., Obukhovsky V.V., Smirnova T.N.* Theory of holographic recording on a photopolymerized material // SPIE "Milestone Seria". – 1996. – Vol. 130. – P. 473–475. 3. *Karpov G.M., Obukhovsky V.V., Smirnova T.N., Lemeshko V.V.* Spatial transfer of matter as a method of holographic recording in photoformers // Opt. Communication. – 2000. – Vol. 174, № 5–6. – P. 391–404. 4. *Karpov H.M., Obukhovsky V.V., Smirnova T.N.* Generalized model of holographic recording in photopolymer materials // Semiconductor Physics, Quantum Electronics & Optoelectronics. – 1999. – Vol. 2, №3. – P. 66–70. 5. *Oleg O. Medvedev and Alexander A. Shapiro.* Modeling diffusion coefficients in binary mixtures // Fluid Phase Equilibria. – 2004. – Vol. 225. – P. 13–22. 6. *Белоусов В.П., Морачевский А.Г.* Теплоты смешения жидкостей. – Л.: Химия ЛО. – 1970. 7. *Обуховський В.В., Нікінова В.В.* Взаємодифузія у водному розчині етилового спирту // УФЖ. – 2010. – Vol. 55, №8. – С. 891–896. 8. Физическая энциклопедия // Под. ред. Прохорова. – М.: Наука, 1988. 9. *Гріднева Ю.В., Обуховський В.В.* Вплив міжмолекулярної взаємодії на дифузію в рідинах // Вісн. Київ. ун-ту. – 2003. – № 3. – С. 284–288.

Submitted on 15.05.2011

UDC 535.4

D. Podanchuk, Ph. D., V. Kurashov, Ph. D., M. Kotov, adv. eng.,
V. Dan'ko, adv. eng., O. Parhomenko, post grad. stud.

WAVEFRONT SENSOR BASED ON THE TALBOT EFFECT

The wavefront sensor based on the Talbot effect is examined experimentally. The factors that allow changing an angular measurement range and a spatial resolution of the sensor are discussed. A comparative analysis with the Shack-Hartmann sensor is illustrated with some experimental results.
Keywords: wavefront sensing, Talbot effect, Fresnel mage.

В роботі експериментально досліджено сенсор хвильового фронту заснований на ефекті Талбота. Розглянуті фактори, що дозволяють змінювати кутовий вимірювальний діапазон сенсора та його просторове розрізнення. Порівняльний аналіз даного сенсора з сенсором хвильового фронту Шека-Хартмана проілюстровано деякими експериментальними результатами.
Ключові слова: сенсор хвильового фронту, ефект Талбота, зображення в зоні Френеля.

Introduction. Wavefront measurements are important in many fields of applied optics: wave front control of laser beams [2], optical diagnostics of the surface [7], human eye aberration measurements [1], etc. Today the Shack-Hartmann sensor is widely used for measuring wave fronts. The principle of work of the sensor is based on measuring the local slopes of the tested wave front with further reconstruction of its distribution [3]. The sensor consists of the lenslet array and CCD-photodetector located at the focal plane of the lenslets. The lenslets produce point images on the photodetector when the spatial coherent light beam falls on lenslet array. The shift of each image from respective optical axis is directly proportional to the local slope of the wave front in the corresponding lenslet subaperture and can be easily defined. The usage of the Shack-Hartmann sensors is complicated by the contradiction between their angular sensitivity and spatial resolution. Usually, the spatial resolution is determined by the lenslet sizes. Reducing the diameter of the lenslets leads, in fact, to reducing its focal length that affects the accuracy of the wavefront reconstruction.

A good alternative to the Shack-Hartmann sensor can be a sensor based on the Talbot effect [8]. Its principle is the self-reconstruction of the image of a linear diffraction grating at the certain distances behind the grating without any optical system due to interference of diffracted waves while the grating is illuminated by monochromatic plane beam. The grating image is distorted when an optically inhomogeneous object is put between the grating and the self-imaging plane.

This occurs because the spatial harmonics gets different phase shifts while passing through different parts of the object. Degree of the image distortion describes the object quality.

Talbot effect was used for wavefront sensing first time in [8]. Further development of the idea is found in [9, 4]. Interesting results are obtained in [5] when the wavefront sensor based on the fractional Talbot effect is proposed. It is shown in theory that for a slowly varying phase distribution the local shifts in the Fresnel images that take place in the presence of wavefront aberrations can be related to the local wavefront slope. Paper [6] presents the results of computer simulation of the diffraction wave front sensor based on the Talbot effect. But the comparative analysis with the Shack-Hartmann sensor is not carried out in any above-mentioned works. This specific question is addressed in the present paper.

Basic theory. Let's consider the imaging of the periodic structure with infinite aperture in the Fresnel diffraction region. The transmission function $\tau(x,y)$ of the grating can be represented as the product of two Fourier series according to x and y axes:

$$\tau(x,y)=\sum_{m=-\infty}^{\infty} a_m \exp(i2\pi\frac{m}{d}x)\cdot\sum_{n=-\infty}^{\infty} a_n \exp(i2\pi\frac{n}{d}y), \quad (1)$$

where d is the grating period, a_m, a_n are the Fourier coefficients, m, n are integers.

If the plane wave falls on the grating in z direction then the complex field amplitude at the observing plane (x_0, y_0, z) can be written with the Fresnel diffraction integral:

$$u(x_0,y_0,z)=\frac{\exp\left(i\frac{2\pi}{\lambda}z\right)}{i\lambda z}\times \\ \times\iint_{-\infty}\tau(x,y)\cdot\exp\left\{\frac{i\pi}{\lambda z}\left[\left(x_0-x\right)^2+\left(y_0-y\right)^2\right]\right\}dxdy. \quad (2)$$

After some transformation [10] with the neglecting of insignificant phase factor, the expression (2) can be written as:

$$u(x_0,y_0,z)\cong\sum_{m=-\infty}^{\infty} a_m \exp\left(i2\pi\frac{m}{d}x\right)\exp\left(-i\pi\frac{m^2\lambda z}{d^2}\right)\times \\ \times\sum_{n=-\infty}^{\infty} a_n \exp\left(i2\pi\frac{n}{d}y\right)\exp\left(-i\pi\frac{n^2\lambda z}{d^2}\right). \quad (3)$$

From this expression we can see that in case of an infinite aperture the field behind the grating is proportional to its transmission function $\tau(x,y)$ at the planes $Z_T=2\ell d^2/\lambda$ (ℓ is an integer) or to the half-period shifted transmission function $\tau(x+d/2,y+d/2)$ at the planes $Z_T^1=\left(2\ell+1\right)d^2/\lambda$.

Now suppose that the phase of the unit amplitude plane wave incident on the grating is varies linearly with coordinate x:

$$u(x)=\exp(-i2\pi\frac{\theta}{\lambda}x), \quad (4)$$

where θ a the wave incidence angle, λ is an wavelength. Then one can show easily that the field behind the grating at the planes $Z_T=2\ell d^2/\lambda$ is proportional to its transmission function $\tau(x+Z_T\cdot\theta,\ y)$ which is shifted into the x direction. This makes possible to determine the local tilts of the wave front incident on the grating by the measuring spot shifts on the grating images at the appropriate planes Z_T.

However, there is some limitation when using the Talbot effect in wave front sensors. First, the spot image shift caused by the wavefront tilt should not exceed half the grating period to avoid ambiguity in the wavefront tilt measurements: $Z_T\cdot\theta \le d/2$. This limits the maximum value of the tilt, which can be measured at the different planes Z_T:

$$\theta\le\frac{\lambda}{4\ell d} \quad (5)$$

As follows from (5), the maximal measurable tilt decreases with the increasing ℓ. However, at the same time the sensitivity to small tilt measurements is increases.

Secondly, the self-imaging phenomenon is an integral effect that imposes additional restrictions on the measurable value of the local tilts of the incident wave front. We can assume that each subaperture where incident wave front is considered as quasiplane should exceed a few grating periods. In the next section we will try to answer these and other questions.

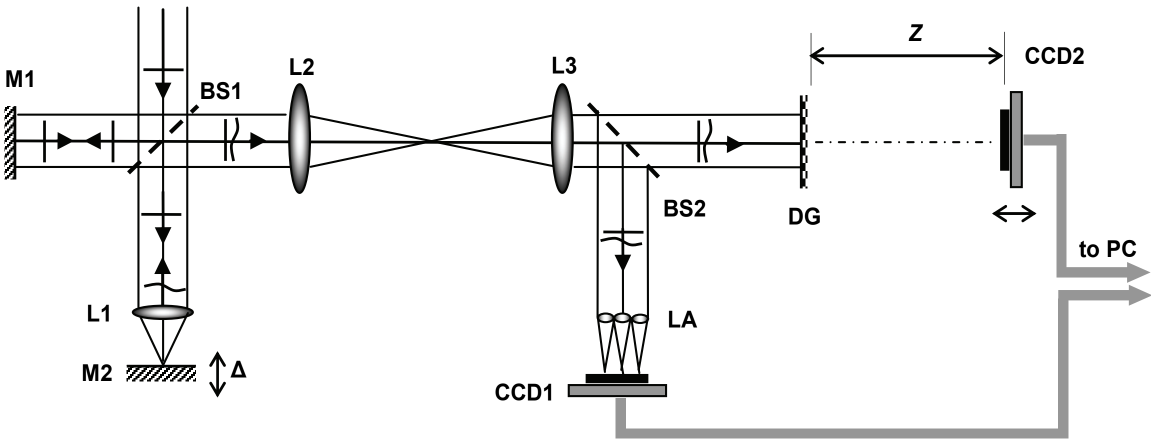

Fig. 1. Experimental setup for testing the sensor based on Talbot effect

Experiments. The capability of the wavefront sensor based on Talbot effect is assessed on the experimental setup depicted on Fig.1. He-Ne laser (λ=0.63 μm) is used as a coherent light source. Colimated laser beam is divided into two parts by the beamsplitter BS1. The beam reflected consecutively from BS1 and mirror M1 forms a reference plane wave. The beam passed through BS1 forms a test wavefront by the use of a lens L1 and mirror M2. Wavefront curvature is varied by the axial shift of the mirror M2 from focus of L1. The telescopic system of objectives L2–L3 and beamsplitter BS2 transmit the output plane of lens L1 to the two measuring planes in which the refractive lenslet array LA and, respectively, the two-dimensional diffraction grating DG are placed. The lenslets have a diameter of 0.4 mm and focal length of 24 mm. The photodetector CCD1 is placed at the focal plane of LA. Thus, in the first channel testing wave front is measured by the Shack-Hartmann sensor. The second channel is used for recording the self-image of DG at a distance *Z* by the photodetector CCD2.

The goal of the experimental researches was comparative analysis of the Shack-Hartmann sensor and the sensor based on Talbot effect by means of test wavefront measurements. First we consider the result of self-imaging periodic structure DG when the plane reference wave falls on it. Several two-dimensional binary amplitude gratings are used in experiments. They have a period *d* of 150 μm, 200 μm and 300 μm and a diameter of sub-apertures *b* of 150 μm, 200 μm and 300 μm, respectively. The transparencies were produced on photoplates PFG-1 by projecting on them reduced images of needed structures. Usually gratings have size of 8×8 mm. Grating image intensity distribution was measured at different Talbot plane, due to the possibility of moving the CCD2 along the optical axis of the system. Fig.2 shows the images of grating with *d* = 200 μm and *b* = 75 μm at the Talbot planes at the distances Z_T (125 mm) and 1.5 Z_T (190 mm). The transparency has only 13×13 periods, bounded by square on the figure. As one can see that the complete grating self-images are observed at corresponding (appropriate) planes, and the periodic image structure in case of 1.5 Z_T get shift of *d*/2 along *X* and *Y* axes. A little blur along the aperture edges and new periods addition is caused by finiteness of the grating aperture. Thus, the grating images on half-integer lengths Z_T can be used for wavefront measurements as well as on integer one.

In the next experiments dependence of curvature of test spherical wave (1/*R*) upon the shift of the mirror M2 from focus of the lens L1 (Δ) was measured by the Shack-Hartmann sensor and sensor based on Talbot effect with the set of different periodic gratings (Fig.3). The measuring results for different sensor types coincide within the error limits. The diagram shows that the Shack-Hartmann sensor was used for wavefront measurements in the range of −1.6…+2.1 m^{-1} despite the fact that full measurement range of the sensor is about ±5.0 m^{-1}. The measurement range of the sensor based on Talbot effect was changed depending on grating parameters. It was −1.2…+0.9 m^{-1} in case *d*=150 μm, *b*=75 μm as one can see on the digram. More narrow range (−1.6…+0.25 m^{-1}) give the grating with *d*=200 μm, *b*=100 μm and more narrow range (−0.6… + 0.2 m^{-1}) with *d*=200 μm, *b*=75 μm. The smallest measuring range ±0.1 m^{-1} was obtained with grating *d*=300 μm, *b*=150 μm (this case is not displayed on the figure).

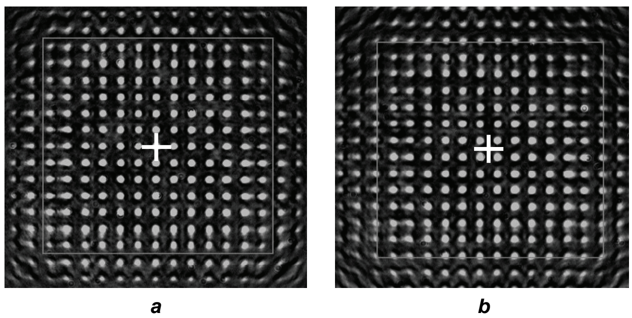

Fig. 2. The grating images (*d* = 200 μm, *b* = 75 μm): a) at Z_T-planes; b) at 1.5 Z_T-planes

Analysis of the received results showed that the grating period *d* is main parameter defining the metrological property of the diffractive wavefront sensor. It defines the distance Z_T for a certain wavelength, i.e. the base used for measurement of shifts of light spots on grating image. The measurement range of the sensor decreases with increasing *d* from 150 μm to 200 μm, as it seen from the diagram. It can be caused by the fact that the *d* increasing leads to the light spots blurring. The image patches of diffractive grating with different periods received with the same spherical wave front are shown on the Fig.4. The spots are too blurred for grating with greater period, therefore the centroid calculations and, accordingly, curvature estimations find difficulty. Also, measuring range for gratings with the same period is affected by the ratio of grating period to diameter of its transparent subapertures: *s* = *d/b*. Comparing the gratings (*d*=200 μm, *b*=100 μm) and (*d*=200 μm, *b*=75 μm), we can assume that optimal *d/b* ratio (in terms of increasing the measuring range of the sensor) is 2.

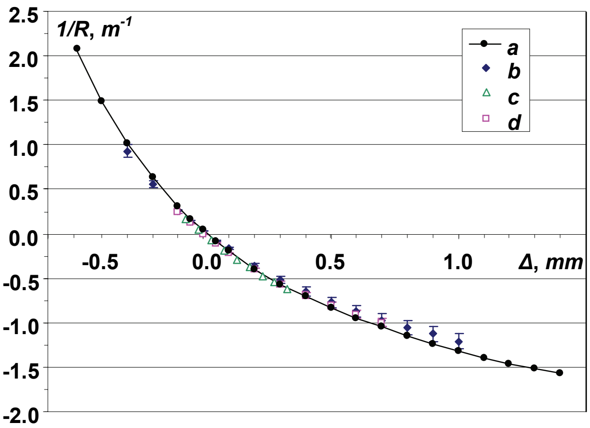

Fig. 3. The dependence of curvature of test spherical wave upon the shift of the mirror M2 from focus of the lens L1 measured by the Shack-Hartmann sensor (a) and sensor based on Talbot effect with different periodic gratings: b) *d* = 150 μm, *b* = 75 μm; c) *d* = 200 μm, *b* = 75 μm; d) *d* = 200 μm, *b* = 100 μm

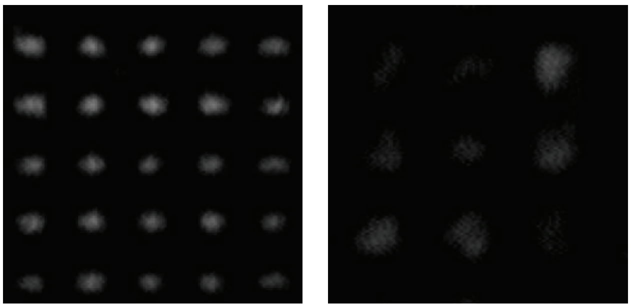

a *b*

Fig. 4. The image patches received with spherical wave front (*R*= −1 m) for different diffraction gratings: a) *d* = 150 μm, *b* = 75 μm; b) *d* = 200 μm, *b* = 75 μm

It can be mentioned, that light spot position estimation is related to the spot size. In the sensors based on Talbot ffect the size of light spots and distances between them can be substantially reduced, because in this design, unlike the Shack-Hartman sensor, the phenomenon of diffraction is not blurring light spots, but rather forms the structure of intensity distribution in the grating image. Thus, this sensor has better accuracy and spatial resolution. Also, the spot shift measuring base can be increased by working on half-integer distances of Z_T without changing the grating parameters. Fig. 5 shows fragments of hartmannogram for the Shack-Hartman sensor (a) and image of grating (*d*=200 μm, *b*=75 μm) at planes of Z_T (b) and 1.5 Z_T (c) for the same subaperture. Enlarged view of the spot images, received simultaneously for the reference plane wave front and the test spherical wave front with curvature radius *R* = 6.1 m, is given on the figure. As one can see, the spots are practically not separated in the Shack-Hartmann sensor (distance between them is less 2 pixels). In case of the sensor based on Talbot effect, the distance between the spots increases when the measuring base *Z* increases. It allows, we suppose, expanding the measurement range of the diffraction sensor on the small angles side quite easily, without changing the gratings.

Finally, we'll give an example of measuring the astigmatic wave front by the Shack-Hartmann sensor and the sensor based on Talbot effect. Fig.6 shows the joint hartmannogram of reference and test wave front (a) and the analogous grating images at different imaging plane (Z=Z_T=125 mm (b), Z=1.5 Z_T=180 mm (c), Z=2Z_T=250 mm (d)). Actually, these images can be considered as interferograms of the tested wave front and the reference plane wave front. The corresponding phase maps of the reconstructed wave front are shown on Fig.6(e–h). The interferograms are not practically differ from one another, as well as the topograms reconstructed from the measurement results received with the different sensors (are not differ too).

Fig.7 shows the sets of Zernike coefficients calculated from the wavefront measurement data received by the Shack-Hartmann sensor and the sensor based on Talbot effect at three different image planes. As one can see from the diagram, the most of expansion coefficients C_n are coincide with each other. Astigmatism coefficients $C_{4,5}$ are the same to within 3% for all measurements.

Conclusions. The comparative analysis of the diffraction sensor based on the Talbot effect and geometric Shack-Hartmann sensor shows that they have some similar features despite the different principles of work. These are optical setup for information registration, measurements of the spot shifts on the hartmannograms or the grating images, and the same software. But the sensors have some differences too. In the Shack-Hartmann sensor the spot shift is proportional to the local tilt of the test wave front in the corresponding subaperture. As the result measurement range and the spatial resolution are practically depend on parameters of the lenslet array only. We use the lenslet array, which provides the angular measurement range of ±5 m^{-1} and the spatial resolution of 400 μm.

In contrast to the Shack-Hartmann sensor, the diffractive sensor is quite easier and more functionally adaptable. The entrance element of the sensor is a binary grating. The grating producing is simpler against the producing of the lenslet array, than the grating parameters can be changed easier.

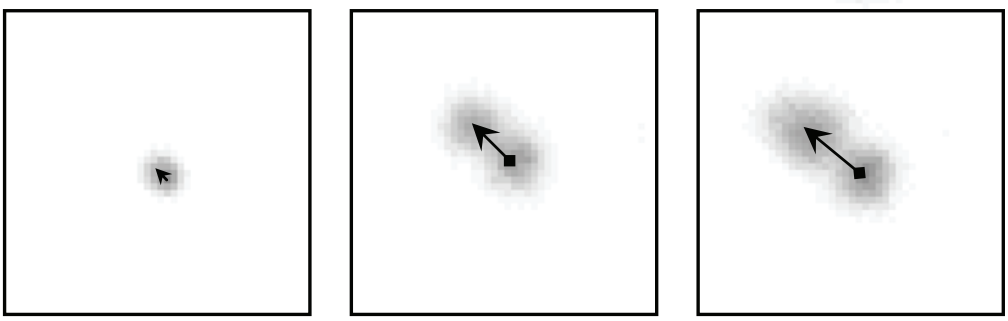

a *b* *c*

Fig. 5. Enlarged subareas of the hartmannogram (a) and image of grating (*d*=200 μm, *b*=75 μm) at planes of Z_T (b) and 1.5 Z_T (c)

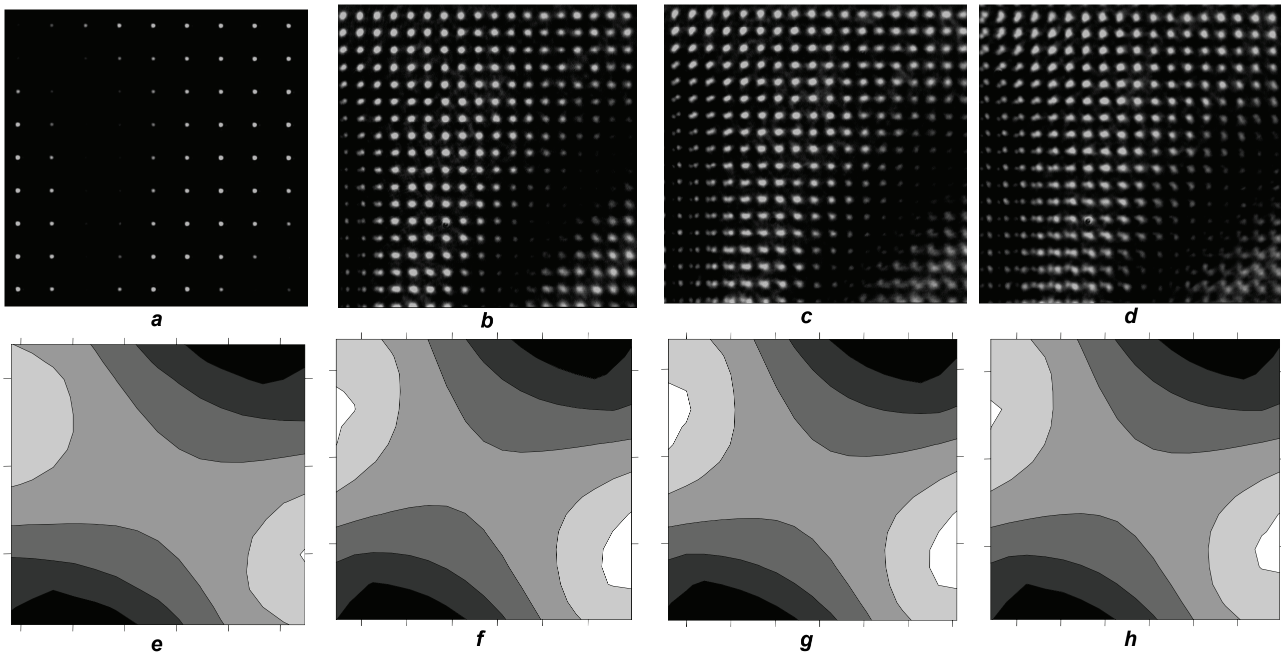

Fig. 6. Joint hartmannogram (*a*), grating images (*b, c, d*) and corresponding reconstructed phase maps (*e-h*) at different image planes: *f*=24 mm (*a, e*); $Z=Z_T$=125 mm (*b, g*), Z=1.5 Z_T=180 mm (*c, g*), $Z=2Z_T$=250 mm (*d, h*)

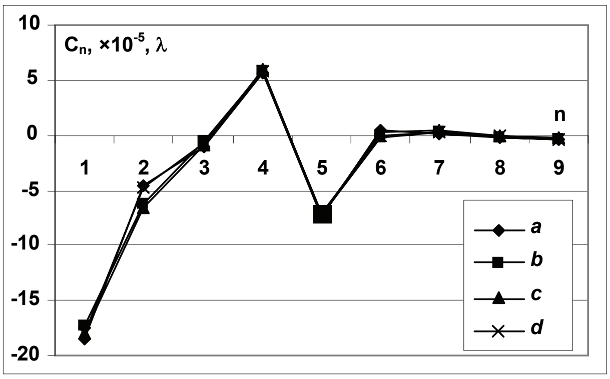

Fig. 7. The Zernike coefficients for the wavefront reconstruction with the Shack-Hartmann sensor (a) and sensor based on Talbot effect (grating with *d*=200 µm, *b*=75 µm) for the different grating image planes: $Z=Z_T$=125 mm (b), Z=1.5 Z_T=180 mm (c), $Z=2Z_T$=250 mm (d)

In addition, the grating period can be quite smaller in comparison with the lenslet size because in the sensor based on the Talbot effect images have no blurring caused by beam diffraction. In our experiments spatial resolution of the diffractive sensor reaches the value of 150 µm. Also grating period decreasing leads to increasing the measurement range up to greater tilt value (−1.2 – +0.9 m^{-1}) under condition of optimal grating fill factor. Moreover, the measurement range of the sensor can be expanded to the small tilt values, without grating period changing, by increasing of the measurement base *Z* and working at multiple or fractional Talbot distances. However, it should be noted that its total angular range (1.2 m^{-1}) is significantly smaller than corresponding range of the Shack-Hartmann sensor (5 m^{-1}).

1. *Molebny V., Kurashov V., Podanchuk D. et al.* Aberration mapping for sight correction // Proc. SPIE. – 1998. – Vol. 3246. – P. 238–247. 2. *Podanchuk D., Kurashov V., Kovalenko A. et al.* Measurement of light-phase distortions in an acousto-optical deflector with Shack-Hartmann wavefront sensor // Proc. SPIE. – 1999. – Vol. 3904. – P.311–318. 3. *Rousset G.* Wavefront sensing // Adaptive Optics for Astronomy / Ed. by D.M. Alloin and J.-M. Mariotti. – Dordrecht; Boston; London, 1994. 4. *Salama N., Patrignani D., De Pasquale L., Sicre E.* Wavefront sensor using the Talbot effect // Opt. Laser Technol. – 1999. – Vol. 31. – P. 269–272. 5. *Siegel C., Loewenthal F., Balmer J. E.* A wavefront sensor based on the fractional Talbot effect // Opt. Commun. – 2001. – Vol. 194. – P. 265–275. 6. *Арчакова Е., Козлов Н.* Дифракционный датчик волнового фронта // Известия Самарского научного центра РАН. – 2010. – Т. 12, № 4. – С. 134–137. 7. *Голобородько А., Григорук В., Котов М. та ін.* Визначення локальних дефектів поверхні сенсором хвильового фронту Шека–Хартмана // Український фізичний журнал. – 2008. – Vol. 53, № 10. – С. 946–951. 8. *Коряковский А., Марченко В.* Датчик волнового фронта на основе эффекта Тальбота // Журнал технической физики. – 1981. – Т. 51, № 7. – С. 1432–1438. 9. *Лобачёв В., Соколов В.* Амплитудно-фазовый датчик светового поля на основе эффекта Тальбота // Оптика и спектроскопия. – 1996. – Т. 81, № 1. – С. 119–126. 10. *Пальчикова И., Попова С., Смирнов С.* Сравнительное изучение самоизображения прозрачных решёток // Компьютерная оптика. – 2000. – Вып. 20. – С. 60–70.

Submitted on 09.06.2011

UDC 536.6

V. Sohatsky, Ph. D., Y. Shulimov, eng.

CURRENT AMPLIFICATION IN SPIN-DEPENDENT TRANSISTOR

Application of a spin-valve in transistor create the additional possibility for current control by means of the external magnetic field. The construction peculiarities and possible characteristics of one type of such a device are being considered in this paper.
Key words: spin transistor, magnetization, spin-valve, magneto-optics.

Застосування спінового клапану, поєднаного з транзистором, створює додаткову можливість регулювання струму за допомогою зовнішнього магнітного поля. В роботі розглянуто конструктивні особливості та характеристики одного з типів таких пристроїв.
Ключові слова: спіновий транзистор, намагнічування, спіновий клапан, магнітооптика.

Introduction. A spin-dependent transistor, that could be used as a binary logic element or non-volatile memory cell, have continuous interest as a base element of spintronic devices since it could have attractive characteristics of switching, amplification and non-volatility. Such a spin transistor (ST) must satisfy some contrary conditions for application as high magnetoresistance (change of electric resistivity in magnetic field), high operating frequency, high amplification capability (voltage, current and/or power gains), low power consumption, not too complicated structure, low-cost technology, etc.

Some types of ST were proposed during the last years as e.g. spin-diffusion transistor [6], spin-valve (SV) transistor [8], Datta–Das type spin field-effect transistor (FET) [3], magnetic bipolar spin transistor [4], spin metal–oxide–semiconductor field-effect transistor (MOS FET), [13], spin single electron transistor [2], spin-torque transistor [1], etc. However, realization of the STs met with a lot of problems, such as conductivity mismatch and formation of interfacial sublayer between ferromagnetic (FM) and semiconducting (SC) layers that caused polarized spin scattering; Fermi level pinning, etc. [5]. Although some advances were attained, the problems are still continuing to be studying.

In order to study the effect of magnetic field on electric current, passing through the stack film structure, we've prepared a few types of the SVs (ferromagnetic layers separated by non-magnetic one), deposited on SC substrate. Such structures were used for simulation and experimental check-up the process of remagnetization similar to those taking place in STs.

The aim of this work was also to evaluate the possibilities of current amplification in the SV-SC structures with different arrangement of the contact pads.

Models of spin transistors.

Spin injection is a critical requirement for the development of spintronics in general. Analyzing the spin injection in a FM metal/two-dimensional electron SC/FM metal structure in a diffusive regime [10], it was pointed out that since the SC parts have high resistance and it electrical conduction is not dependent on spin, so the overall resistance change is small when magnetization of the ferromagnets is being changed from parallel to anti-parallel. According to this model, it is difficult to achieve efficient spin injection into SCs in a diffusive regime if the degree of spin polarization in the FM metal is lower than 100%.

It was established [9] that use of magnetic tunnel junction (MTJ), (that are the SVs with thin (~1 nm) dielectric sublayer between FM layers) for spin injection should allowed to overcome the problems associated with the diffusive transport. One of the most efficient types of MTJ have MgO tunnel barrier. Furthermore, half-metallic ferromagnet electrodes using full-Heusler alloys would also have a great impact on the MTJ and ST technology. In these situations, recently developed MTJs exhibited a high tunneling magnetoresistance (TMR) ratio over 100% at room temperature, which is sufficient for ST operations and its applications to functional circuits such as non-volatile logic circuitries. The first successful fabrication of the so-called pseudo spin-MOSFET was presented in paper [11], where the spin-transistor operations controlled by magnetization configurations of the MTJ were successfully demonstrated.

One of the first constructions of bipolar ST [8] used a metallic spin-valve (SV) as a base electrode with alternative conductivity that could be shift by applied magnetic field. The voltage amplification of such a device was reached 300%, however the power gain was not enough at room temperature (RT). Some of the spin FET constructions proposed the last time had shown more promising characteristics [5], however such a reports are rare and usually not confirmed by another researches.

The structure of spin-FET is similar to that of Schottky source/drain MOS FETs [10] except the half-metallic (HM) source/drain contacts that are the HMF/Si junctions without a *pn* junction. Possible candidates for the HMF materials are CrO_2, Fe_2O_3 and FM SCs. Nonmagnetic (NM) contacts was also formed on the HMF source/drain.

Samples. The SVs were consisted from two FM Fe or NiFe layers, separated by non-magnetic metallic Cu or dielectric MgO sublayer, i.e. of 2 types: with conductive (Fe/Cu/FeNi) or dielectric (Fe/MgO/NiFe) sublayer. In some samples the SV FM layers had changing (wedged) thickness in order to study remagnetization in the layers with variable parameters. All the layers were prepared by thermal deposition on Si substrate with flat SiO_2 cap layer. Contacting Cu pads had the thickness of a few microns and allowed to pass the current in perpendicular or parallel to plane directions.

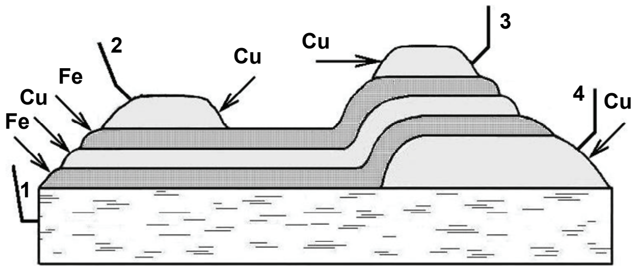

Fig. 1. Scheme of the explored stack structure

Experiment. Magnetooptical Kerr effect (MOKE) magnetometry was used for observation of remagnetization of both FM layers. The signal from the ground (adjoined to substrate) layer was about one order higher than a signal from the top NiFe layer. The reason of this was a small Kerr effect from NiFe surface as well as it oxidation due to contact with air.

Versions of the ST structure with a SV, that simply change conductivity between the input and output electrodes can work mainly in a key mode without amplification. In order to receive amplification index k>1 under applied magnetic field, it was proposed to use a SV as a component of the drain [11] or the contacts to source/drain electrodes, or a component of the domain wall control scheme [7]. In order to obtain the highest energetic efficiency of the ST, the energy of remagnetization must be as small as possible. So the anisotropy, saturation magnetization, thicknesses of the layers must be optimized in correspondence with the above conditions.

We've studied remagnetization of the spin-valves in a contact with SC while the electric current could flow through or along the stack structure in any case crossing the interfaces FM/NM, SC/FM. The thickness of the structure was determined as a proportion to the intensity of light, passing through the stack. Almost 6 times change of the intensity corresponded to differences in thicknesses of 3-layered stack from 80 till 110 nm with Fe (40-50 nm), Cu (10-20 nm) and NiFe (30-40 nm) layers.

Such a stack structure is too complicated for exact theoretical description especially in applied small magnetic fields because of inhomogeneities caused by domain structure. Nevertheless in most cases it is possible to consider it as monodomain and remagnetized by rotation of magnetization. Thus anisotropy axis could be determined e.g. by application of magnetic field parallel to in-plane easy anisotropy axis – in such case the hysteresis loop became almost exactly rectangular; it became nearest to linear with small remanence and coercivity when magnetization occur in the perpendicular direction (in the direction of hard anisotropy axis).

Results and discussion. The energy need for remagnetization of the SV is important component of the ST amplification efficiency. Therefore the field of SV remagnetization from this point of view must be as small as possible. Its typical value is about several tenths Oersted. The result of decreasing of this field is growing instability of SV magnetization that is manifested as accidental remagnetization.

In order to optimize characteristics of the SV incorporated in ST it's possible to: 1) technologically choose the orientations of magnetic anisotropy axes in FM layers; 2) choose the thicknesses of FM layers which determine the interlayer interaction; 3) choose the direction of applied magnetic field; 4) use polarized current, passed through the SV to assist it remagnetization.

In order to improve the ST efficiency by means of selecting mode of remagnetization the SV layers were deposited with alternative thickness. The hysteresis curves of both layers remagnetization were obtain with MOKE-magnetometer. Change of the interlayer interaction is obviously seen on Fig. 2, where non-monotonic curves number 1-6 have sharp peculiarities that evidenced an interlayer interaction. Just two sharp peaks on the reverse part of the loops (at approximately H_1 ~25Oe and H_2 ~50Oe) are the results of the hard (lower) and soft (upper) FM layer interaction in anisotropic matter. The above paculiarities and correspondent interaction are disappeared on the last loop without sharp peaks. Thus a strongest interaction corresponds to the third hysteresis loop. An optimum thickness of the stack must not exceed this value since further decreasing of magnetoresistance decrease the ST efficiency.

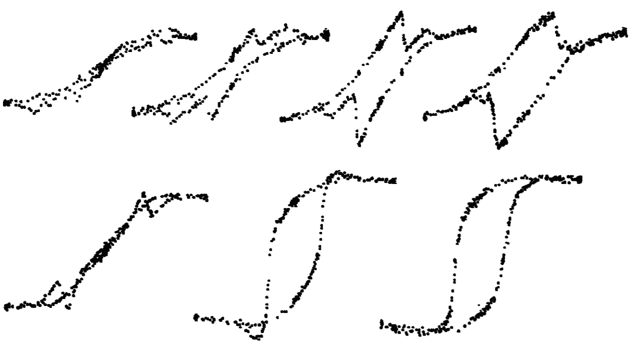

Fig. 2. Changes of MOKE hysteresis loop with thickness of the structure

The stack structure (Fig. 1) could operate in a binary mode when magnetic field is applied in the direction of easy anisotropy axis. In this case remagnetization loop of the soft layer has a rectangular shape. In analogous mode the field not parallel to easy axis and a loop shape determined by the angle between easy axes and correspondent magnetization of both layers. In both cases the structure is fit for modeling all main ST operations.

The *I-V* characteristics of such a ST were measured in a bias magnetic field mode; the output current depended on input voltage and changed applied magnetic field as shown on the graphs (Fig. 3, 4). The power consumption of the ST with external magnetic field source is higher than it's need when the source is a component of the ST. Lack of amplification in a presented geometry was confirmed by evaluation of the energy balance, that moreover assumed decreasing of the SV cell size (with corresponding increasing of demagnetization). Decreasing of the SV cell size did not decrease the remagnetizing field because of the enhanced coercivity.

The possible way to overcome the problem of small amplification is to use in one ST two SVs with various remagnetizing fields and MR. The second SV (with higher MR) should be used for control the ST current and the first SV (with lower switching field) for control remagnetization current of the second SV [7]. This way complicates the ST construction, however evaluations confirmed the amplification enhancement in such a case. Another way that was tried out in our experiments was a remagnetization with a polarized current assistance.

There were abrupt changes of current of about a few percent in switching field in totally metallic SV. At the same time the output current was near to linearly dependent on input voltage (Fig.3). Evaluation of the ST energy balance allowed to determine the most profitable directions of applied magnetic field relatively to the layer anisotropy axes as for key mode of the ST operation as for the highest amplification for different versions of the ST arrangement.

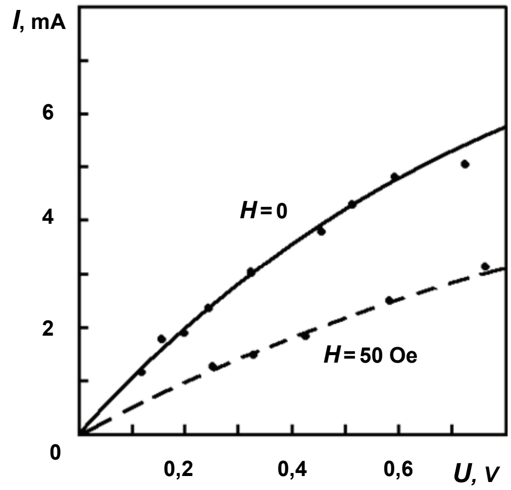

Fig. 3. Output currents vs input voltage & bias field

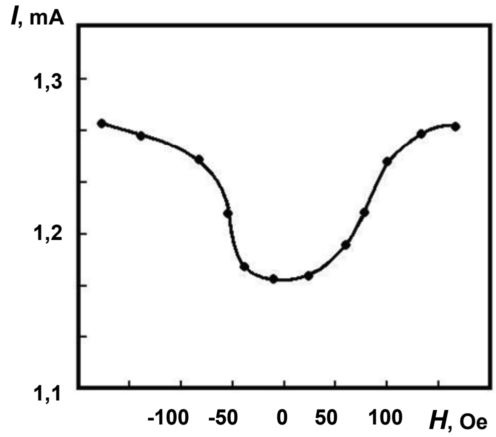

Fig. 4. Current vs magnetic field

We now compare the observed gain properties with the theoretical expectations using a method of [7] and discuss the scaling of our device. The input power is calculated as:

$$P_{in} = I^2 R = (2hH_c)^2 \cdot R ,$$

where I and R are wire current and input wire resistance, respectively. $H_c = I/(2h)$ is a required switching magnetic field (coercive force), where h is the wire width. H_c is assumed to be constant if the cell size L is larger than L_c (L_c = 2 mkm would be assumed in the calculation). For the small cells with $L \ll L_c$, H_c is assumed to be inversely proportional to L because of a large in-plane demagnetization field in small cells. Therefore, the input power is constant for small L and proportional to L^2 for large L.

The formula for output power calculations, taken from [7] is as following:

$$\Delta P = \frac{k \cdot V^2 \cdot \left(R_{\uparrow\downarrow} - R_{\uparrow\uparrow}\right)}{\left(R_{\uparrow\downarrow} + R_{\uparrow\uparrow}\right)},$$

where, V is the applied voltage, $R_{\uparrow\downarrow}$ and $R_{\uparrow\uparrow}$ are the resistances at various directions of magnetization. The factor k~4/3 appears because of the power sharing between the load and the SV. The output power is proportional to L^2, since a SV with larger area may provide larger output current. Therefore, following scaling rule is obtained for the power gain: $G \sim L$ if $L \gg L_c$, and $G \sim L^2$ if $L \ll L_c$.

The estimated power gain for the evaluated cases is constant for large cell size and it becomes smaller for small cell size. We can also recognize that the low resistance area value is very important parameter to obtain a high power gain. The power gain obtained in the experiment was only about 1% of the ideal expectation. This can be interpreted as the influence of the finite parasitic series resistance R_p in the line connecting the SV and waveguides. Including R_p, the gain has a peak at the optimum cell size, because the output power is mainly lost in the parasitic resistance for large SVs with small resistance. The experimental result was quantitatively in a good agreement with the theoretical expectation if we assume that $R_p = 10\,\Omega$. Similar scaling can be calculated for the current gain. We can also explain these experimental results by including the R_p. Although we could not obtain substantial current gain in this experiment, the calculation shows that a current gain of 10 could be obtained if the parasitic resistance could be reduced to 1 Ω. In the smaller sized device, less than 0,2 μ, it is difficult to realize the current gain in this architecture because of significant increase of H_c. To overcome this problem, use of the spin-transfer torque should be promising, as has been already proved in the development of MRAMs.

Conclusions. Since the ST discussed here has the optimum performance in sub-100 nm regime and it has a simple structure similar to shown on Fig. 1, one can expect the scaling merits by downsizing the ST. Therefore, the ST should satisfies all the requirements for spintronic integrated circuit applications.

Such a deposited and analyzed stack structure serves as a model of ST that can be presented as pseudo-FEST. The FEST was shown to have magnetization-dependent-output characteristics, high transconductance, amplification capability, low power consumption, low off-current and a simple structure compatible with Si-MOS technology, which are all important for integrated circuits applications. The FEST can be used as a key device for ultrahigh density nonvolatile memory and reconfigurable logic devices based on novel spintronic concepts.

1. *Bauer G. E. W., Brataas A., and van Wees B. J.* // Appl. Phys. Lett. 2003. – Vol. 82. – P. 3928. 2. *Bruckel H., Reiss G., Binzelberg H., Bertram M., Monch I., and Schumann J.* // Phys. Rev. – 1998. – Vol. B58. – R8893. 3. *Datta S. and Das B.* // Appl. Phys. Lett. – 1990. – Vol. 56. – P. 665. 4. *Fabian J., Zutic I., and Das Sarma S.* // Appl. Phys. Lett. – 2004. – Vol. 84. 5. *Fert A. and Jaffre's H.* // Phys. Rev. – 2001. – Vol. B64. – P. 184420 85. 6. *Johnson M.* // Phys. Rev. Lett. – 1993. – Vol. 70. – P. 2142. 7. *Konishi K. et al.* Current-Field Driven "Spin Transistor" // Appl. Phys. Expr. – 2009. – Vol. 2. – P. 063004. 8. *Lodder J. C., Monsma D. J., Vlutters R., and Shimatsu T.* The spin-valve transistor: technologies and progress // JMMM. – 1999. – Vol. 198–199. – P. 119–124. 9. *Rashba E. I.* // Phys. Rev. – 2000. – Vol. BE2. – R16267. 10. *Schmidt G., Ferrand D., Molenkamp L W., Filip A. T. and van Wees B. J.* // Phys. Rev. – 2000. – Vol. 162. – R4790. 11. *Shuto Y. et al.* A New Spin-Functional Metal–Oxide–SC Field-Effect Transistor Based on Magnetic Tunnel Junction Technology: Pseudo-Spin-MOSFET // Appl. Phys. Express. – 2010. – Vol. 3. – P. 013003. 12. *Sohatsky V., Shulimov Y.* Effect of current on spin-valve layer magnetization // Abstr. of V Int. Conf. "Functional Materials" (ICFM-2009), Partenit, Ukraine. – P. 172. 13. *Sugahara S. and Tanaka M.* // Appl. Phys. Lett. – 2004. – Vol. 84. – P. 2307.-7.

Submitted on 31.05.2011

UDC 537.6/.8

K. Shchyrba, stud., O. Prokopenko, Ph. D.

MICROWAVE SOURCES BASED ON MICROSTRIP RESONATOR WITH SPIN-TORQUE NANO-OSCILLATORS

A possibility of application of microstrip resonators (MSR) with embedded spin-torque nano-oscillators (STNO) as a microwave signal sources is briefly considered and the typical output microwave power from such type of microwave sources is calculated in the scope of previously developed lossless model. In the paper we expand this theoretical model by taking into account the losses in the system, thus, such important parameter of the MSR as an unloaded Q-factor is considered below as a variable parameter, which depends on the number of STNOs embedded into the MSR. This means that the performance of considered type of microwave sources depends on the number of STNOs embedded into the MSR and may be substantially lower for a large number of embedded STNOs than in the case of previously developed lossless model. The developed formalism can be used for optimization of the practical parameters of microwave signal sources based on STNO arrays.

Key words: spin-torque nano-oscillator, microwave power, microwave source, microstrip resonator, unloaded Q-factor.

Стисло розглянуто можливість застосування мікросмужкових резонаторів (МСР) з вбудованими у них магнітними наноструктурами (МНС) для створення генераторів мікрохвильових сигналів та розраховано в рамках моделі без втрат типову вихідну потужність подібних джерел мікрохвильового випромінювання. У роботі розвинена теоретична модель мікрохвильових генераторів зазначеного типу за рахунок безпосереднього врахування втрат у системі, що розглядається. Зокрема, такий важливий параметр МСР як його власна добротність у рамках моделі з втратами вже розглядається як змінна величина, яка залежить від кількості МНС вбудованих у резонатор. Відповідно характеристики мікрохвильових генераторів на основі МСР з багатьма МНС вже залежать від кількості МНС, вбудованих у резонатор, і можуть бути суттєво гіршими у випадку МСР з великою кількістю МНС ніж це передбачає модель без втрат. Розроблений в роботі формалізм може бути використаним для оптимізації практичних параметрів джерел мікрохвильових сигналів на основі МСР з масивом МНС.

Ключові слова: магнітна наноструктура, потужність мікрохвильового сигналу, мікрохвильовий генератор, мікросмужковий резонатор, власна добротність.

Introduction and outlines. One of the most perspective and rapidly developing branches of micro- and nanoelectronics is the magnetic nanoelectronics [2, 4–5, 14, 36, 46]. Nowadays the element base of this branch of science and technology is being quickly developed, especially in the area of spin-wave electronics. Most of presently used spin-wave devises are created using thin ferromagnetic films (for instance, yttrium-iron garnet films [1, 3, 11]) and intended for the realization of nonlinear interaction between two or more microwave signals [1, 3, 11, 23, 44, 51]. But today there are no sources and amplifiers of spin waves with acceptable scale and performance [36, 45–46]. This problem can be solved by using recently developed new active nano-scale magnetic devices – the spin-torque nano-oscillators (STNO) (Fig. 1) – and the microwave systems based on them [27–28, 32].

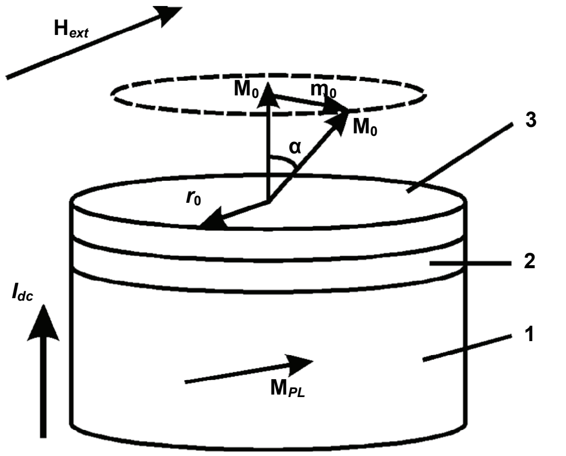

Fig. 1. The simplest model of spin-torque nano-oscillator (STNO) consists of three layers: "pinned" magnetic layer (PL) (1), thin non-magnetic spacer (2) and thin "free" magnetic layer (FL) (3). $\mathbf{M}_{PL}$ is the magnetization vector in the PL (1), defined by an external magnetic field $\mathbf{H}_{ext}$, geometry of the structure, etc. $\mathbf{M}_0$ is the magnetization vector in the FL (3). If direct bias current I_{dc} passing the structure from PL to FL a microwave precession of magnetization with the magnetization vector $\mathbf{M}_0$ is excited; α is the precession angle and $\mathbf{m}_0$ is the excited microwave component of magnetization vector

The discovery of the spin-transfer-torque effect in magnetic multilayers, theoretically predicted by J.C. Slonczewski [47, 48] and L. Berger [8] and after that experimentally observed by many authors [10, 16–18, 20–21, 27–28, 40–42, 50], has opened a possibility for a new method of generation of microwave oscillations that does not involve any semiconductor materials or devices [46]. The spin-transfer-torque effect turned out, that electric direct current I_{dc} passing through a magnetized magnetic layered structure becomes spin-polarized and, if the current density is sufficiently high (greater than current threshold I_{th}), this spin-polarized current can transfer enough spin angular momentum between the magnetic layers to destabilize the static equilibrium orientation of magnetization in the thinner ("free") magnetic layer (FL) of the multilayered structure (see fig. 1). Depending on the actual geometry and properties of the magnetic structure and the magnitude of the external bias magnetic field, this phenomenon can lead either to the magnetization switching (reversal of the magnetization direction) [18, 29], or to the magnetization precession with the frequency close to the frequency of the ferromagnetic resonance (FMR) in the magnetic layer [20–22, 39–41]. In the last case the frequency of the current-induced precession is close to the frequency of the most unstable spin wave mode of the FL (i.e. it is close to the FMR frequency), depends on the current magnitude, and, typically, lies in the microwave range. The typical eigen frequency of a STNO is 1÷50 GHz [14–15, 17], but there is theoretical prediction that it can be increased up to 200 GHz [15, 38–40].

The major advantages of the STNOs are its small sizes (the typical radius r_0 of the structure is 5÷500 nm, height of the structure is 10÷100 nm), compatibility of STNO fabrication technology with the standard micro- and nanoelectronics fabrication technology, the possibility of generation frequency tuning in a wide range [36, 46].

Practical applications of above described magnetization dynamics in non-volatile magnetic random access memory, microwave nanometer-scale oscillators, detectors, mixers and other devices are under development [10, 19, 52], and non-equilibrium states of magnetization induced by spin-transfer-torque are of fundamental interest in nonlinear science [15, 46, 54]. Also spin-transfer-torque effect is used in spin torque ferromagnetic resonance measurements of spin waves in magnetic nano-structures [9, 43, 50].

Microwave spin-torque nanometer-scale auto-oscillators based on either fully metallic giant magnetoresistance (GMR) spin valves or magnetic tunnel junctions, having a thin dielectric spacer and employing tunneling magnetoresistance (TMR) effect, are very attractive for potential applications in active nanometer-scale devices in microwave spintronics [46, 26–28, 31–34, 49]. The major problem that arises during the development and application of such devices is the small microwave output power that can be extracted from a single STNO. In the case of a STNO based on the GMR effect this power is relatively small (around one nW) [20–22, 24], while in the case of a STNO based on the TMR effect it can reach 1 μW [16, 25, 50]. But in most cases the microwave power emitted from a typical STNO is about 1÷10 pW due to the various undesirable effects like the impedance mismatch effect [17, 20, 24].

In all known to us experiments (for instance, see [10, 16–18, 20–21, 27–28, 40–42, 50]) the microwave signal generated by a STNO is registered, typically, as oscillations of the multilayer resistance through the GMR [20–22, 24] or TMR [16, 25, 50] effects due to the fact that in the course of precession the orientation of the magnetization of the FL relative to the static magnetization of the PL oscillates with microwave frequency. In this case, in fact, the time-dependent resistance of the STNO $R(t)$ is measured. The resistance $R(t)$ of a STNO depends on time t due to the existence of a microwave magnetization precession with angular frequency $\omega_0 = 2\pi f_0$ in the FL of the STNO. If the direct bias current I_{dc} passing through the STNO then the characteristic microwave power W_{MR} generated by a STNO can be estimated as

$$W_{MR} \sim \frac{1}{2} I_{dc}^2 R_{dc} \left(\frac{R_{rf}}{R_{dc}} \right)^2 , \qquad (1)$$

where R_{dc} and R_{rf} are the direct and microwave components of the STNO resistance, respectively.

The value of R_{rf} is several percents of R_{dc} (typically 1÷5 %) in real STNO devices [10, 16–18, 20–21, 25, 27, 28, 40–42, 50]. Thus, the efficiency of standard method of experimental observing the microwave power generated by a STNO is proportional to the square of the magnetoresistance (MR) coefficient R_{rf}^2 / R_{dc}^2 and due to this circumstance is low ($\sim 10^{-4}$).

In the paper we analyze another opportunities of detection of microwave power generated by a STNO. We consider a possibility of direct microwave signal detection as the microwave oscillations in the microstrip resonator (MSR) with several embedded STNOs. It was shown in [32–33] that the microstrip resonator has the smallest effective volume amongst the majority of existing microwave systems and has the high enough Q-factor. Due to these circumstances MSRs are very convenient for creation of practical devices involving STNOs.

However, the analysis was carried out and this conclusion was obtained for the case of lossless system, when the losses inserted into a MSR by each STNO was equal to zero. In real system Q-factor of MSR is decreased while the power losses are increased in the system, i.e. the number of STNOs is increased. Thus, below we analyze the performance of microwave signal sources based on MSR with embedded STNOs in the scope of lossy model based on the previous developed lossless model [32–33].

Lossless model. We make several natural assumptions during our analysis. First, we consider a STNO as a point object, because any size of typical STNO is much smaller than the wavelength λ_0 of the microwave signal. Second, we use the macrospin approximation and assume the microwave component of magnetization $\mathbf{m}_0 = \mathbf{x}m_x + \mathbf{z}m_z$ is circularly polarized, so we can simply write $\mathbf{m}_0 = (\mathbf{x}+\mathbf{z})m_0$ (see fig. 1). Third, using first and second assumptions we can consider a microwave magnetization precession in the FL of the STNO as the oscillations of two point linear magnetic dipoles oriented along *x*- and *z*-axis.

During the analysis we consider the case of STNO with following typical parameters: frequency of magnetization precession $f_0 = 10$ GHz, saturation magnetization of the FL of a STNO $\mu_0 M_0 = 800$ mT, STNO radius $r_0 = 100$ nm, thickness of the FL of STNO $d_0 = 5$ nm, so the volume of the FL is $V_0 = \pi r_0^2 d_0 \approx 153$ nm^3. We analyze only the case of maximal magnetization precession angle $\alpha_0 = 90°$. The last case is typically realized if direct current I_{dc} passing the structure is greatly exceeds the current threshold I_{th}.

In the following we do only qualitative analysis of microwave signal power emitted from a STNO. Thus, we can assume that the permittivity ε and permeability μ of the media are approximately equal to the vacuum permittivity ε_0 and vacuum permeability μ_0, respectively.

Theory based on lossless model. For the first time an approach to the analysis of electromagnetic fields generated by a STNO was presented in the recent paper by N. Amin, H. Xi, and M.X. Tang [7]. The authors of the paper [7] have obtained the expressions for the electromagnetic fields of a STNO considering it as a point magnetic dipole, but no quantitative study of the microwave power emitted from the STNO has been made. Later the model firstly presented in [7] was expanded and propagated on other microwave systems in papers [32–33].

We note, that the following derivations are based on the field expressions for linear magnetic dipole [7, 37]:

$$E_\varphi = -\frac{i\omega_0\mu_0 M_0}{4\pi} e^{-ik_0 r}\left(\frac{ik_0}{r} + \frac{1}{r^2}\right)\sin\theta\, e^{i\omega_0 t},$$

$$H_r = \frac{i\omega_0\mu_0 M_0}{2\pi} e^{-ik_0 r}\left(\frac{1}{Z_0 r^2} + \frac{1}{i\omega_0\mu_0 r^3}\right)\cos\theta\, e^{i\omega_0 t}, \quad (2)$$

$$H_\theta = \frac{i\omega_0\mu_0 M_0}{4\pi} e^{-ik_0 r}\left(\frac{i\omega_0\varepsilon_0}{r} + \frac{1}{Z_0 r^2} + \frac{1}{i\omega_0\mu_0 r^3}\right)\sin\theta\, e^{i\omega_0 t},$$

where $i = \sqrt{-1}$, $k_0 = 2\pi/\lambda_0$, $Z_0 = \sqrt{\mu_0/\varepsilon_0}$ – media impedance. The detailed analysis involving Eqs. (2) for different microwave systems is presented in [32].

Microwave resonators with STNO: general analysis. Further we shall analyze the excitation of oscillations in microwave resonators by a STNO. We begin the analysis by writing Maxwell's equations for the electromagnetic field $\mathbf{E}$, $\mathbf{H}$, excited by an external magnetic current with density $\mathbf{j}^m = 2\pi i f_0 M_0(\mathbf{x}+\mathbf{z})$:

$$\mathrm{rot}\,\mathbf{E} + i\omega\mu_0\mathbf{H} = -\mathbf{j}^m,\ \mathrm{rot}\,\mathbf{H} - i\omega\varepsilon_0\mathbf{E} = 0. \quad (3)$$

The fields $\mathbf{E}$, $\mathbf{H}$ can be presented as a series expansion by eigen fields $\mathbf{E}_n$, $\mathbf{H}_n$ of the resonator and some gradient functions [1]:

$$\mathbf{E} = \sum_n A_n\mathbf{E}_n - \mathrm{grad}\,\Psi_e,\ \mathbf{H} = \sum_n B_n\mathbf{H}_n - \mathrm{grad}\,\Psi_h, \quad (4)$$

where n is the generalized mode index. The eigen fields $\mathbf{E}_n$, $\mathbf{H}_n$ are the solution of the uniform equations:

$$\mathrm{rot}\,\mathbf{E}_n + i\omega_n\mu_0\mathbf{H}_n = 0,\ \mathrm{rot}\,\mathbf{H}_n - i\omega_n\varepsilon_0\mathbf{E}_n = 0. \quad (5)$$

The eigen fields and gradient functions satisfy the following orthogonal conditions [1]:

$$\varepsilon_0\int_V \mathbf{E}_n^*\mathbf{E}_{n'}dV = N_n^e\Delta_{nn'},\ \mu_0\int_V \mathbf{H}_n^*\mathbf{H}_{n'}dV = N_n^h\Delta_{nn'},$$

$$\varepsilon_0\int_V \mathbf{E}_n^*\,\mathrm{grad}\,\Psi_e dV = \mu_0\int_V \mathbf{H}_n^*\,\mathrm{grad}\,\Psi_h dV = 0,$$

$$\Delta_{nn'} = \begin{cases} 1, & n = n' \\ 0, & n \neq n' \end{cases}. \quad (6)$$

From Eqs. (3)–(6) we can obtain the expressions for the coefficients A_n and B_n:

$$A_n = \frac{\omega\omega_n}{\omega_n^2 - \omega^2}\frac{G_n}{N_n^h},\ B_n = \frac{\omega^2}{\omega_n^2 - \omega^2}\frac{G_n}{N_n^h}, \quad (7)$$

where $G_n = \mu_0\int_V \mathbf{H}_n^*\mathbf{m}dV$. It is certainly A_n and B_n are infinite at the frequency $\omega = \omega_n$. But this case is the most important and interesting. To analyze the excitation of the resonator at the frequency $\omega \approx \omega_n$ we introduce the Q-factor of the resonator $Q_n = \frac{\omega_n}{|\omega_n - \omega|}$ and assume $Q_n \gg 1$. In that case Eq. (7) is transformed to the following

$$A_n \approx \frac{1}{2}Q_n\frac{G_n}{N_n^h},\ B_n \approx \frac{1}{2}Q_n\frac{G_n}{N_n^h}. \quad (8)$$

Neglecting the gradient functions in (4) the power pumped in a n-resonance mode by the STNO can be calculated as

$$W_n = \frac{f_n}{2Q_n}\left(A_n^2 N_n^e + B_n^2 N_n^h\right). \quad (9)$$

Microstrip resonator with one embedded STNO. In this section of the paper we analyze the excitation of TEM_1 mode in a microstrip resonator of cross-section $a \times b$ and length $l = \lambda_0/2$; its volume is $V = a \times b \times l$ (fig. 2). The electromagnetic field of TEM-mode in the resonator has the form:

$$E_y = A_n\sin\left(\frac{\pi}{l}z\right),\ H_x = -\frac{A_n}{Z_0}\cos\left(\frac{\pi}{l}z\right). \quad (10)$$

The microwave power W_{MSR} pumped in the resonator from the STNO can be calculated using the maximum value of the electric field:

$$W_{MSR} = \frac{f_n}{Q_n}\frac{\varepsilon_0}{2}\int_0^a dx\int_0^b dy\int_0^l dz\left|E_{y\max}\right|^2 = \frac{f_n}{Q_n}\frac{\varepsilon_0}{4}|A_n|^2 abl, \quad (11)$$

where

$$A_n \approx \frac{1}{2}Q_n\frac{G_n}{N_n^h} = -Q_n\frac{M_0 V_0 Z_0}{abl}\cos\left(\frac{\pi}{l}z_0\right),$$

$$G_n = -\mu_0 \frac{M_0 V_0}{Z_0} \cos\left(\frac{\pi}{l} z_0\right),$$

$$N_n^h = \mu_0 \frac{1}{2Z_0^2} abl .$$

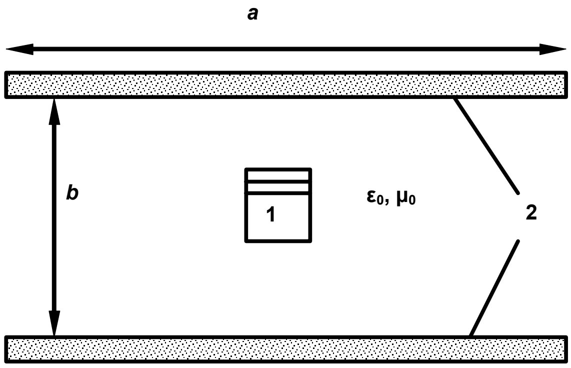

Fig. 2. A front view of a STNO (1) between the plates (2) of microstrip resonator of cross-section *a* × *b*

If, for instance, $z_0 = 0$, then

$$W_{MSR} = \frac{f_0}{Q_n} \frac{\varepsilon_0}{4} |A_n|^2 abl = f_0 \frac{\varepsilon_0}{4} Q_n \frac{M_0^2 V_0^2 Z_0^2}{abl} . \qquad (12)$$

For the values $a = 10\,\mu\text{m}$, $b = 50\,\text{nm}$, $Q_n = 10^3$, and typical STNO parameters, we obtain the maximum output microwave power $W_{MSR}^{\max} \approx 4.2\,\text{pW}$ and for $a = 1\,\mu\text{m}$ – $W_{MSR}^{\max} \approx 42\,\text{pW}$.

Microstrip resonator with many STNOs. The calculations using (12) have demonstrated that absolute value of microwave power emitted by a single STNO are rather small. Thus, to create a practical source of microwave signals based on STNOs it would be useful to use arrays of coupled and synchronized STNOs [27, 42, 49].

There are two approaches to create such an array of STNOs. The first (traditional) approach is to form an array of *N* oscillators connected in parallel or in series and coupled by a common bias current. In such a case, as it was shown in [12], the output power extracted through the MSR mechanism from an array of *N* synchronized STNOs is *N* times larger than the power of a single STNO. The second approach is to place *N* STNOs (coupled through their dipolar electromagnetic fields) inside a resonator with a high Q-factor and extract the power through the above described dipolar emission mechanism. In that case, as it was shown in [29], the output power of the N-oscillator array can be N^2 times larger than the power of a single oscillator, as long the total microwave power extracted from the resonator coupled to the array remains smaller then the power caused by Gilbert damping in a single STNO in the array (in our case this threshold is reached at $N \sim 10^4$).

Using the theory developed in [12] and assuming that a synchronized array of *N* STNOs is placed in a MSR, we can obtain the condition on the number *N*(*f*) of STNOs in the array, that guarantees that the microwave power extracted through the dipolar emission is larger than the power obtained through the magnetoresistance mechanism:

$$N(f_0) \geq N_c(f_0) = \frac{W_{MR}}{W_{MSR}(f_0)} = \frac{f_0^2}{f_c^2} , \qquad (13)$$

where W_{MR} and $W_{MSR}(f)$ are given by (1) and (12), respectively, and f_c is the characteristic frequency of the system (STNO + resonator) at which $W_{MSR}(f_c) = W_{MR}$ for a single STNO.

The typical dependence of $N_c(f_0)$ on f_0 is shown in fig. 3. The straight lines showing the dependence of the critical number of STNOs in an array $N_c(f_0)$ (13) on the generation frequency f_0 for STNOs using the GMR (dashed line) and TMR (solid line) effects are presented in fig. 3. These lines were calculated for the case of STNOs coupled to a MSR assuming that $W_{MR} = 1\,\text{nW}$ for the GMR STNO and $W_{MR} = 1\,\mu\text{W}$ for the TMR STNO. The characteristic frequencies f_c in these two cases are $f_c^{GMR} = 154\,\text{GHz}$ and $f_c^{TMR} = 4.883\,\text{THz}$, respectively. The regions above the GMR (dashed) and TMR (solid) lines are the regions where the direct dipolar emission from a synchronized array of STNOs provides the larger output microwave power than the corresponding (GMR or TMR) magnetoresistance effects.

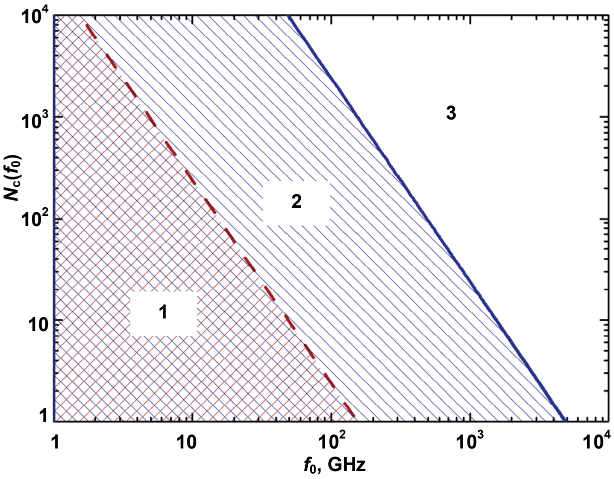

Fig. 3. Dependence of the critical number $N_c(f_0)$ (see Eq. (13)) of STNOs in a synchronized array placed in a microstrip resonator on the generation frequency f_0. If N > $N_c(f_0)$ the microwave power that could be extracted from the array through the dipolar emission mechanism exceed the power that could be extracted through the magnetoresistance mechanism. Solid line is the curve $N_c(f_0)$ for TMR STNO and dashed line is the curve $N_c(f_0)$ for GMR STNO. These lines were calculated for the case of STNOs coupled to a MSR assuming that $W_{MR} = 1\,\text{nW}$ for the GMR STNO and $W_{MR} = 1\,\mu\text{W}$ for the TMR STNO. GMR and TMR mechanisms of microwave power extraction are dominant in the area 1. TMR and dipole emission mechanisms are dominant in the area 2. And the dipole emission mechanism is dominant in the area 3

One can see from fig. 3, if we fix the STNO generation frequency at $f_{0,1} = 50\,\text{GHz}$ and $f_{0,2} = 100\,\text{GHz}$ we can get that the dipolar emission mechanism would be dominant and more convenient for arrays consist of $N_1 \geq 9540$ and $N_2 \geq 2385$ STNOs, respectively.

Lossy model. Here we expand the theoretical model presented above by taking into account the losses in the system. We assume that such important parameter of the MSR as an unloaded Q-factor is a variable parameter, which depends on the number of STNOs *N* embedded into the MSR. This means that the performance of considered type of microwave signal sources depends on the number of STNOs embedded into the MSR and may be substantially lower for a large number of embedded STNOs than in the case of previously developed lossless model. We suppose that the developed formalism can be used for optimization of the practical parameters of microwave signal sources based on STNO arrays.

Theory based on lossy model. The Q-factor of MSR can be defined as

$$Q = 2\pi f \frac{W}{\sum P}, \quad (14)$$

where $f = f_0$ is the resonance frequency of the MSR, W is the energy accumulated in the resonator during the time $1/f_0$, and $\sum P$ is the total power of losses in the system. The term $\sum P$ can be represented as

$$\sum P = P_t + P_b + P_d + P_A(N), \quad (15)$$

where P_t and P_b are the power losses in the top and bottom plates of a MSR, respectively, P_d is the power losses in the dielectric substrate of a MSR, and, finally, P_A is the power losses in an array of N synchronized STNOs. We note, that we deliberately omit the radiation losses in (15), which, however, certainly exists in a real system.

The power losses P_t, P_b and P_d can be calculated as

$$P_t = \int_{S_t} \left[\mathbf{E} \times \mathbf{H}^*\right] d\mathbf{S}_t,$$

$$P_b = \int_{S_b} \left[\mathbf{E} \times \mathbf{H}^*\right] d\mathbf{S}_b, \quad (16)$$

$$P_d = \frac{1}{2}\omega_0 \varepsilon_0 \,\mathrm{tg}\delta \int_{V_d} \mathbf{E}^2 dV_d,$$

where $\mathbf{E}$ and $\mathbf{H}$ are the complex vector amplitudes of electric and magnetic fields, respectively. S_t and S_b are the area of the top and bottom plates of a MSR, respectively, and the vectors $d\mathbf{S}_t$ and $d\mathbf{S}_b$ are directed inside the corresponded plates. V_d is the volume of dielectric substrate of the MSR, $\mathrm{tg}\delta$ is the tangent of dielectric loss of the substrate.

Introducing the accumulated energy W in the form

$$W = \frac{1}{4} \int_{V_{MSR}} \left(\varepsilon_0 \mathbf{E}^2 + \mu_0 \mathbf{H}^2\right) dV, \quad (17)$$

one can calculate the "eigen" unloaded Q-factor of a MSR Q_0 consisting no STNOs:

$$\frac{1}{Q_0} = \frac{P_t + P_b + P_d}{\omega W}. \quad (18)$$

The exact expression for Q_0 can be simplified if we assume, that

$$[\mathbf{n}_t \times \mathbf{E}] = -Z_t[\mathbf{n}_t \times [\mathbf{n}_t \times \mathbf{H}]],$$

$$[\mathbf{n}_b \times \mathbf{E}] = -Z_b[\mathbf{n}_b \times [\mathbf{n}_b \times \mathbf{H}]], \quad (19)$$

where $\mathbf{n}_t$ and $\mathbf{n}_b$ are the unit vector directed inside the top or bottom plates of a MSR, Z_t and Z_b are the surface impedances of the top or bottom plates of a MSR, respectively.

If surface impedances for top and bottom plates of a MSR and the tangent of dielectric loss of the substrate are known then using the simple equations (10) (or more complex expressions for more precise calculations) it is possible to obtain the value of Q_0.

In the following we omit the calculation of Q_0 (it can be done using the appropriate equations (16)–(19) and the equations for electromagnetic field, if required) and assume that $Q_0 = 10^3$ (typical achievable value for high quality MSR). In the following we analyze the dependence of total unloaded Q-factor of the MSR $Q(N)$ on the number of embedded STNOs N:

$$\frac{1}{Q(N)} = \frac{1}{Q_0} + \frac{1}{Q_A(N)}, \quad (20)$$

where

$$Q_A(N) = \omega_0 \frac{W}{P_A(N)}, \; P_A(N) = N \cdot I_{eff}^2 R_{eff}. \quad (21)$$

Here I_{eff} and R_{eff} are the effective current traversing the STNO and the effective resistance of the STNO, respectively.

For simplicity we assume that $R_{eff} \approx R_{dc} = 1\,\Omega$ and analyze the dependence $Q(N)$ for different values of I_{eff}. We use the simplest normalization condition for $Q_A(N)$: $Q_A(N) = 1$ at $N = 10^4$.

The results of numerical calculations of $Q(N)$ is shown in fig. 4.

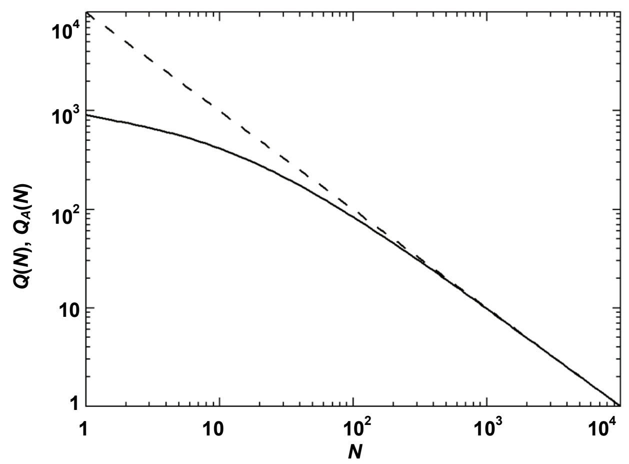

Fig. 4. Dependence of the $Q(N)$ (solid line) and $Q_A(N)$ (dashed line) on the number of STNOs N

Results and discussion. As one can see, the Q-factor of the MSR with N STNOs in decreased while the N is increased. This means that in order to achieve some fixed output microwave power we have to embed more STNOs in a MSR than predicted by Eq. (13). Taking into account Eq. (12), i.e. proportionality between W_{MSR} and Q one can estimate the required number of STNOs $N_{c,L}(f_0)$ accounting the losses as

$$N_{c,L}(f_0) = N_c(f_0) \frac{Q_0}{Q(N)}. \quad (22)$$

Let's consider Eq. (22) in details. If, for instance, $N = 1, 10, 10^2, 10^3$ at frequency $f_{0,1} = 50$ GHz and $f_{0,2} = 100$ GHz, then $N_{c,L}(f_{0,1}) = 10494, 19080, \ldots$, $N_{c,L}(f_{0,2}) = 2624, 4770, 26235, \ldots$. One can see $N_{c,L}(f_0)$ grows dramatically with the increase of N even in our model, which is rough enough. This means that the optimization of microwave signal sources parameters can be a very complicated problem for a microwave source of high output microwave power (because it may consist of many STNOs). From the other hand this problem can be minimized by the application of small arrays of very high frequency STNOs. In this situation the high output microwave power can be achieved by increasing the operation frequency of STNOs but not their quantity in the STNO array.

Nevertheless, although the operation frequencies of STNOs are not very high today, it seems that the problem of microwave signal sources is a complicated problem that must be thoroughly investigated further.

Conclusion. In summary, we have analytically studied on a qualitative level the possibility of application of STNOs and its arrays as the microwave signal sources. We have demonstrated that the microwave power radiated from a single STNO into a microstrip resonator can reach the level of several tens of pW. We show in the scope of lossless model, that although this power level is not very high, the direct measuring of microwave power emitted from a STNO may be convenient for the case of arrays with many (*N*) synchronized oscillators due to the dependence of registered microwave power on *N* as N^2. But in more realistic lossy model we show that the efficiency of such microwave sources is substantially decreased with the increase of number of STNOs embedded in the microstrip resonator. We think that the only solution for this situation is to achieve the high output microwave power from the source by application of STNOs with the most high operation frequencies.

This work was supported in part by grant M/212-2011 of The State Agency of Science, Innovations and Informatizations of Ukraine and by grant UU34/008 of The State Fund for Fundamental Researches of Ukraine.

1. *Гуревич А.Г., Мелков Г.А.* Магнитные колебания и волны. – М., 1994. 2. *Мелков Г.*, *Прокопенко О.* Умови надвисокочастотної синхронізації для магнітних наноконтактів, розташованих у шарі магнітовпорядкованої речовини // Вісник Київського національного університету імені Тараса Шевченка. Серія: радіофізика та електроніка. – 2007. – № 10. 3. *Мойсеєнко В.А., Мелков Г.А., Васючка В.І., Прокопенко О.В., Слободянюк Д.В.* Кореляційна обробка інформації в плівках залізо-ітрієвого гранату // Вісник Київського університету. Серія: фізико-математичні науки. – 2008. – № 4. 4. *Погорілий А.М., Рябченко С.М., Товстолиткін О.І.* Спінтроніка. Основні явища. Тенденції розвитку // Український фізичний журнал. Огляди. – 2010. – Т. 6, № 1. 5. *Прокопенко О.В., Верба Р.В., Борисенко М.О.* Вузькосмуговий режим вимушеної фазової синхронізації магнітних наноконтактів // Вісник Київського національного університету імені Тараса Шевченка. Серія: фізико-математичні науки. – 2008. – № 3. 6. *Acebron J.A., Bonilla L.L., Perez Vicente C.J., Ritort F., Spigler R.* The Kuramoto model: a simple paradigm for synchronization phenomena // Review of Modern Physics. – 2005. – Vol. 77. 7. *Amin N., Xi H., Tang M.X.* Analysis of electromagnetic fields generated by a spin-torque oscillator // IEEE Transaction on Magnetics. – 2009. – Vol. 45. 8. *Berger L.* Emission of spin waves by a magnetic multilayer traversed by a current // Physical Review B. – 1996. – Vol. 54. 9. *Boone C.T., Katine J.A., Childress J.R., Tiberkevich V., Slavin A., Zhu J., Cheng X., Krivorotov I.N.* Resonant nonlinear damping of quantized spin waves in ferromagnetic nanowires: a spin torque ferromagnetic resonance study // Physical Review Letters. – 2009. – Vol. 103. 10. *Cheng X., Boone C.T., Zhu J., Krivorotov I.N.* Nonadiabatic stochastic resonance of a nanomagnet excited by spin torque // Physical Review Letters. – 2010. – Vol. 105. 11. *Chumak A.V., Serga A.A., Hillebrands B., Melkov G.A., Tiberkevich V., Slavin A.N.* Parametrically stimulated recovery of a microwave signal using standing spin-wave modes of a magnetic film // Physical Review B. – 2009. – Vol. 79. 12. *Georges B., Grollier J., Cros V., Fert A.* Impact of the electrical connection of spin transfer nano-oscillators on their synchronization: an analytical study // Applied Physics Letters. – 2008. – Vol. 92. 13. *Heide C.* Spin Currents in Magnetic Films // Physical Review Letters. – 2001. – Vol. 87. 14. *Hoefer M.A., Ablowitz M.J., Ilan B., Pufall M.R., Silva T.J.* Theory of Magnetodynamics Induced by Spin Torque in Perpendicularly Magnetized Thin Films // Physical Review Letters. – 2005. – Vol. 95. 15. *Houssameddine D., Ebels U., Delaët B., Rodmacq B., Firastrau I., Ponthenier F., Brunet M., Thirion C., Michel J.-P., Prejbeanu-Buda L., Cyrille M.-C., Redon O., Dieny B.* Spin-torque oscillator using a perpendicular polarizer and a planar free layer // Nature Materials. – 2007. – Vol. 6. 16. *Kaka S., Pufall M.R., Rippard W.H., Silva T.J., Russek S.E., Katine J.A.* Mutual phase-locking of microwave spin torque nano-oscillators // Nature. – 2005. – Vol. 437. 17. *Katine J.A., Albert F.J., Buhrman R.A., Myers E.B., Ralph D.C.* Current-driven magnetization reversal and spin-wave excitations in Co/Cu // Physical Review Letters. – 2000. – Vol. 84. 18. *Katine J.A., Fullerton E.E.* Device implications of spin-transfer torques // Journal of Magnetism and Magnetic Materials. – 2008. – Vol. 320. 19. *Kiselev S.I., Sankey J.C., Krivorotov I.N., Emley N.C., Schoelkopf R.J., Buhrman R.A., Ralph D.C.* Microwave oscillations of a nanomagnet driven by a spin polarized current // Nature. – 2003. – Vol. 425. 20. *Kiselev S.I., Sankey J.C., Krivorotov I.N., Emley N.C., Rinkoski M., Perez C., Buhrman R.A., Ralph D.C.* Current-induced nanomagnet dynamics for magnetic fields perpendicular to the sample plane // Physical Review Letters. – 2004. – Vol. 425, № 3. 21. *Kiselev S.I., Sankey J.C., Krivorotov I.N., Emley N.C., Garcia A.G.F., Buhrman R.A., Ralph D.C.* Spin-transfer excitations of permalloy nanopillars for large applied currents // Physical Review B. – 2005. – Vol. 72. 22. *Kobeliatskyi V., Melkov G., Moiseienko V., Prokopenko O.* Correlation receiver with wave front reversal of magnetostatic waves // Вісник Київського національного університету імені Тараса Шевченка. Серія: радіофізика та електроніка. – 2010. – № 13. 23. *Krivorotov I.N., Emley N.C., Sankey J.C., Kiselev S.I., Ralph D.C., Buhrman R.A.* Time-domain measurements of nanomagnet dynamics driven by spin-transfer torques // Science. – 2005. – Vol. 307. 24. *Lee K.J., Deac A., Redon O., Nozières J.-P., Dieny B.* Excitations of incoherent spin waves due to spin-transfer torque // Nature Materials. – 2004. – Vol. 3. 25. *Likharev K.K.* Dynamics of Josephson Junctions and Circuits. – N.-Y., 1986. 26. *Mancoff F.B., Rizzo N.D., Engel B.N., Tehrani S.* Area dependence of high-frequency spin-transfer resonance in giant magnetoresistance contacts up to 300 nm diameter // Applied Physics Letters. – 2006. – Vol. 88. 27. *Mancoff F.B., Rizzo N.D., Engel B.N., Tehrani S.* Phase-locking in double-point-contact spin-transfer devices // Nature. – 2005. – Vol. 437. 28. *Myers E.B., Ralph D.C., Katine J.A., Louie R.N., Buhrman R.A.* Current-induced switching of domains in magnetic multilayer devices // Science. – 1999. – Vol. 285. 29. *Pikovsky A., Rosenblum M., Kurths J.* Synchronization: a universal concept in nonlinear sciences. – Cambridge, 2007. 30. *Pozar D.M.* Microwave Engineering. – N.-Y., 1998. 31. *Prinz G.A.* Magnetoelectronics // Science. – 1998. – Vol. 282. 32. Prokopenko O. Microwave sources based on spin-torque nano-oscillators // Вісник Київського національного університету імені Тараса Шевченка. Радіофізика та електроніка. – 2011. – № 15. 33. Prokopenko O., Bankowski E., Meitzler T., Tiberkevich V., Slavin A. Spin-Torque Nano-Oscillator as a Microwave Signal Source // IEEE Magnetics Letters. – 2011. – Vol. 2. 34. *Prokopenko O., Tyberkevych V., Slavin A.* Mutual phase-locking of two spin-torque oscillators: Influence of time delay of a coupling signal // Proceedings of the Europe International Magnetics Conference (Intermag 2008), Madrid, Spain, 2008. 35. *Prokopenko O., Verba R.* Broad-band regime of forced phase-locking of magnetization oscillations in spin-torque nanooscillators // Вісник Київського національного університету імені Тараса Шевченка. Серія: радіофізика та електроніка. – 2009. – № 12. 36. *Ralph D.C., Stiles M.D.* Spin Transfer Torques // Journal of Magnetism and Magnetic Materials. – 2008. – Vol. 320. 37. *Ramo S., Whinnery J.R., Duzer T.V.* Fields and Waves in Communication Electronics. – N.-Y., 1984. 38. *Rezende S.M., de Aguiar F.M., Azevedo A.* Spin-wave theory for the dynamics induced by direct currents in magnetic multilayers // Physical Review Letters. – 2005. – Vol. 94. 39. *Rippard W.H., Pufall M.R., Kaka S., Russek S.E., Silva T.J.*, Direct current induced dynamics in $Co_{90}Fe_{10}$ = $Ni_{80}Fe_{20}$ point contacts // Physical Review Letters. – 2004. – Vol. 92. 40. *Rippard W.H., Pufall M.R., Silva T.J.* Quantitative studies of spin-momentum-transfer-induced excitations in Co/Cu multilayer films using point-contact spectroscopy // Applied Physics Letters. – 2003. – Vol. 82, № 8. 41. *Rippard W.H., Pufall M.R., Kaka S., Silva T.J., Russek S.E.* Current-driven microwave dynamics in magnetic point contacts as a function of applied field angle // Physical Review B. – 2004. – Vol. 70. 42. *Ruotolo A., Cros V., Georges B., Dussaux A., Grollier J., Deranlot C., Guillemet R., Bouzehouane K., Fusil S., Fert A.* Phase-locking of magnetic vortices mediated by antivortices // Nature Nanotechnology. – 2009. – Vol. 4. 43. *Sankey J.C., Braganca P.M., Garcia A.G.F., Krivorotov I.N., Buhrman R.A., Ralph D.C.* Spin-transfer-driven ferromagnetic resonance of individual nanomagnets // Physical Review Letters. – 2006. – Vol. 96. 44. *Schafer S., Chumak A.V., Serga A.A., Melkov G.A., Hillebrands B.* Microwave spectral analysis by means of nonresonant parametric recovery of spin-waves signals in a thin magnetic film // Applied Physics Letters. – 2008. – Vol. 92. 45. *Slavin A.N., Kabos P.* Aproximate theory of microwave generation in a current-driven magnetic nanocontact magnetized in an arbitrary direction // IEEE Transaction on Magnetics. – 2005. – Vol. 41. 46. *Slavin A., Tiberkevich V.* Nonlinear auto-oscillator theory of microwave generation by spin-polarized current // IEEE Transaction on Magnetics. – 2009. – Vol. 47. 45. *Slonczewski J.C.* Current-driven excitation of magnetic multilayers // Journal of Magnetism and Magnetic Materials. – 1996. – Vol. 159. 48. *Slonczewski J.C.* Excitation of spin waves by an electric current // Journal of Magnetism and Magnetic Materials. – 1999. – Vol. 195. 49. *Tiberkevich V., Slavin A., Bankowski E., Gerhart G.* Phase-locking and frustration in an array of nonlinear spin-torque nano-oscillators // Applied Physics Letters. – 2009. – Vol. 95. 50. *Tulapurkar A.A., Suzuki Y., Fukushima A., Kubota H., Maehara H., Tsunekawa K., Djayaprawira D.D., Watanabe N., Yuasa S.* Spin-torque diode effect in magnetic tunnel junctions // Nature. – 2005. – Vol. 438. 51. *Vasyuchka V.I., Melkov G.A., Moiseienko V.A., Prokopenko A.V., Slavin A.N.* Correlation receiver of below-noise pulsed signals based on parametric interactions of spin waves in magnetic films // Journal of Magnetism and Magnetic Materials. – 2009. – Vol. 321, No. 20. 52. *Wang C., Cui Y.-T., Sun J.Z., Katine J.A., Buhrman R.A., Ralph D.C.* Sensitivity of spin-torque diodes for frequency tunable resonant microwave detection // Journal of Applied Physics. – 2009. – Vol. 106. 53. *Yang Z., Zhang S., Li Y.C.* Chaotic dynamics of spin-valve oscillators // Physical Review Letters. – 2007. – Vol. 99.

Submitted on 03.06.2011

UDC 577.3

R. Yatsiuk, post. grad. stud., M. Kononov, Ph. D.

ANALISYS OF MODELS FOR NEURAL NETWORKS MODELING WITH BIG AMOUNT OF NODS

The general structure of biological neuron and mechanisms of its functioning are considered. The main current actual methods of simulation of biological neural networks are described, their analysis is made. The advantages and disadvantages of specific models are pointed out, their limits of application are grounded. Main attention is paid to the modeling of neural networks with big amount of nods.

Keywords: neuron networks, models, ONN.

Розглянуто загальну структуру біологічного нейрона і механізми його функціонування. Наведено основні актуальні на даний момент підходи до моделювання біологічних нейронних мереж, проведено їх аналіз, вказано на переваги і недоліки конкретних моделей, обґрунтовано їх межі застосування. Основну увагу звернено на моделювання нейронних мереж з великою кількістю вузлів.

Ключові слова: нейронні мережі, моделювання, ОНМ.

1. Introduction. The feature of biological approach to the issue of neural networks is that it is based on observations of processes at the cellular level and their descriptions. At some point of time, it accumulates quite a number of experimental data and it becomes difficult to do further research without understanding the nature of the described process. Explanations of these processes a physicist can give by proposing the correct model of the process and describing it mathematically. Besides a physicist can sometimes predict the system behavior under conditions that have not been given experimentally. Due to that the physical models of neural networks and their computer simulation are relevant nowadays.

Attempts to simulate the work of separate parts of the cerebral cortex have been made many times, but, unfortunately, the obtained results are poor. Model behavior of an individual neuron or small group of neurons is a purely theoretical problem and has very little in common with the real biological system. To be closer to biological neural networks we need to increase the number of neurons, but this needs to enlarge computations for modeling. Therefore, this article is devoted to currently available physical models of neurons and analysis of their possible using in networks modeling with big amount of nodes.

2. Biological neuron. Neuron performs reception, elementary conversation and information transfer to other neurons. Information is transferred in the form of pulses of nervous activity with electrochemical nature.

Body cells contain two types of branching sprouts. Sprouts of the first type, called dendrites, serve as input channels for nerve impulses from other neurons. The pulses are delivered into the body of cell, called soma, causing its specific excitation. Then the excitation is spread to output sprout of the second type – axon [2].

The body of a neuron is filled with lead ion solution, surrounded by a membrane with thickness of about 75 angstrom, which has low conductivity. The difference of electric potentials is supported between the inner surface of the axon membrane and the external environment. This is done using molecular mechanism of ion pumps, which creates different concentrations of positive ions K+ and Na+ inside and outside the cell. Permeability of neuron membrane is selective for these ions. Inside the axon, which is at the state of rest, active transport of ions is committed to take the concentration of potassium ions higher than the concentration of sodium ions, while in the fluid, that surrounds the axon, the concentration of Na+ ions is higher. Passive diffusion of potassium ions leads to their intense exit from the cell, causing its negative potential, which is -65 mV [7].

Unlike the situation with a conductor, electrical signal between neurons is transmitted in a wave of depolarization. The pulse of depolarization of the membrane, called spike, is spread along the axon without damping. The speed of spike movement is from 100 to 1000 cm / sec.

The excitation of neuron is transmitted to other neurons of a network. The places of axon membrane, where there is a contact area of the axon of one neuron with dendrites of other neurons, are called synapses. Synapses exchange the information between neurons. Mechanisms of synaptic transmission may have chemical and electrical nature. In a chemical synapse specific chemicals – neurotransmitters that cause changes in permeability of the membrane local area, involve the transmission of impulses. Depending on the type of neurotransmitter synapse can be excitation or inhibition [9].

3. Physical models of neurons. As input signals for neural networks we can use fixed or variable continuous signals, and deterministic or random sequence of pulses. These signals may be supplied to the entire of whole network or on the entrances of some network elements. Network output signals may be pulse sequence, or dynamics of the averaged activity of network elements, or phase relationships between oscillations in different parts of the network. In the first case adequate mathematical apparatus for describing dynamic networks are multidimensional stochastic processes, the second and the third case are deterministic processes in dynamic systems.

Therefore there are several fundamentally different approaches to the creation of physical models of neural networks. According to [3] there are four such approaches:

1. Networks of neurons in which the dynamics of each element are described by a system of differential equations.
2. Networks of integrative-threshold neurons with leak.
3. Networks of neural interacting oscillators.
4. Network of phase oscillators (a separate case, a third approach).

3.1. Networks of neurons in which the dynamics of each element is described by a system of differential equations. The simplest model that corresponds to the first approach is the "integrate-and fire" (I&F) neuron model. Differential equations for this model have the next form:

$$\frac{dv}{dt} = I + a - bv \text{, where } v < v_{пор}\text{, } v \leftarrow c \text{, where } v \geq v_{пор}\text{,}$$

where v – neuron membrane potential, I – input current, $a, b, c, v_{пор}$ – parameters. When the value of the membrane potential v reaches a threshold value $v_{пор}$, the neuron generates a wave in the shape of burst. Waves in this model do not have delays, what is explained with the presence of a fixed threshold. Although the I&F model is simple and easy to understand, it is considered as one of the worst models to simulate the vibrations and can be used excluding the proof of analytical results.

Considering melt-cortical neurons it is proposed a model of "integrate-and-fire-or-burst" [19], which can generate vibrations in the form of explosions:

$$\frac{dv}{dt} = I + a - bv + \mathrm{gH}(\mathrm{v}-\mathrm{v_h})\mathrm{h}(\mathrm{v_T} - v),$$

$$\frac{dh}{dt} = -h/\tau_h^-, \text{ if } V > V_h,$$

$$\frac{dh}{dt} = (1-h)/\tau_h^+, \text{ if } V < V_h,$$

where h – deactivation of T-current, $g, v_h, v_T, \tau_h^-, \tau_h^+$ – parameters, which describe T-current. H – heaviside step function.

A somewhat more complex model, which enables to obtain almost all forms of neural oscillations is Izhikevich's model [17]:

$$\frac{dv}{dt} = 0.04v^2 + 5v + 140 - u + I,$$

$$\frac{du}{dt} = a(bv - u),$$

$$v \leftarrow c, u \leftarrow u + d, \text{ if } v>=30\text{mV},$$

where v,u are dimensionless membrane potentials and dimensionless membrane recovery, a,b,c,d – dimensionless parameters. Variable u simulates activation of ionic currents K+ and deactivation of ionic currents Na+ and provides negative feedback to v. I simulates external currents. This model was used to simulate the functioning of neural network, which contained 10^5 neurons of the cerebral cortex and generated oscillations in the form of spikes and explosion with delays and synchronization of oscillations.

To describe the dynamics of vibrations in the form of spikes for many neurons it is appropriate to use a resonator model of Fitz Hugh-Nagumo:

$$\frac{dv}{dt} = a + bv + cv^2 + dv^3 - u,$$

$$\frac{du}{dt} = \varepsilon(ev - u),$$

where v,u are the same as in previous model, a,b,c,d,ε,e – parameters, choice of them make a form for vibrations.

In [18] a model of Morris-Lekar is proposed. The model was used to describe the vibrations in muscle fibers of large bivalves. This model has a biophysical meaning and contains parameters that can be measured. The model consists of three differential equations, the first containing the membrane potential with instant activation, second and third are optional and describe the slow activation.

$$I = C\frac{dv}{dt} + g_L(V_L) + g_{Ca}M(V - V_{Ca}) + g_K N(V - V_K)$$

$$\frac{dM}{dt} = \lambda_M(V)[M_\infty(V) - M],$$

$$\frac{dN}{dt} = \lambda_N(V)[N_\infty(V) - N],$$

where $M, N, \lambda_M, \lambda_N$ are described below:

$$M_\infty(V) = \tfrac{1}{2}\{1 + \tanh[(V - V_1)/V_2]\},$$

$$\lambda_M(V) = \bar{\lambda}_M \cosh([V - V_1]/2V_2),$$

$$N_\infty(V) = \tfrac{1}{2}\{1 + \tanh[(V - V_3)/V_4]\},$$

$$\lambda_N(V) = \bar{\lambda}_N \cosh([V - V_3]/2V_4),$$

$C, g_L, g_{Ca}, g_K, V_L, V_{Ca}, V_K, V_1, V_2, V_3, V_4, \bar{\lambda}_M, \bar{\lambda}_N$ – parameters of described system.

The most popular model, which refers to the first approach is the Hodgkin-Huxley model [2, 6, 16]. The basis of this model is the first law of Kirchhoff. The model quite accurately describes the dynamics of membrane potential, it can simulate the behavior of the neuron under the influence of external current, which flows through the membrane, it describes well the activation and deactivation of Na currents, activation of Ca currents, the process of generating pulses, subthreshold stimulation, refractory, fiber hyperpolarization, accommodation etc. The model is also important because its parameters have biological meaning and can be measured. The framework consists of four differential equations and large number of auxiliary parameters. A complete system of equations is as follows:

$$C\frac{dV}{dt} = g_K(V - V_K) + g_{Na}(V - V_{Na}) + I(t), \text{ where}$$

$$g_K = g_{K\max}n^4, \; g_{Na} = g_{Na\max}m^3h,$$

$$\frac{dn}{dt} = \alpha_n(1-n) - \beta_n n,$$

$$\frac{dm}{dt} = \alpha_m(1-m) - \beta_m m,$$

$$\frac{dh}{dt} = \alpha_h(1-h) - \beta_h h,$$

$$\alpha_n = \frac{0.01(V-10)}{1 - e^{(25-V)/10}}, \; \beta_n = 0.125e^{-V/80},$$

$$\alpha_m = \frac{0.1(V-25)}{1 - e^{(25-V)/10}}, \; \beta_m = 4e^{-V/18},$$

$$\alpha_h = 4e^{-V/20}, \; \beta_h = \frac{1}{1 + e^{(30-V)/10}},$$

V – membrane potential, V_K, V_{Na} – sodium and potassium equilibrium potentials, respectively. However, this model has one disadvantage – it requires a lot of computations and using this model to simulate neural network with big amount of nods today is impossible. Hence there are neuron models, which are called the simplified Hodgkin-Huxley models. These models include the models of Fitz Hugh-Nagumo and Morris-Lekar, which were discussed above. Nevertheless, even such models still cannot approximate the neural network, which has the same number of elements as the human brain (10^9-10^{10} neurons).

Another very interesting model, which is based on simplification of Hodgkin-Huxley equations, is described in [5]. In this model, the nerve fiber is equivalent to the coaxial line and the system of equations is based on the telegraph equations:

$$C_0\frac{dV}{dt} = -\frac{dI}{dx} - g_0(V - E),$$

$$-\frac{dV}{dx} = r_0 I,$$

where V – membrane potential, I – current along the bone neuron, C_0, g_0, r_0 – linear parameters of capacitance, conductance and resistance, E – external electromotive force. The method of lines (method of finite differences using one of the arguments) was applied to solve this system. It is based on the obtained results and we can say that this model describes quite well the voltage dependence of time with different parameters of neural system (distance from the excitement, axon diameter).

3.2. Networks of integrative-threshold neurons with leak. *Integrative-threshold* neuron model is a relatively simple device that collects input signals and generates a pulse (action potential) at the threshold. In this model such things as absolute and relative refractory, synaptic delay in signal transmission, the dynamics of postsynaptic potentials and some others [13] can be taken into account. This type of neural network is by far the most common object of both theoretical studies and in the simulation. The simplest classical model of this type is threshold integrator with leak. The mathematical model is written in the form of one-dimensional stochastic Langevin equation and is as follows:

$$\frac{dv}{dt} = -\mu v + I(t) + \sqrt{D}\xi(t) \ ,$$

where V – models the membrane potential of neuron, $\mu(t)$ – a constant of relaxation, $I(t)$ – external action (current), $\xi(t)$ - white Gaussian noise with unit intensity and zero mean value, D – intensity of current noise on the neuron. $\xi(t)$ in this case simulates the effects of various sources of noise in neural environment: thermal noise, unreliability of synaptic contacts between neurons and nerve fibers, and a large number of input neurons (about 10^4) from its nearest neighbors [15]. It should be noted that despite the linearity of the equation, the model is nonlinear because of the presence of a threshold generation of pulses.

3.3. Networks of neural interacting oscillators. Considering the oscillator neural networks (ONM), the main interest focuses on the dynamic and vibrational aspects of the networks. The interest is provided to the conditions of oscillations and their synchronization. One of the central hypothesis is that the process of information processing in the nervous system can be described in terms of synchronization of activities of different neural structures. This hypothesis was formulated in the works of famous Russian neurophysiologists A.A. Ukhtomskiy [12] and M.N. Lyvanov [8]. The great interest is linked with experimental data on tetarythm research – low-frequency oscillatory activity (see, for example, the work of O. Vinogradova [4]). Nowadays the work is made in two interrelated areas:

- mathematical study of synchronization in ONM;
- appling ONM models for modeling olfactory and visual cortex and motor systems as well as memory and attention.

Depending on the architecture of connections between oscillators two types of ONM are considered:

- fully connected network of oscillators;
- network with local ties.

If the oscillators are connected in ONM with weak ties of order ε, the system can be described by the following differential equations:

$$\frac{\partial x_k}{\partial t} = F_k(x_k) + \varepsilon G_k(x_1,...,x_N), x_k \in R^m, k = 1,...,N \ ,$$

in the case of additive relationships between the oscillators the equation takes the following form:

$$\frac{\partial x_k}{\partial t} = F_k(x_k) + \varepsilon \sum_j G_{kj}(x_k, x_j), x_k \in R^m, k = 1,...,N \ .$$

For the phase oscillators it is used the system of the following type:

$$\frac{\partial x_k}{\partial t} = \omega_k \varepsilon \sum_j H_{kj}(\theta_k, \theta_j), k = 1,...,N \ ,$$

where 2π – periodic functions H_{kj} are obtained using the averaging and dependence on the type of oscillator, as well as from the architecture and the type of relations (functions $G_{kj}(x)$).

It is usually focuses on synchronization of vibrations. It is considered that the network is in the regime of synchronization if each oscillator stabilizes its frequency at $t \to \infty$:

$$\frac{\partial \theta_k}{\partial t} \xrightarrow[t\to\infty]{} \Omega_k \ .$$

As it was mentioned that ONM can be used for building models of olfactory and visual cortex, motor system, but the greatest interest for the present application of ONM is memory modeling. Information stored in the network as a phase. This approach to memory modeling was used in [10]. In this case there were used phase oscillators of the following type:

$$\frac{\partial \phi_i}{\partial t} = \omega_i + \sum_{i=1}^{N} K_{ij} f(\phi_j - \phi_i), i = 1,...,N \ ,$$

where f – periodic odd function. It is shown that under certain conditions, remembering of information in this ONM is better than in the Hopfild's network. The same approach of memory modeling is described in [14], but in this case the oscillator of Van der Pol was used as a network element. In [1] it is considered the synchronization of neural ensembles and the question of associative memory. There were used the oscillators of Wilson-Kovan's:

$$\frac{dx_i}{dt} = -\frac{-x_i}{\tau_x} + F_x\left[T_{xx}\frac{x_i}{\bar{x}} - T_{xy}G\left(\frac{y_i}{\bar{y}}\right) + S_i + I_i - H_i\right]$$

$$\frac{dy_i}{dt} = -\frac{-y_i}{\tau_y} + F_y\left[-T_{yy}\frac{y_i}{\bar{y}} - T_{yx}\frac{x_i}{\bar{x}}\right],$$

$$H_i = \alpha\int_0^t x_i(\tau)\exp\left[-\beta(t-\tau)\right]d\tau, i = 1,...,N \ ,$$

4. Validation of models for neural networks with big amount of nodes. Based on this review, we consider that it is necessary to analyze described models for their suitability for neural networks modeling with big amount of nodes and choose the optimal model for this task.

The estimates for computations for most of the models, which are described, are given in [11]. This work presents estimates of the number of operations needed to simulate vibrations of one neuron within 1 ms when using first order Euler's method with fixed step. Models I&F require from 4 to 13 floating point operations to simulate the vibrations within 1ms. Izhikevich's model requires 13 operations using the same parameters. The model of Fitz Hugh-Nagumo requires 72 operations for neuron modeling for 1 ms with the time of discretization equal to 0.25 ms (at a larger time the discretization model looses its essential features). The model of Morris-Lekkar requires 600 floating point operations when selecting the time of discretization equal to 0.1 ms, and the Hodgkin-Huxley model with the same parameters requires 1200 operations. For the ONM models there are no such data, because in this case everything depends on the chosen model and on description of neural network.

So, counting, for example, how many operations Hodgkin-Huxley model needs to model the behavior of a neuron during 1sec, multiplying it by the number of neurons in our network (take 10^9, as in the brain), taking into account the number of connections between neurons, we can see that no supercomputer can simulate the behavior of such a network of neurons in real time. So we come to the conclusion that we should choose the simplified model (depending on the task) and limit neural network with fewer nodes (about 10^5–10^6). The most successful of the above models in this case is Izhikevich's model, which requires relatively few computing resources and can simulate almost all kinds of vibrations. We can also use the model of Morris-Lekkar, lowering the number of neurons in network.

5. Conclusions. Thus, summing up the above mentioned, we can come to the conclusion that there are different approaches to neural networks modeling. If the task is to study the dynamics of states of a neuron form the measured parameters (such as conductivity, activation functions and time constants), the best choice would be the Hodgkin-Huxley model. However, this model requires a lot of computations and therefore cannot simulate a network with many neurons. In this case the simplified Hodgkin-Huxley models are very useful, such as, for example, the model of Fitz Hugh-Nagumo. If we need to simulate the neural network with big amount of nods, the best choice is I&F model or one of its modifications, but unfortunately, these models only approximately describe the behavior of biological neurons and do not include many of their features. To simulate passing signals through nonlinear noisy environment it is appropriate to choose the model of integrative-threshold neurons with leak. When modeling processes associated with the functionality of the brain (visual, olfactory, auditory cortex, processes, memory and attention) typically are used ONM models, where we can use the equations, which describe the averaged dynamics of the ensemble. This saves computational resources, but introduces some uncertainty due to averaging.

1. *Абарбанель Г.Д.И., Рабинович М.И., Селверстоун А.* и др. Синхронизация в нейронных ансамблях // Успехи физических наук. – 1996. – Т. 166, № 4. – С.363–390. 2. *Беркинблит М.Б., Глаголева Е.Г.* Электричество в живых организмах. – М., 1988. 3. *Борисюк Г.Н., Борисюк Р.М., Казанович Я.Б., Иваницкий Г.Р.* Модели динамики нейронной активности при обработке информации мозгом – итоги "десятилетия" // Успехи физических наук. – 2002. – Т. 172, № 10. – С. 1189–1214. 4. *Виноградова О.С.* Гиппокамп и память. – М., 1975. 5. *Горячко В.* Математична модель поширення нервового імпульсу в нейроні // Теоретична електротехніка. – 2005. – № 58. – С. 20–26. 6. *Заенцев И. В.* Нейронные сети: основные модели : Учебное пособие к курсу "Нейронные сети". – Воронеж, 1999. 7. *Костюк П.Г., Зима В.Л., Магура І.С. та ін.* Біофізика. – К., 2001. 8. *Ливанов М.Н.* Нейронные механизмы памяти // Успехи физиологических наук. – 1975. – Т. 6. – С. 66–89. 9. *Маркий В. С., Пастушенко В. Ф., Чизмаджев Ю. А.*. Физика нервного импульса // Успехи физических наук. – 1977. – Т. 123, № 2. – С. 289–332. 10. *Плахов А.Ю., Фисун О.И.* Осцилляторная модель нейронных сетей // Математическое моделирование. – 1991. – Т. 3, № 3. – С. 48–54. 11. *Тимощук П.В.* Порівняльний аналіз моделей нейронних осциляторів // Автоматика, вимірювання та керування. – 2009. – № 639. – С. 243. 12. *Ухтомский А.А.* Избранные труды. – Л., 1978. 13. *Ушаков Ю.В.* Модель нейрона "Пороговый интегратор с утечкой" в исследованиях прохождения сигналов через нелинейные зашумленные среды // Актуальные проблемы статистической радиофизики. – 2009. – Т. 8. – С. 68–87. 14. *Abbott L.F.* Modulation of function and gated learning in a network memory // Proc. Natl. Acad. Sci. USA. – 1990. – Vol. 87. – P. 9241–9245. 15. *Gerstner W., Kistler W.M.* Spiking Neuron Models. Single Neurons, Populations, Plasticity. – Cambridge University Press, 2002. 16. *Hodgkin A. L., Huxley A. F.* A quantitative description of membrane current and application to conduction and excitation in nerve // Physiology. – 1954. – № 117. – P. 500–544. 17. *Izhikevich E. M.* Simple model of spiking neurons // IEEE Transactions on Neural Networks. – 2003. – Vol. 14, № 6. – P. 1569–1572. 18. *Morris C., Lecar H.* Voltage oscillations in the barnacle giant muscle fiber // Biophysics. – 1981. – № 35. – P. 193–213. 19. *Smith G. D., Cox C. L., Sherman S. M., Rinzel J.* Fourier analysis of sinusoidally driven thalamocortical relay neurons and a minimal integrate-and-fire-or-burst model // Neurophysiology. – 2000. – № 83. – P. 588–610.

Submitted on 06.06.2011

Наукове видання

ВІСНИК

КИЇВСЬКОГО НАЦІОНАЛЬНОГО УНІВЕРСИТЕТУ ІМЕНІ ТАРАСА ШЕВЧЕНКА

РАДІОФІЗИКА ТА ЕЛЕКТРОНІКА

Випуск 16

За авторською редакцією

Оригінал-макет виготовлено Видавничо-поліграфічним центром "Київський університет"
Виконавець *Д. Ананьївський*

Підписано до друку 20.10.11. Формат 60x84$^{1/8}$. Вид. № Рф2. Гарнітура Arial. Папір офсетний.
Друк офсетний. Наклад 300. Ум. друк. арк. 6,85. Обл.-вид. арк. 9,83. Зам. № 211-5816.

Видавничо-поліграфічний центр "Київський університет"
01601, Київ, б-р Т. Шевченка, 14, кімн. 43,
☎ (38044) 239 32 22; факс (38044) 239 31 28.
E-mail: vydav_polygraph@univ.kiev.ua
WWW: http://vpc.univ.kiev.ua